STATE OF CALIFORNIA • DEPARTMENT OF TRANSPORTATION

TECHNICAL REPORT DOCUMENTATION PAGE

DRISI-2011 (REV 10/1998)

1. REPORT NUMBER	2. GOVERNMENT ASSOCIATION NUMBER	3. RECIPIENT'S CATALOG NUMBER
CA18-3018		

4. TITLE AND SUBTITLE	5. REPORT DATE
Development of Accurate Damping Models for Nonlinear Time History Analysis	August 14, 2019
	6. PERFORMING ORGANIZATION CODE UCLA
7. AUTHOR Ertugrul Taciroglu, and S. Farid Ghahari	8. PERFORMING ORGANIZATION REPORT NO. UCLA SGEL 2019-07
9. PERFORMING ORGANIZATION NAME AND ADDRESS Department of Civil and Environmental Engineering University of California, Los Angeles UCLA, 5731E Boelter Hall Los Angeles, CA 90095-1593	10. WORK UNIT NUMBER
	11. CONTRACT OR GRANT NUMBER 65A0642
12. SPONSORING AGENCY AND ADDRESS California Department of Transportation	13. TYPE OF REPORT AND PERIOD COVERED Final Report 07/27/2017-05/31/2019
	14. SPONSORING AGENCY CODE

15. SUPPLEMENTARY NOTES

Prepared in cooperation with the State of California Department of Transportation.

16. ABSTRACT

California's bridges provide vital transportation links, and their seismic performance impacts the entire state and thus, the nation. In order to accurately estimate the response of bridges under earthquake ground motions, highly detailed and accurate Finite Element (FE) models are necessary. While the nonlinear behaviors of most elements can be captured relatively well with current capabilities, devising accurate models and parameter values for damping has eluded researchers and practitioners alike. In order to identify the inherent damping from real-life data and distinguish its effects from other sources of energy dissipation, a novel Bayesian Finite Element (FE) model updating framework was developed and extensively verified and validated through synthetic and real-life data. This new method can be applied to real-life earthquake data recorded by bridges which are instrumented by Caltrans through the California Strong Motion Instrumentation Program (CSMIP). Two typical concrete bridges in California were selected and the proposed solution was applied to several earthquake data sets. It was determined that the identified inherent damping confirms that the current 5% Rayleigh damping model is only reliable if the bridge is under a moderate earthquake. If the level of excitation is weak, 2% damping is advised. As no strong earthquake data has been recorded by these two bridges, it was not possible to present any validated conclusion for this level of earthquake intensity. The methodology developed herein has no limitations in this regard and can be applied to other bridges and intensity levels in the future.

17. KEYWORDS	18. DISTRIBUTION STATEMENT	
Energy dissipation, inherent damping, structural nonlinearity, CSMIP Bridges, Bayesian output-only estimation		
19. SECURITY CLASSIFICATION (*of this report*) Unclassified	20. NUMBER OF PAGES 126	21. COST OF REPORT CHARGED

Structural & Geotechnical Engineering Laboratory

UCLA

Development of Accurate Damping Models for Nonlinear Time History Analysis

Ertugrul Taciroglu
S. Farid Ghahari

University of California, Los Angeles
Department of Civil & Environmental Engineering

Development of Accurate Damping Models for Nonlinear Time History Analysis

PRINCIPAL INVESTIGATOR

Ertugrul Taciroglu

University of California, Los Angeles

ASSISTANT PROJECT SCIENTIST

S. Farid Ghahari

University of California, Los Angeles

UCLA SGEL Report 2019-07

also a Final Report submitted to the
California Department of Transportation under Award No. ***65A0642***

Department of Civil and Environmental Engineering

University of California, Los Angeles

June 2019

FUNDING AGENCY ACKNOWLEDGMENT

Support for this research was provided by the California Department of Transportation under Research Contract No. 65A0642, which is gratefully acknowledged. Authors would also like to thank Pat Hipley, Toorak Zokaie, and Mark Mahan who provided oversight and recommendations during the course of this project.

DISCLAIMER STATEMENT

The content of this report was developed under Contract No. 65A0642 from the California Department of Transpiration. This report has not been edited to the standards of a formal publication. Any opinions, findings, conclusions or recommendations contained in this report are those of the authors, and should not be interpreted as representing the official policies, either expressed or implied, of the State of California.

EXECUTIVE SUMMARY

California's bridges provide vital transportation links between metropolitan, industrial and agricultural regions, and their seismic performance impacts the well-being of the entire state and thus the nation. In order to accurately estimate the response of bridges under earthquake ground motions, highly detailed and accurate Finite Element (FE) models are necessary. While the nonlinear behaviors of most superstructure components and foundation elements can be captured relatively well with current capabilities, devising accurate models and parameter values for damping has eluded researchers and practitioners alike. It is fair to state that models and values of damping used today are largely based on numerical/analytical conveniences, qualitative observations, and engineering intuition. Unfortunately, as it is not possible to theoretically derive a model of damping, and thus, damping models for bridges (and other civil structures) bear by significant levels of ambiguity. Proper estimation of inherent diffuse damping in structures is becoming a simultaneously more tractable and critical objective, because many other sources of energy dissipation in the bridge system now have explicit and validated models. In efforts directed towards this objective, there is always a risk of double-counting the damping forces, because inherent damping can only be estimated from real-life data, and the available empirical damping values have been obtained from data that came from bridges/buildings that may have exhibited damage or other types of dissipation due to concrete cracking, soil-structure interaction, etc.

Model-based system identification methods appear indispensable in efforts to identify the inherent damping in structures from real-life data and to distinguish it from damping due to other sources of energy dissipation. One such approach is the so-called Finite Element (FE) model updating method wherein the parameters of a numerical model of the structure is modified to match the model predictions with real-life data. While FE model updating procedures using ambient and/or operational vibration data are quite straightforward, they are not necessarily beneficial because the levels of vibration in those recoded signals are much lower than those expected in moderate earthquakes. To resolve this issue, earthquake data recorded by instrumented bridges must be used. In the U.S., the California Department of Conservation initiated the California Strong Motion Instrumentation Program (CSMIP) in 1972 through which multiple bridges were instrumented with funding and oversight provided by the California Department of Transportation (Caltrans).

In the present project, a joint system-input identification/model updating method is developed through which uncertain properties of a bridge model, including its various sources of damping, together with unmeasured Foundation Input Motions (FIMs) can be identified using sparsely measured acceleration responses recorded during an earthquake. In addition to the identification of inherent damping in the presence of other explicit sources of energy dissipation, the developed framework is capable of (1) producing a calibrated FE model of a bridge structure, which can be used as a Digital Twin for future response predictions, damage assessment, and Structural Health Monitoring (SHM); (2) estimating FIMs, which, in turn, can be used to quantify Soil-Structure Interaction (SSI) effects, as well as spatial variations of the ground motions from real-life data. The latter output of the developed method provides a valuable and unique opportunity to investigate kinematic SSI effects using real-life data, as most efforts on this subject have been limited to analytical and numerical studies.

After extensive verification and validation studies, the solution developed in the present project has been applied to two typical concrete bridges in California. The identified inherent damping confirms that the current 5% Rayleigh damping model is only reliable if the bridge is subjected to a moderate earthquake. If the level of excitation is weaker, then 2% damping is advised. On the other hand, a validated recommendation cannot be made for the case strong (damaging) earthquakes due to lack of recorded data. While it appears safe to assume that damping due to hysteresis and damage to structural components that are implicitly included in nonlinear time history analyses will be overwhelmingly larger than the typical viscous modal damping values assumed for weaker events, it is recommended, as a follow up effort, to carry out parametric analytical studies on typical bridge models to examine the consequences of including or excluding viscous damping on damage/performance estimates under strong earthquakes.

TABLE OF CONTENTS

LIST OF FIGURES

LIST OF TABLES

CHAPTER 1: INTRODUCTION

1.1. INTRODUCTION

California's bridges provide vital transportation links between metropolitan, industrial and agricultural regions, and their seismic performance impacts the well-being of the entire state and thus the nation. In order to accurately estimate the response of bridge structures under earthquake ground motions, highly detailed and accurate Finite Element (FE) models are necessary. Although the state-of-knowledge is in its maturity stage [1]–[3], and there are many powerful commercial software tools available for this purpose, there have always been numerous sources of uncertainties in the created models. Damping properties of a structure have typically been one of the most significant sources of these uncertainties. While the nonlinear behaviors of most superstructure components and foundation elements can be captured relatively well with current capabilities, devising accurate models and parameter values for damping has eluded researchers and practitioners alike. It is fair to state that models and values of damping used today are largely based on numerical/analytical conveniences, qualitative observations, and engineering intuition. For example, most engineers use Rayleigh damping, which is mainly due to the convenience it offers in linear (or equivalent linear) modal response analyses (the said advantage actually vanishes for nonlinear time-history analyses). According to the latest version of the Caltrans Seismic Design Criteria (Caltrans, 2013), "*A 5% damped elastic response spectrum shall be used for determining seismic demand in Ordinary Standard concrete bridges*." Or it is stated that "*for bridges that are heavily influenced by energy dissipations at abutments, 10% damping can be justified*." Therefore, because it is not possible to theoretically derive a model of damping, damping models for bridges (and other civil structures) are accompanied by significant levels of ambiguity[1]. The proper estimation of the inherent damping is getting more attention, as other sources of energy dissipation in the bridge system (see Figure 1-1) are explicitly modeled. So, there is always a risk of double counting the damping, because inherent damping can only be estimated from real-life data (Jeary, 1997), and the available empirical damping values have been obtained from data which come from bridges/buildings with implicitly having such energy dissipation mechanism.

While data-driven identification methods, e.g., [4], have been traditionally used for damping identification from real-life data, they are not useable when various sources of damping are needed to be estimated separately. In other words, model-based identification methods are inevitable to be able to carry out this task. Such an approach is called Finite Element (FE) model updating [5] in which a numerical model of the bridge structure is modified to match real-life data. While FE model updating using ambient and/or operational data is quite straightforward [6], [7], they may not be beneficial because the level of

[1] It is expedient to note there that recent trial studies at Caltrans showed that applying Rayleigh damping to abutment backfill spring models for a typical two-span bridge affected maximum bent displacements by more than 50% (Caltrans , 2016).

vibration is much lower than those expected in moderate earthquakes. To resolve this issue, data recorded during earthquakes through proper instrumentation should be used. In the United States, California Department of Conservation (DOC) initiated a program called California Strong Motion Instrumentation Program (CSMIP) [8] in 1972 through which many bridges were instrumented with the funding and the instrumentation layout recommendation provided by the California Department of Transportation (Caltrans). The data collected by these instrumented bridges during the last three decades helped researchers all around the world to increase their understanding of bridge behavior during earthquakes [9]–[11].

Figure 1-1: Major explicit sources of energy dissipation in bridge structures.

However, contrary to the ambient data, the data collected during earthquakes cannot be easily used with classic FE model updating methods due to two main reasons. First, the bridge structures are usually large scale structures which are under multiple support excitations [12]. To be able to carry out model updating, all input excitations to the system must be recorded, which would need quite a number of sensors, while almost all of the existing instrumented bridges (see https://strongmotioncenter.org/) suffer from lack of instrumentation. Second, even having a densely instrumented bridge with many sensors to measure the motion of all foundations, the recorded foundation motions are not the actual input motions due to Soil-Structure Interaction (SSI) effects [13]. Due to the impedance contrast between the soil and the foundation, the foundation experiences different motions, called Foundation Input Motions (FIMs), than the Free-Field Motion (FFM). Moreover, the signal recorded at the foundation is affected by the feedback from the dynamic response of the bridge due to the flexibility provided by the soil which is called Impedance Function (IF). On account of these facts, output-only identification methods need to be designed to carry

out FE model updating. Moreover, the output-only FE model updating must be carried out in the time domain and can deal with nonlinearity (material and geometry) to be used for the real-life data. The recently developed Blind Modal Identification (BMID) [14]–[17] methods are not capable for this purpose, as they are limited to linear-elastic behavior.

In this project, we develop a joint system-input identification/model updating method through which uncertain properties of the bridge model, including various sources of damping, along with unmeasured FIMs can be identified using sparsely measured acceleration responses recorded during an earthquake. In addition to the identification of the inherent damping in the presence of other explicit sources of energy dissipation, the developed framework and its current and future results can results in: 1- the FE model of a bridge structure which is updated to match to the recorded responses, and can be used for future response prediction, damage assessment, and Structural Health Monitoring (SHM) purposes; 2- the identified FIMs can be used to study kinematic SSI as well as spatial variation of the ground motions from real-life data. The latter would provide us with an opportunity to investigate realistic kinematic SSI effects, because, most of the studies on the kinematic SSI effects are limited to analytical and numerical (e.g., [18], [19]).

The method presented herein employs a sequential Bayesian model updating method originally developed for building structures [20]. The overall representation of this method is shown in Figure 1-2 and will be described in details later. In this method, we assume a prior normal distribution for the unknown parameter vector $\boldsymbol{\psi}$ (collection of system's uncertain parameters and inputs) and propagate this uncertainty through the FE model. Based on the Bayes' rule, the posterior distribution is obtained by calculating the difference between the prediction and measurement (collected through sensors). This process is sequentially continuing in time. To show the applicability of the method to even complexes and large scale structures, we verify it through simulated data obtained from the Golden Gate Bridge (GGB) under the 2014 South Napa earthquake. The method is computationally expensive, so a double parallel processing framework is designed and described here. The method then will be used on a classic soil-bridge interaction problem, i.e., Meloland Road Overpass. Finally, the method is applied on several real-life earthquake data sets recorded at the San Roque Canyon and UnionMills bridges to estimate inherent damping values along with unmeasured FIMs and some other uncertain parameters.

In the remainder of Chapter 1, we first show the importance of the inherent damping in the presence of other sources of energy dissipation through a series of direct simulations. Then, the available data which can be used within the proposed framework is reviewed. In Chapter 2, we introduce a software which is specifically designed to classify available data in the CESMD. Chapter 3 presents the initial development of the Bayesian output-only identification method which will be completed in Chapter 4. An extensive verification of the proposed solution along with challenges for real-life applications is carried out in Chapter 5 by using the numerical model of the Golden Gate Bridge. Also, real-life data of this bridge is used to test the performance of the method when there is significant modeling uncertainty in the developed FE model. Chapter 6 is devoted to the Meloand Road Overpass (MRO), which is a well-studied bridge especially due to its significant interaction with the surrounding soil (an important explicit source of damping). We extensively studied available earthquake data and extracted inherent damping from these real-life data sets. In a practical point of view, Chapter 7 is the most important part of this project in which two bridges which

can be representative of a large number of bridges in California are studied. Before studying real-life data, a series of identifiability and verification are carried out to make sure that the results of the real data are reliable. The major findings of this project are summarized in the final chapter along with recommendations for future studies. Throughout this report, we call the collection of the deck, piers, abutments, foundation, and soil at pier foundations and abutments as bridge systems. This bridge system is composed of various substructures including, for example, soil-foundation substructures. When the isolated bridge body without soil is meant, the term superstructure is used.

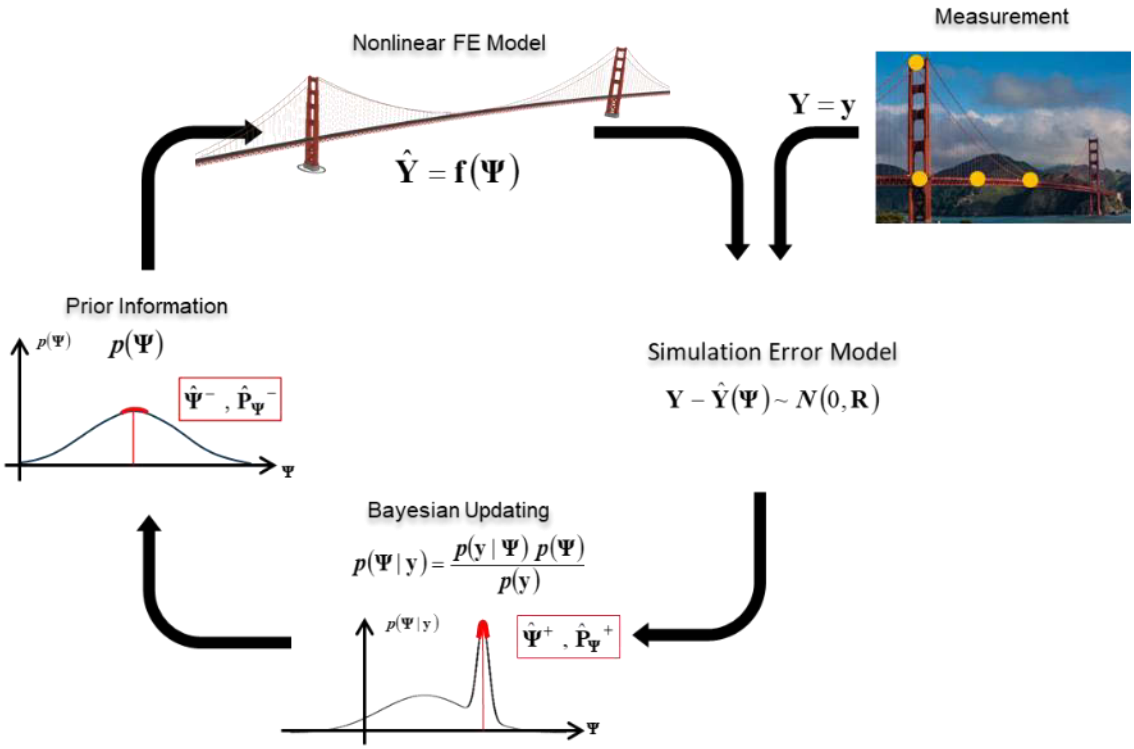

Figure 1-2: Overall representation of the proposed identification method.

1.2. IMPORTANCE OF THE INHERENT DIFFUSE DAMPING

The subject of the present study is to quantify the level of the inherent damping should be used within a detailed nonlinear Finite Element model where other sources of energy dissipation are explicitly modeled. Herein, we try to see how important this specific damping is in comparison with other damping sources through a series of nonlinear analyses. The energy equilibrium in a structural system can be written as [21]

$$E_K + E_S + E_D = E_I \tag{1-1}$$

where E_K, E_S, E_D, are a kinetic, strain, and damping energy, respectively. E_I is the input energy to the system which is calculated as

$$E_I = -\int_0^T \left(\mathbf{ML}\ddot{\boldsymbol{u}}_g\right)^T d\boldsymbol{u} \tag{1-2}$$

in which **M** and **L** are mass and influence matrices, $\ddot{\boldsymbol{u}}_g$ is a vector of ground motions, and $\boldsymbol{u}$ is the relative displacement of the structure. T as an integral upper bound shows the duration of response, while as a superscript denotes matrix/vector transpose. Kinetic energy can be calculated in a similar way as

$$E_K = \int_0^T (\mathbf{M}\ddot{\boldsymbol{u}})^T d\boldsymbol{u} \tag{1-3}$$

The strain energy is composed of two parts. That is, $E_S = E_S^s + E_S^b$ where E_S^s is the energy consumed to create deformations in the superstructure, while E_S^b is the energy used to make strain in the boundary elements, e.g., soil-foundation system. These two components can be calculated similarly as

$$E_S^{s(b)} = \int_0^T \left(\boldsymbol{f}_S^{s(b)}\right)^T d\boldsymbol{u} \tag{1-4}$$

where $\boldsymbol{f}$ is the resistance force which can be a nonlinear function of deformations. According to this superstructure-boundary decomposition, it is possible to write energy dissipated through damping mechanisms as $E_D = E_D^s + E_D^b$ where E_D^s is the energy dissipated through inherent damping of the superstructure, and E_D^b is the energy dissipated through boundaries, e.g., soil-foundation radiation damping. The latter component can be calculated as

$$E_D^b = \int_0^T \left(\boldsymbol{f}_D^b\right)^T d\boldsymbol{u} \tag{1-5}$$

where $\boldsymbol{f}$ is the damping force at the boundaries. Assuming a Rayleigh model for the inherent damping, the first component can be calculated as

$$E_D^s = \int_0^T (\alpha\mathbf{M}\dot{\boldsymbol{u}})^T d\boldsymbol{u} + \int_0^T (\beta\mathbf{K}^S\boldsymbol{u})^T d\boldsymbol{u} \tag{1-6}$$

where α and β are, respectively, mass and stiffness proportional damping coefficients, and $\mathbf{K}^S$ is the elastic stiffness matrix constructed using superstructure's elements. Note that we used elastic stiffness in Rayleigh damping because we are going to identify an independent damping from real-life which is not dependent on the nonlinear modeling assumptions and accuracy.

Herein, we carry out a series of numerical simulations to see the contribution of each component described above in consuming input energy. To do so, a very detailed numerical model of the San Roque Canyon

(SRC) bridge, which will be extensively studied later, is used. All damping sources mentioned earlier are present in the model. We assumed a Rayleigh model for the inherent damping and we changed its coefficients to cover a range of first and ninth modal damping ratios of 1% to 20%. We also incrementally increased ground motion intensity from 0.05g Peak Ground Acceleration (PGA) to 1.0g.

Figure 1-3 shows the variation of E_K (kinetic energy), E_S^s (strain energy in the structure), E_S^b(strain energy in the boundaries), E_D^s (inherent Rayleigh damping in the structure), and E_D^b (damping energy in the boundaries). To make sure that the calculation is carried out correctly, the input energy is computed directly using Eq. (1-1). As seen in Figure 1-3 where various energy types are plotted on top of each other, the summation of those energy types equals to the directly calculated energy. As seen in this figure, the importance of the inherent damping in low and moderate levels of the ground motion is very significant, while its contribution reduces for very high excitation. Note that, this observation may not be general and could be significantly changed for a different bridge due to the different contribution of the boundaries.

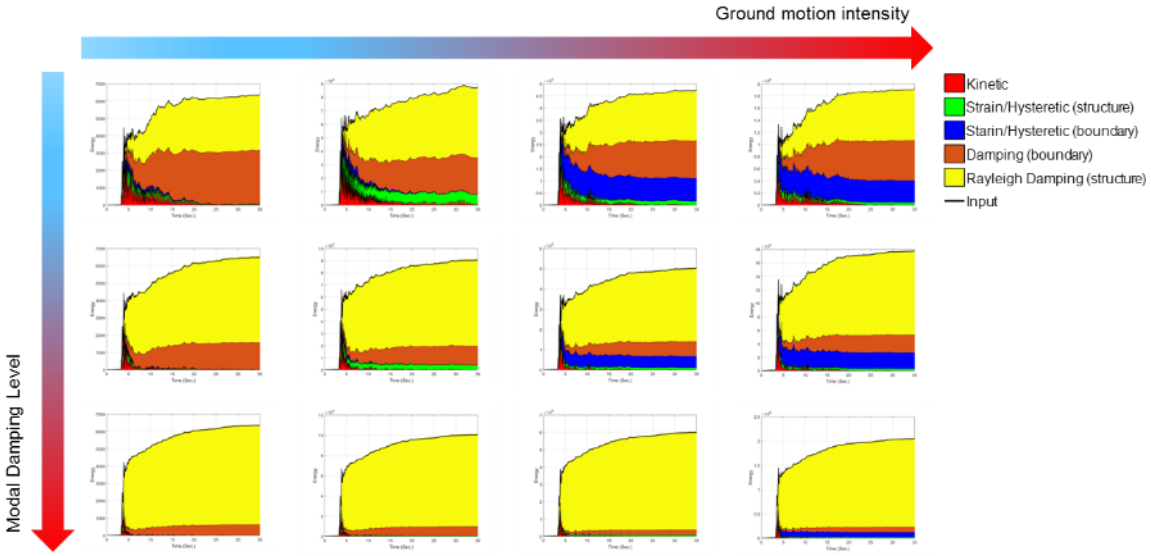

Figure 1-3: Contribution of various energy dissipation sources versus ground motion intensity and inherent damping level.

To be able to talk about the level of contribution in energy dissipation in a more quantitative way, Figure 1-3 is shown in Figure 1-4 where all energy sources are normalized by the input energy. As seen, there is a quite complex behavior is observed. For example, for the lowest level of modal damping, by increasing the level of ground motion, energy dissipated through damping mechanisms at the boundaries reduces and compensated by nonlinear behavior of the superstructure and inherent damping. If the level of excitation highly increases, the bridge structure mostly moves as a rigid body system, so the contribution of the boundaries in the energy dissipation through damping or nonlinear behavior increases. However, if the level

of inherent damping is too high then the variation in the ground motion intensity does not significantly change the contribution of the inherent damping which.

These preliminary analyses, which could itself be the subject of a serious numerical study, show that the problem in hand is a complex problem with various players including superstructure details, level of soil-structure interaction, ground motion intensity, the frequency content of excitation, etc. Anyway, as it can be seen, the inherent damping is a key factor in the dynamic response of the bridge structure whose accurate estimation is an essential task to be able to accurately predict the response of a bridge during a future earthquake.

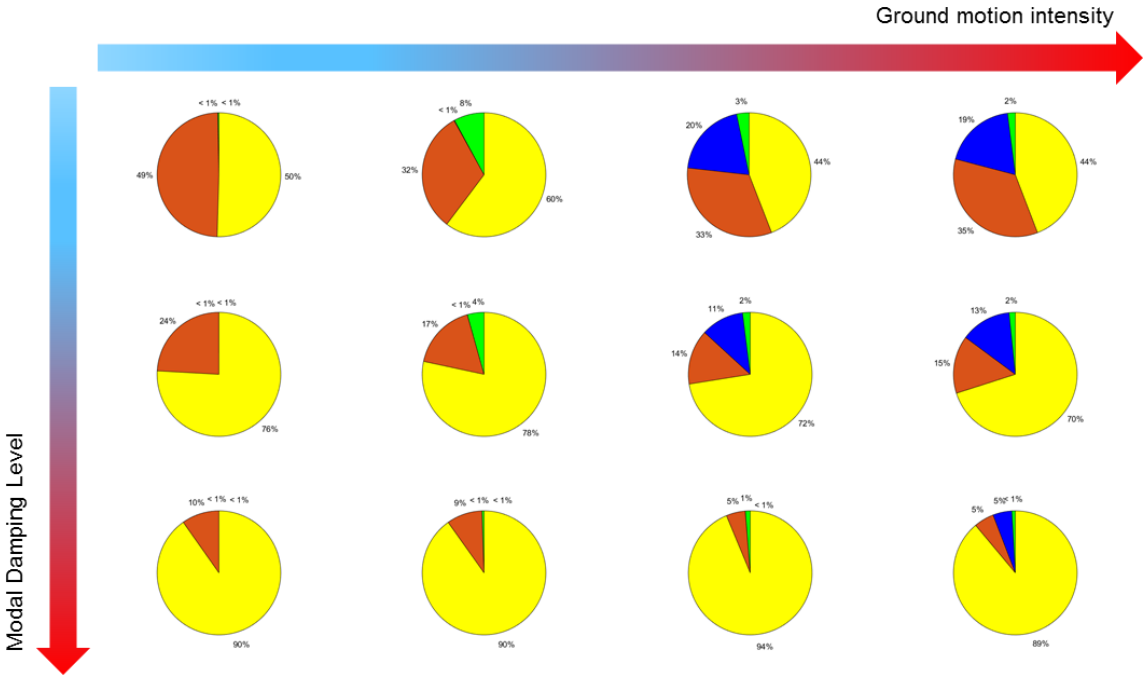

Figure 1-4: Figure 1-3 normalized by the input energy.

1.3. DATA AVAILABILITY

Currently, there are almost 81 instrumented bridges in California which are listed in Table 1-1 and distributed as shown in Figure 1-5. This rich source of data made the authors and sponsor convinced to spend time and resources to develop a robust and reliable methodology to be able to extract as much information as possible from the data. While, a few bridge cases are studied in this report for verification, validation, and application purposes, the procedure can be used on all available data which is continuously increasing in size. However, to be able to make data selection and classification in a systematic way, a specific toolbox with a graphical user interface, called CSMIP-BRIDGE, is developed in Matlab [22]. This

software tool is able to connect to the Center for Engineering Strong Motion Data (CESMD)[2] online database [23] and harvest the metadata of all bridges instrumented through CSMIP. Detailed instruction on how to use the software will be presented in a separate chapter. The current version of this software features capabilities that enable a user to manually update its CSMIP-harvested database. It also features a search form through which bridges with specific characteristics can be selected and grouped together.

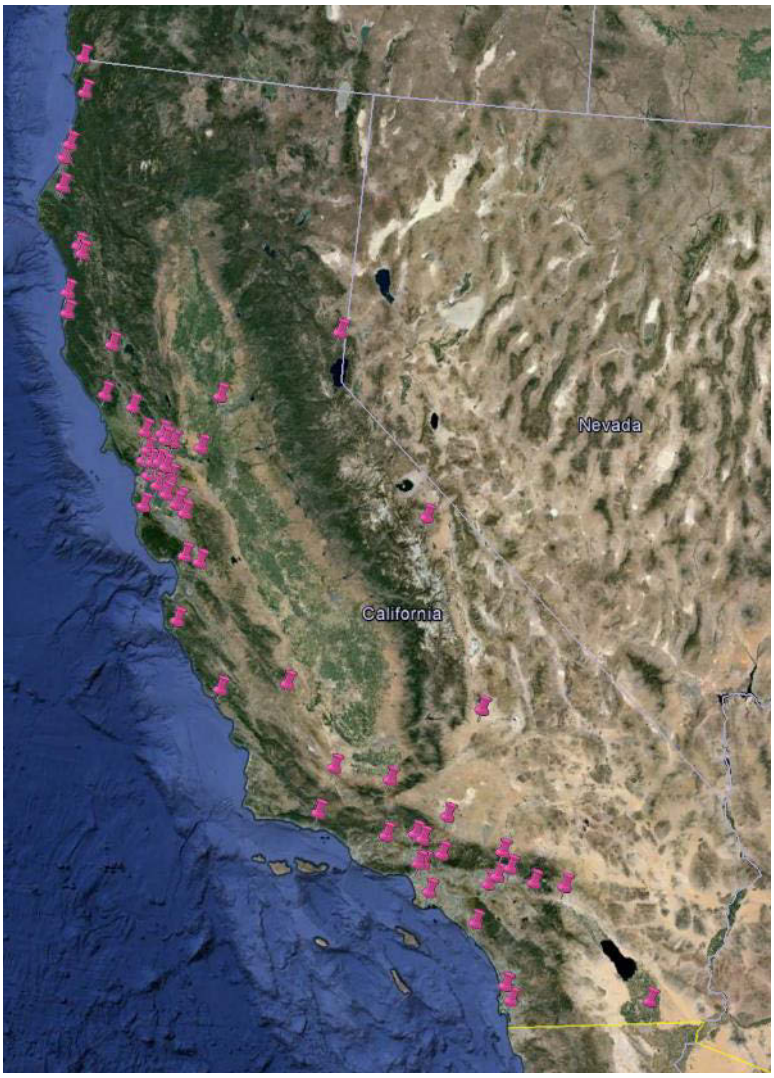

Figure 1-5: Geographic distribution of instrumented bridges in California (last update: 02/04/2016).

Table 1-1: Available instrumented bridges in California (last update: 2017).

No.	CSMIP No.	Name	Network	Photo Availability	Layout Availability	Number of Eqs.	Available Eqs.
1	79683	Albion - Hwy 1/Salmon Creek Bridge	CGS	Yes	Yes	1	1
2	67771	Antioch - San Joaquin River Bridge	CGS	Yes	Yes	2	2

[2] www.strongmotioncenter.org

3	89708	Arcata - Hwy 101/Murray Road Bridge	CGS	Yes	Yes	1	1
4	12649	Beaumont - I10/60 Interchange Bridge	CGS	Yes	Yes	3	2
5	68322	Benicia - Martinez/I680 East Bridge	CGS	Yes	Yes	1	1
6	68682	Benicia - Martinez/I680 West Bridge	CGS	Yes	Yes	1	1
7	47729	Big Sur - Hwy 1/Pfeiffer Canyon Bridge [demol]	CGS	Yes	Yes	2	2
8	13795	Capistrano Beach - I5/Via Calif. Bridge	CGS	Yes	Yes	5	5
9	13705	Corona - I15/Hwy91 Interchange Bridge	CGS	Yes	Yes	5	3
10	99190	Crescent City - Hwy 101/Smith Rvr Bridge	CGS	Yes	Yes	2	2
11	25758	Cuyama - Hwy 166/Cuyama River Bridge	CGS	Yes	Yes	1	0
12	23650	Devore - I15/215 Interchange Bridge	CGS	Yes	Yes	1	1
13	1336	El Centro - Hwy8/Meloland Overpass	CGS	Yes	Yes	14	13
14	89736	Eureka - Eureka Channel Bridge	CGS	Yes	Yes	10	9
15	89735	Eureka - Middle Channel Bridge	CGS	Yes	Yes	8	7
16	89686	Eureka - Samoa Channel Bridge	CGS	Yes	Yes	11	10
17	79296	Fort Bragg - Hwy 1/Noyo River Bridge	CGS	Yes	Yes	1	1
18	57595	Fremont - Channel B Bridge	CGS	Yes	Yes	1	1
19	24775	Grapevine - I5/Lebec Rd Bridge	CGS	Yes	Yes	3	3
20	58754	Half Moon Bay - Hwy 1/Tunitas Cr. Bridge	CGS	Yes	Yes	3	3
21	58501	Hayward - BART Elevated Section	CGS	Yes	Yes	1	1
22	58658	Hayward - Hwy 580/238 Interchange Bridge	CGS	Yes	Yes	3	3
23	58799	Hayward - San Mateo Bridge Trestle	CGS	Yes	Yes	1	1
24	69760	Hopland - Hwy 101/Railroad Bridge	CGS	Yes	Yes	2	2
25	69671	Jenner - Hwy 1/Russian River Bridge	CGS	Yes	Yes	1	1
26	99710	Klamath - Hwy 101/Klamath River Bridge	CGS	Yes	Yes	1	1
27	54730	Lake Crowley - Hwy 395 Bridge	CGS	Yes	Yes	5	5
28	79761	Leggett - Big Dann Bridge	CGS	Yes	Yes	1	0
29	79757	Leggett - Cedar Creek Bridge	CGS	Yes	Yes	2	1
30	79421	Leggett - Hwy 101/Confusion Hill Bridge	CGS	Yes	Yes	2	2
31	24670	Los Angeles - I10/405 Interchange Bridge	CGS	Yes	Yes	1	1
32	24704	Los Angeles - I10/La Cienega Bridge	CGS	Yes	Yes	3	3
33	14406	Los Angeles - Vincent Thomas Bridge	CGS	Yes	Yes	6	6
34	24738	Moorpark - Hwy 23/118 Bridge	CGS	Yes	Yes	2	2
35	12666	North Palm Springs - I10/Hwy 62 Bridge	CGS	Yes	Yes	3	2
36	68778	Novato - Hwy37/Petaluma River Bridge	CGS	Yes	Yes	3	3
37	58656	Oakland - Hwy 580/13 Interchange Bridge	CGS	Yes	Yes	1	1
38	58657	Oakland - Hwy 580/24 Interchange Bridge	CGS	Yes	Yes	5	5
39	58600	Oakland - SF Bay Bridge/East: SAS	CGS	Yes	Yes	2	2
40	58601	Oakland - SF Bay Bridge/East: Skyway	CGS	Yes	Yes	3	3
41	58602	Oakland - SF Bay Bridge/East: YBITS	CGS	Yes	Yes	2	2
42	24706	Palmdale - Hwy 14/Barrel Springs Bridge	CGS	Yes	Yes	4	4
43	36668	Parkfield - Hwy 46/Cholame Creek Bridge	CGS	Yes	Yes	2	2
44	24689	Pasadena - I210/Hwy134 Interchnge Bridge	CGS	Yes	Yes	5	5
45	58258	Richmond - San Rafael Bridge	CGS	Yes	Yes	1	0
46	33742	Ridgecrest - Hwy 395/Brown Road Bridge	CGS	Yes	Yes	1	0
47	89973	Rio Dell - Hwy 101/Eel River Bridge	CGS	Yes	Yes	23	23
48	89324	Rio Dell - Hwy 101/Painter St. Overpass	CGS	Yes	Yes	18	17
49	5235	Riverside; Santa Ana River Bridge	USGS	Yes	No	1	1
50	68717	Rohnert Park - Hwy 101 Bridge	CGS	Yes	Yes	4	4
51	23631	San Bernardino - I10/215 Interchange Br	CGS	Yes	Yes	9	9
52	3679	San Diego - Coronado Bridge	CGS	Yes	Yes	2	2
53	3731	San Diego - I5/Hwy 52 Interchange Bridge	CGS	Yes	Yes	2	2
54	24714	San Fernando - I210/Hwy 118 Bridge	CGS	Yes	Yes	3	3
55	58632	San Francisco - Bay Bridge/West	CGS	Yes	Yes	5	4
56	58700	San Francisco - Golden Gate Bridge	CGS	Yes	Yes	6	5
57	58596	San Francisco Bay - Dumbarton Bridge	CGS	Yes	Yes	2	2
58	1571	San Jose; Interchange 101/280/680	USGS	Yes	No	1	1
59	47315	San Juan Bautista - Hwy 101/156 Overpass	CGS	Yes	Yes	10	10
60	58677	San Mateo - San Mateo Bridge	CGS	Yes	Yes	1	1
61	37728	San Simeon - Hwy 1/San Simeon Crk Bridge	CGS	Yes	Yes	2	2
62	25749	Santa Barbara - San Roque Canyon Bridge	CGS	Yes	Yes	4	4
63	57748	Santa Clara - Hwy 237/Alviso Overpass	CGS	Yes	Yes	3	3
64	58536	South San Francisco - Sierra Pt Overpass	CGS	Yes	Yes	1	1
65	24694	Sylmar - I5/14 Interchange Bridge	CGS	Yes	Yes	2	1
66	76741	Truckee - I80/Truckee River Bridge	CGS	Yes	Yes	4	4
67	68184	Vallejo - Carquinez/I80 East Bridge	CGS	Yes	Yes	1	1
68	68185	Vallejo - Carquinez/I80 West Bridge	CGS	Yes	Yes	1	1
69	68065	Vallejo - Hwy 37/Napa River Bridge	CGS	Yes	Yes	3	3
70	47707	Watsonville - Hwy1/Struve Slough Bridge	CGS	Yes	Yes	2	2
71	67972	West Sacramento - I80/Yolo Causeway	CGS	Yes	Yes	1	1
72	58678	Belmont - I280 Pedestrian Bridge	CGS	Yes	Yes	0	0
73	22503	Big Bear Lake - Hwys 18 & 38 Bridge	CGS	Yes	Yes	0	0
74	26917	Lompoc - Hwy 1/El Jaro Creek Bridge	CGS	Yes	Yes	0	0
75	14690	Los Angeles - I405/San Gabriel River Br	CGS	Yes	Yes	0	0
76	34715	Mojave - Hwy 14/Railroad Bridge	CGS	Yes	Yes	0	0
77	25324	Oxnard - Hwy 101/Santa Clara Rvr Bridge	CGS	Yes	No	0	0
78	58414	Pacifica - Hwy1/Devils Slide Bridge	CGS	No	No	0	0
79	88194	Redding - I5/Shasta Lake Bridge	CGS	Yes	Yes	0	0
80	88638	Shasta Lake - I5/Antlers Bridge	CGS	No	No	0	0
81	25725	Ventura - Hwy101/Telephone Rd. Bridge	CGS	Yes	Yes	0	0

CHAPTER 2: CSMIP-BRIDGE SOFTWARE

2.1. INTRODUCTION

To be able to classify bridges in a systematic and extendable way, we developed a Matlab [104] toolbox which is called CSMIP-BRIDGE. This toolbox is able to connect to the Center for Engineering Strong Motion Data (CESMD)[3] and classify the available data. The CSMIP-CIT can be used to search for and retrieve data using different criteria such as the number of earthquakes, PGA value, number of instrumented locations, etc.

2.2. HOW TO RUN CSMIP-BRIDGE?

CSMIP- BRIDGE is delivered as a standalone executable file CSMIP-BRIDGE.exe. This software is originally written in Matlab 2016a on a Windows platform. Therefore, users must run it on Windows with compatible MATLAB Compiler Runtime (MCR) installed. Additionally, the CSMIP-BRIDGE executable requires *Ghostscript* for Windows[4] to be installed. CSMIP-BRIDGE employs Ghostscript to display bridge layouts as embedded images. User must install it and insert its directory address prior to running CSMIP-BRIDGE, as will be described in 2.3.1.

Remark: an Executable file is a compact form and MCR unpacks it when the user runs the CSMIP-BRIDGE for the first time. So, it may take ~30 seconds to CSMIP-BRIDGE shows up in the first time run. So long as the user does not restart the computer, this time decreases to ~5 seconds for the next tries.

2.3. OVERVIEW

A general overview of the software is shown in Figure 2-1. CSMIP-BRIDGE comprises THREE major modules, which can work together or independently:

- **Update module**: Using this module, it is possible to connect to CESMD and collect metadata of all bridges. After running this module for the first time, it is possible to use the *offline* option to read metadata from a locally saved database without repeating the downloading process from CESMD.

- **Modify module**: Some types of information about the bridges cannot be automatically detected from layouts or photos. As such, a Modify module is provided to allow the users to insert metadata manually. These additional metadata are also saved for future use.

---

[3] www.strongmotioncenter.org

[4] Ghostscript is available at http://www.ghostscript.com.

- **Search module**: This module provides a multi-criteria search capability over data collected and updated with two previous modules. This and two previous modules together comprise the "Classification" part of CSMIP-BRIDGE.

Details of each module are provided in the following chapters.

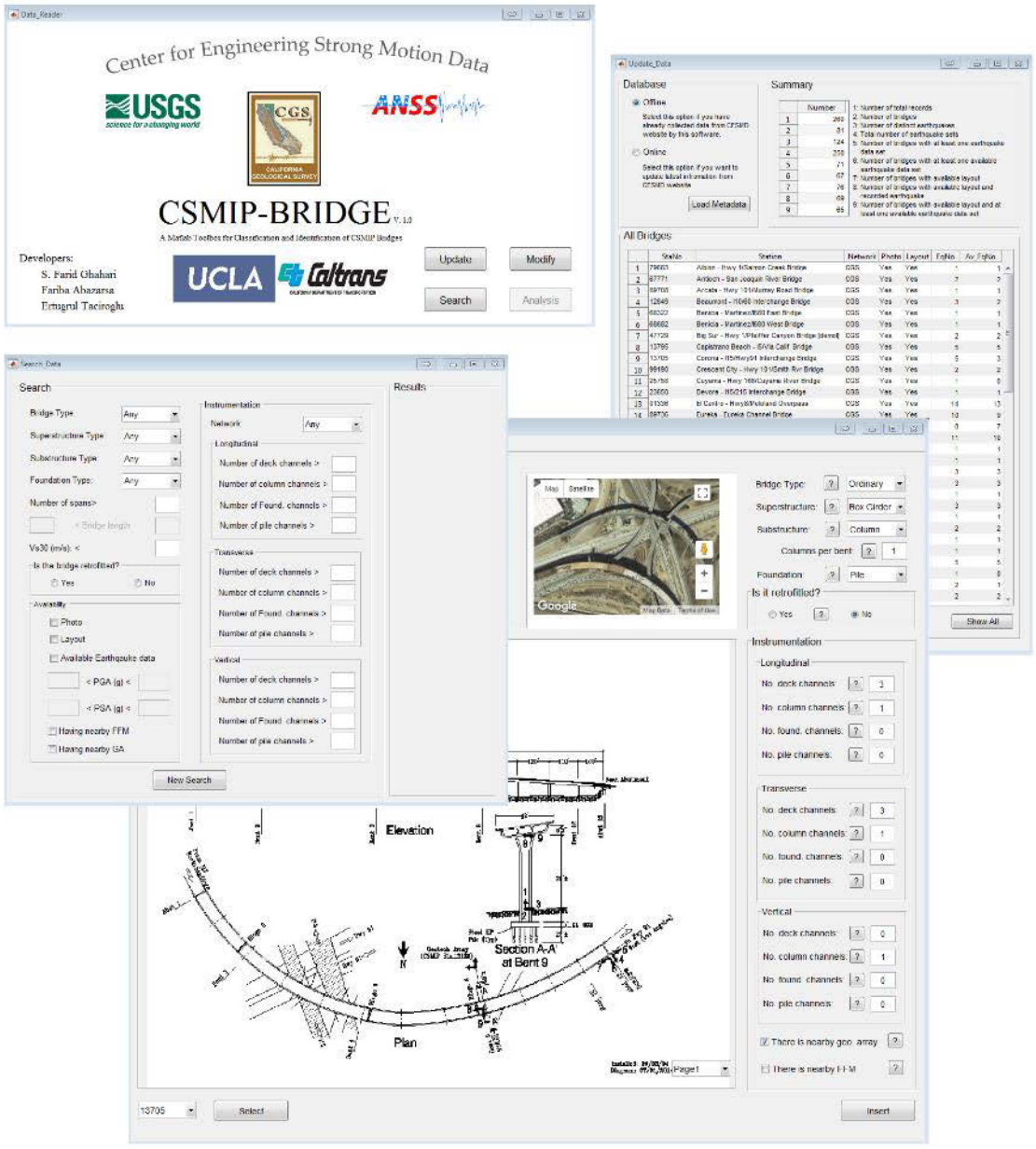

Figure 2-1: CSMIP-BRIDGE's graphical user interface and information windows.

2.3.1 "Update" Module

This section describes how to read bridge metadata and save them for future use. A new window (see, Figure 2-2) appears upon clicking the "Update" button. In the "Database" panel, the user must choose

whether metadata can be read from an available offline database or not. If the user has run the software previously, then the necessary information is already available on the current directory of the CSMIP-BRIDGE software. These files and folders are:

- A "Layouts" folder, which contains the instrumentation layouts of all bridges;
- A "Photos" folder, which contains bridge photos;
- Two files labeled as "Table.mat" and "Data.mat" containing the bridges metadata read from the CESMD data center.

Let us assume that the necessary information is already available, and the user has chosen the "offline" option. By pushing the "Load Metadata" button, a summary of all information will be displayed in the "Summary" table, as shown in Figure 2-2. A description of each row is briefly written alongside[5]. Additionally, the "Show All" button provides a list of all of the bridges along with their information such as station name, network, number of earthquakes, etc. (Figure 2-2).

[5] For example, at the time of the writing of this user's manual, there were 81 instrumented bridges in the CESMD.

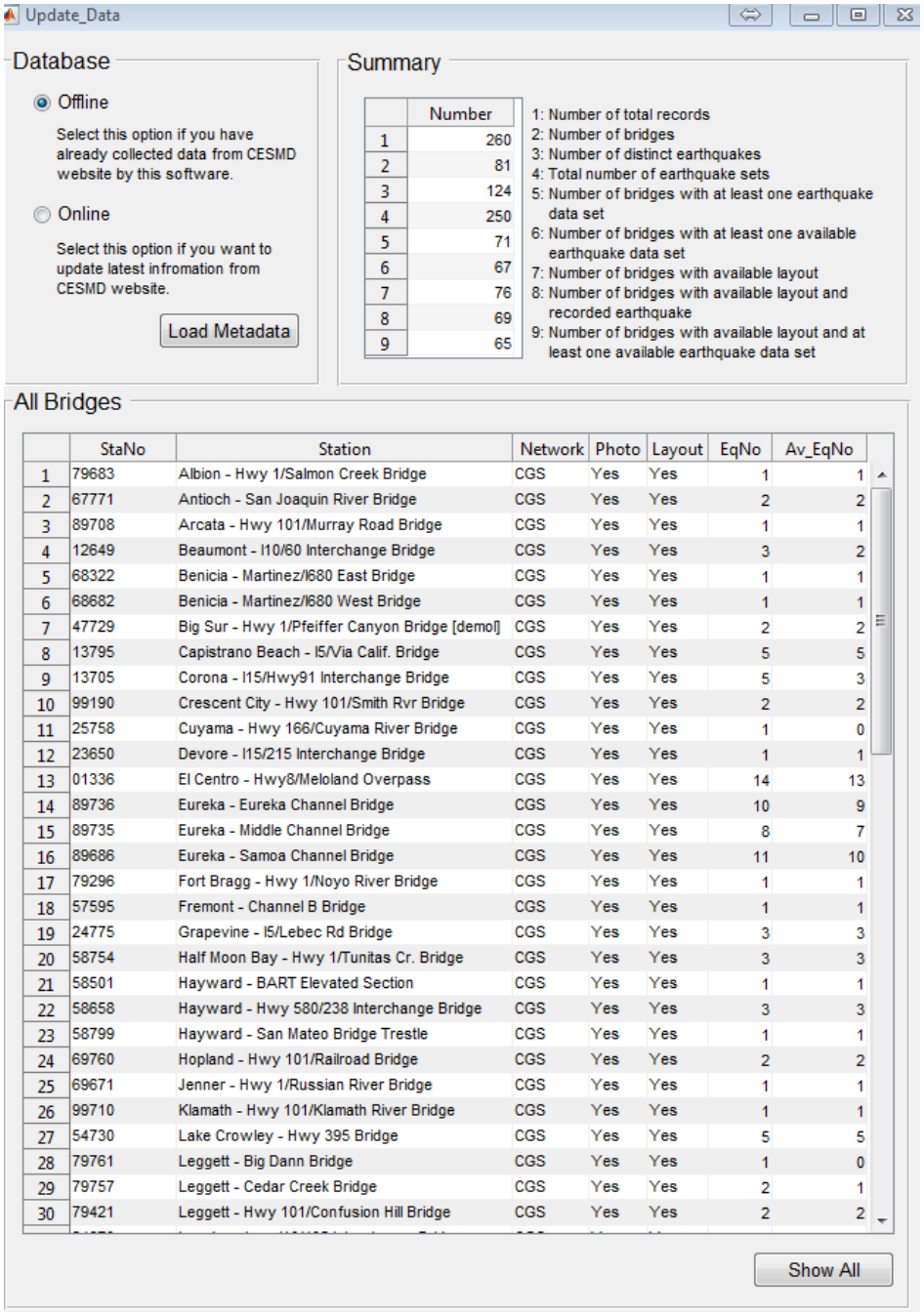

Figure 2-2: the *Update* window.

Now assume that this is the first time the user runs the software (or assume that the user wants to have the most up-to-date information/data). There is an "Online" option in the "Update" window. By selecting this option and by clicking the "Load Metadata" button, CSMIP-BRIDGE is invoked to connect to the CESMD data center through the Internet. During this process, CSMIP- BRIDGE also tries to internally convert the instrumentation layouts of buildings from their nominal PDF format (available in CESMD) to

the PNG format so that they can be shown on the CSMIP- BRIDGE plots. This conversion is carried out through the third-party software Ghostscript. By pushing the "Load Metadata" under the "Online" option, CSMIT-BRIDGE asks the user to locate the folder containing "gswin64c.exe" or "gswin32c.exe." Having installed the proper Ghostscript version, the user must provide CSMIP-BRIDGE with the address of this folder—e.g., C:\Program Files\gs\gs9.16\bin. After this step, CSMIP-BRIDGE collects metadata of all available bridges and displays the summary in the "Summary" table. Note that depending on the number of records at CESMD, this step may take several minutes. Again, the details of all bridges can be obtained by clicking the "Show All" button.

2.3.2 "Modify" Module

By completing the updating step, metadata of all bridges are compiled into the Table.mat and Data.mat files, and under two folders (Layouts and Photos) in the same directory as CSMIP-BRIDGE. Although most of the metadata are read from information available at CESMD, they are not complete and additional information needs to be inserted into the software's database for future use by the "Search" module. To do so, a "Modify" module is implemented in CSMIP-BRIDGE. By pressing the "Modify" button at the main page, a new window —i.e., the "Modify" module—appears as shown in the upper-left part of Figure 2-3.

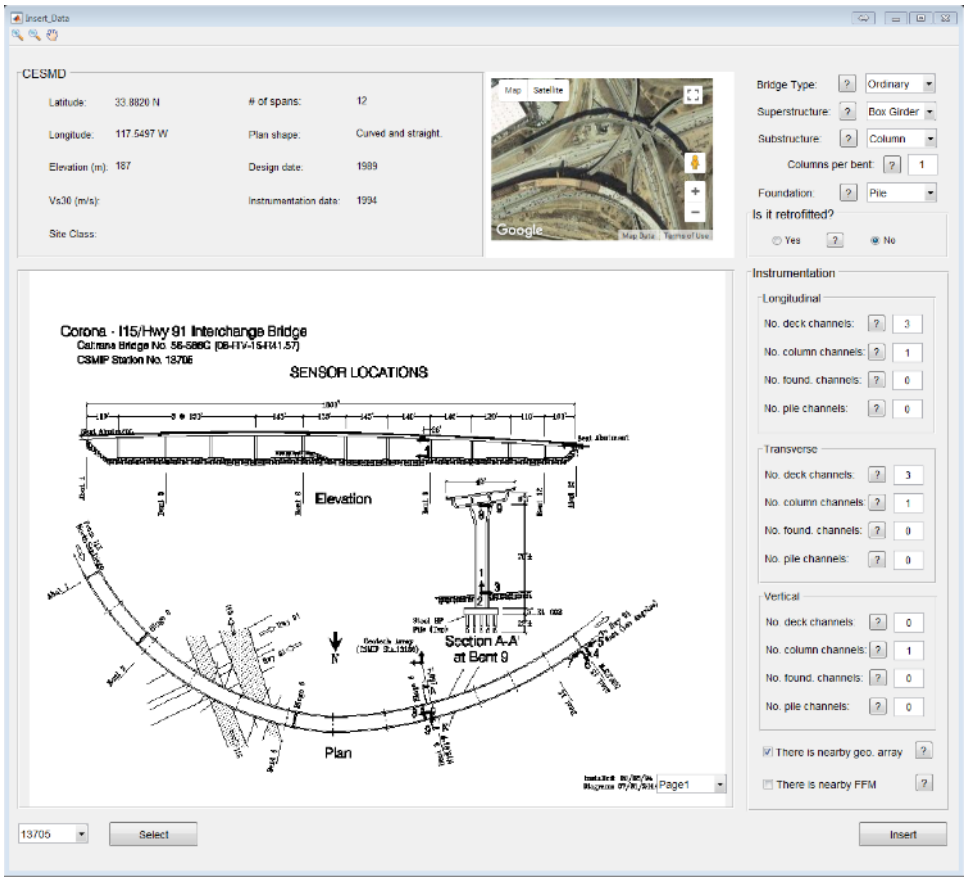

Figure 2-3: the *Modify* module.

A complete list of bridges is available in the popup menu on the lower-left part of the "Modify" form wherein each bridge is listed by its corresponding CSMIP Station number. If this the first time the user runs this module and has not added any additional information to the software, then all bridges in the menu are shown with two asterisks. If the user chooses a bridge from the list and presses the "Select" button, then the form is updated with the metadata of the bridges retrieved from CESMD through the "Update" module. As will be seen, a 3D Google view of the bridge is shown on the top, and the instrumentation layout (if available) is shown at the center of the form. Some preliminary metadata about the bridge—such as latitude, longitude, height, design date, etc.—are also read from CESMD and displayed on the upper-left of the form. As this was the first time of applying the "Modify" form to the bridge (note that the bridge had two asterisks), the fields on the right-side of the form are blank. The user must provide this needed information. A definition of each case can be obtained by clicking the nearby small help "?" button.

After inserting the new information by pressing the "Insert" button, the two asterisks are removed from the CSMIP number of the bridge. This process must be manually carried out for *all* bridges. However, the said additional data are already provided by the developers of CSMIP-BRIDGE, and delivered with the software. Note that, for bridges added to the database after the last CSMIP-BRIDGE update release (currently, 2017), the user must provide this type of information manually. Bridges with missing metadata can be easily identified because they will be displayed with two asterisks.

It is important to note that there are a few bridges in the CESMD center, for which no instrumentation layout is available. For those cases, the users should leave the form as-is and only press the "Insert" button. This action removes one of their asterisks, thereby marking these bridges as being different from the *newly added* bridges.

2.3.3 "Search" Module

The main purpose of developing CSMIP-BRIDGE was to create a systematic tool through which we can choose bridges with specific properties. This is essential if we need to have aggregated information using lots of bridge's data, e.g., developing a formula for inherent damping using identified damping values from lots of bridges having different characteristics. Having loaded metadata from the CESMD center through "Update" module and also adding extra information through "Modify" module, "Search" module is now able to search through available information and find bridges with specific properties desired by the user. As shown in Figure 2-4, many items are considered for "Search" module.

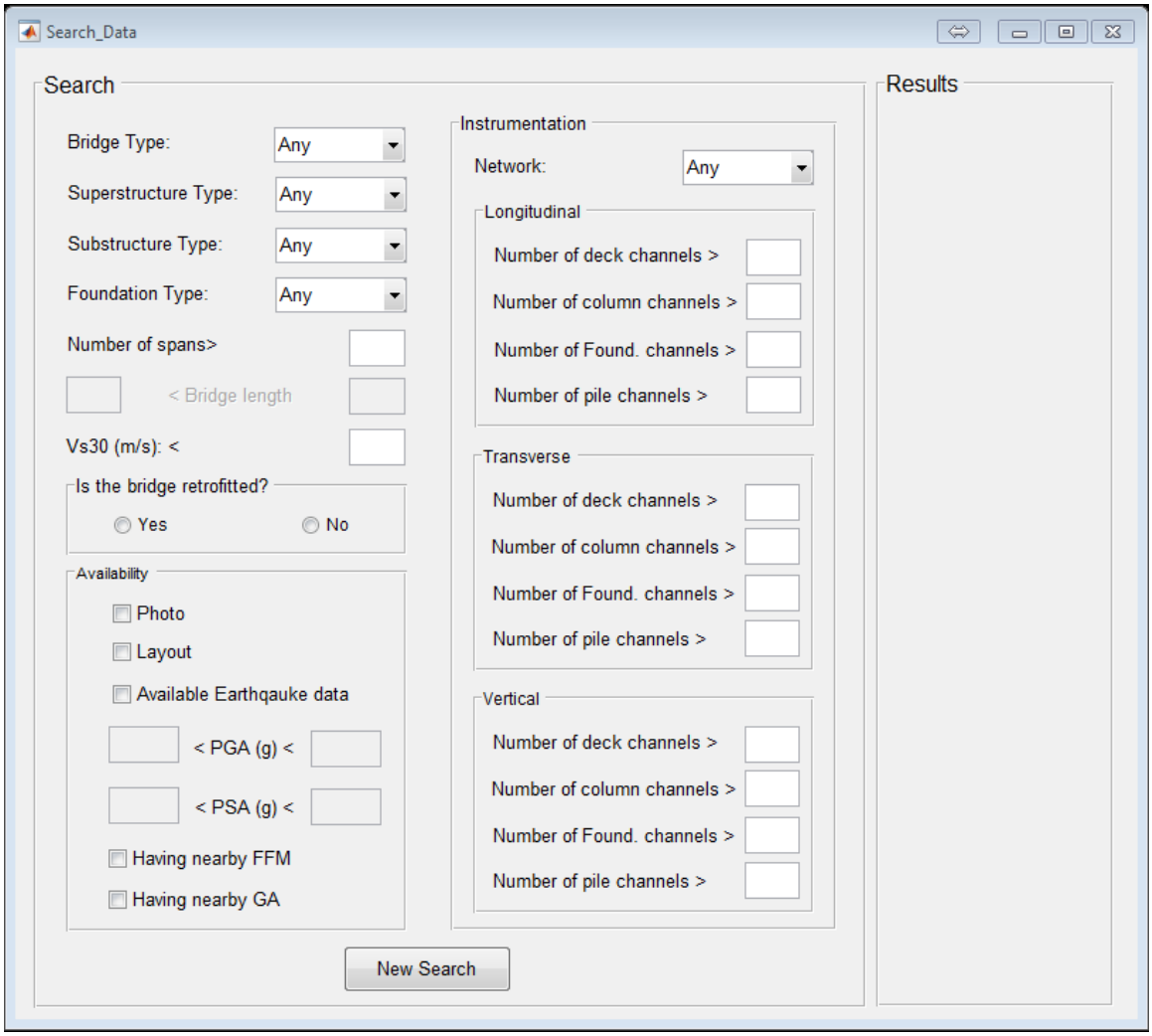

Figure 2-4: the *Search* module.

CHAPTER 3: OUTPUT-ONLY IDENTIFICATION

3.1. INTRODUCTION

In this chapter, the previously outlined output-only identification method is presented in detail. We first derive equations of motion of a bridge structure under multiple FIMs in both relative and absolute coordinates. The former is usually used in forward analyses of structural dynamics, and the second one is needed for identification purposes because we are only able to measure absolute responses in the real world. Next, we briefly review the joint state-system-input identification method originally developed by Huang et al. [24]. As it will be shown through a synthetic example, that method theoretically is able to solve our problem—i.e., joint identification of system-input of a bridge structure. However, it is not applicable to large-scale structures due to its high computational expense and its embedded linearity assumption. To resolve these issues, we assume that the FE model is accurate, so we dissolve state equation into the observation equation and then carry out a Sequential Bayesian estimation [25] using an Unscented Kalman Filter [26].

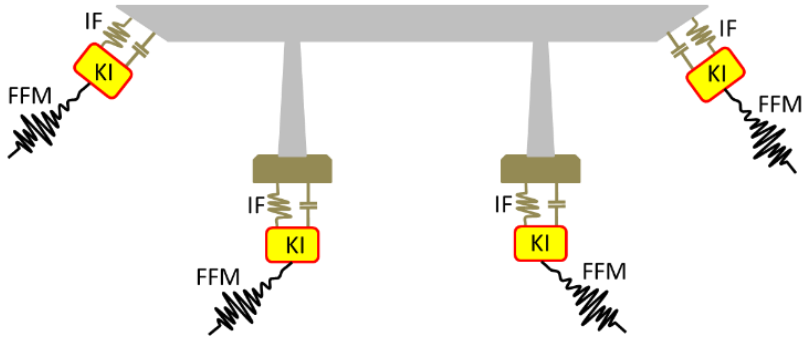

Figure 3-1: a Lumped model of a multi-span bridge.

3.2. EQUATIONS OF MOTION OF A SOIL-FOUNDATION-STRUCTURE SYSTEM SUBJECT TO MULTIPLE FIMS

A schematic representation of the problem under study is shown in Figure 3-1. As seen, the bridge structure is subjected to several different unknown Free-Field Motions (FFMs) at its piers. These FFMs are first converted to FIMs through yet-unknown Kinematic Interaction (KI) filters and excite the bridge that is supported on flexible soil-foundation Impedance Functions (IFs). Herein, we assume that an initial

(*uncertain*) Finite Element (FE) model of the bridge supported on *uncertain* IFs is available. Also, responses of the system at several locations on the bridge and foundation are measured as absolute accelerations through the sensors. In what follows, a novel method will be described with which unknown FIMs, IFs, and the unknown parameters of the superstructure are all identified simultaneously along with their uncertainties.

The equation of dynamic equilibrium for all the Degrees-Of-Freedom (DOFs) n structure-foundation and n_g foundation-soil DOFs) is written in a partitioned form as [27]

$$\begin{bmatrix} \mathbf{M} & \mathbf{M}_g \\ \mathbf{M}_g{}^T & \mathbf{M}_{gg} \end{bmatrix} \begin{Bmatrix} \ddot{\boldsymbol{x}}(t) \\ \ddot{\boldsymbol{x}}_{\boldsymbol{g}}(t) \end{Bmatrix} + \begin{bmatrix} \mathbf{D} & \mathbf{D}_g \\ \mathbf{D}_g{}^T & \mathbf{D}_{gg} \end{bmatrix} \begin{Bmatrix} \dot{\boldsymbol{x}}(t) \\ \dot{\boldsymbol{x}}_{\boldsymbol{g}}(t) \end{Bmatrix} + \begin{bmatrix} \mathbf{K} & \mathbf{K}_g \\ \mathbf{K}_g{}^T & \mathbf{K}_{gg} \end{bmatrix} \begin{Bmatrix} \boldsymbol{x}(t) \\ \boldsymbol{x}_{\boldsymbol{g}}(t) \end{Bmatrix} = \begin{Bmatrix} \mathbf{0} \\ \mathbf{P}_g(t) \end{Bmatrix} \tag{3-1}$$

where $\mathbf{M}$, $\mathbf{D}$, and $\mathbf{K}$ are $n \times n$ mass, damping, and stiffness matrices of the foundation-structure, respectively. Matrices $\mathbf{M}_g$, $\mathbf{D}_g$, and $\mathbf{K}_g$ are $n \times n_g$ mass, damping, and stiffness matrices of the foundation-soil interface, while $\mathbf{M}_{gg}$, $\mathbf{D}_{gg}$, and $\mathbf{K}_{gg}$ matrices are related to soil's DOFs. In Eq. (3-1), $\boldsymbol{x}(t)$ is a vector that contains the absolute displacement response of all n structure-foundation DOFs, while $\dot{\boldsymbol{x}}(t)$, and $\ddot{\boldsymbol{x}}(t)$ are their corresponding velocity and acceleration vectors. $\boldsymbol{x}_g(t) = \begin{bmatrix} x_{g,1}(t) & \cdots & x_{g,n_g}(t) \end{bmatrix}^T$ and its time derivatives $\dot{\boldsymbol{x}}_g(t)$ and $\ddot{\boldsymbol{x}}_g(t)$ are vectors containing the prescribed Foundation Input Motions (FIMs) as displacement, velocity, and acceleration at all n_g foundation-soil interface DOFs. As there is no external force on the structure-foundation DOFs, the only forces needed for applying FIMs are $\mathbf{P}_g(t)$, as shown in Eq. (3-1).

The absolute displacement of the bridge (structure-foundation) can be written as the superposition of displacement produced by the static application of the prescribed FIMs at each time instant $\boldsymbol{u}^s(t)$ and the dynamic response with respect to the statically deformed position $\boldsymbol{u}(t)$ as

$$\begin{Bmatrix} \boldsymbol{x}(t) \\ \boldsymbol{x}_g(t) \end{Bmatrix} = \begin{Bmatrix} \boldsymbol{u}^s(t) \\ \boldsymbol{x}_g(t) \end{Bmatrix} + \begin{Bmatrix} \boldsymbol{u}(t) \\ \mathbf{0} \end{Bmatrix}. \tag{3-2}$$

As $\boldsymbol{u}^s(t)$ is produced by static deformation of the bridge under static application of $\boldsymbol{x}_g(t)$, their relationships are governed by static equilibrium as follows

$$\begin{bmatrix} \mathbf{K} & \mathbf{K}_g \\ \mathbf{K}_g{}^T & \mathbf{K}_{gg} \end{bmatrix} \begin{Bmatrix} \boldsymbol{u}^s(t) \\ \boldsymbol{x}_g(t) \end{Bmatrix} = \begin{Bmatrix} \mathbf{0} \\ \mathbf{P}_g^s(t) \end{Bmatrix} \tag{3-3}$$

where $\mathbf{P}_g^s(t)$ is needed force at each time to impose $\boldsymbol{x}_g(t)$. It is trivial that $\mathbf{P}_g^s(t)$ would be zero if the system is statically determinate or all foundation-soil interface nodes move in a compatible manner (e.g., identical horizontal FIMs).

The first partition of Eq. (3-1) can be rewritten using the aforementioned static and dynamic parts as

$$\mathbf{M}\,\ddot{\boldsymbol{u}}(t) + \mathbf{D}\,\dot{\boldsymbol{u}}(t) + \mathbf{K}\,\boldsymbol{u}(t) = -\left[\mathbf{M}\,\ddot{\boldsymbol{u}}^{s}(t) + \mathbf{M}_g\ddot{\boldsymbol{x}}_g(t)\right] - \left[\mathbf{D}\,\dot{\boldsymbol{u}}^{s}(t) + \mathbf{D}_g\dot{\boldsymbol{x}}_g(t)\right]. \tag{3-4}$$

The term $\left[\mathbf{K}\,\boldsymbol{u}^{s}(t) + \mathbf{K}_g\boldsymbol{x}_g(t)\right]$ has been removed from right-hand-side of the equation above, because it is zero, based on the first partition of Eq. (3-3). In Eq. (3-4), it is more favorable to replace the quasi-static velocity and acceleration using their FIM counterparts, because of $\mathbf{K}\,\boldsymbol{u}^{s}(t) + \mathbf{K}_g\boldsymbol{x}_g(t) = \mathbf{0}$. So, Eq. (3-4) can be rewritten

$$\mathbf{M}\,\ddot{\boldsymbol{u}}(t) + \mathbf{D}\,\dot{\boldsymbol{u}}(t) + \mathbf{K}\,\boldsymbol{u}(t) = -\left[\mathbf{M}\,\mathbf{L} + \mathbf{M}_g\right]\ddot{\boldsymbol{x}}_g(t) - \left[\mathbf{D}\,\mathbf{L} + \mathbf{D}_g\right]\dot{\boldsymbol{x}}_g(t) \tag{3-5}$$

where $\mathbf{L} = -\mathbf{K}^{-1}\mathbf{K}_g$ is an $n \times n_g$ influence matrix. Each column of the matrix $\mathbf{L}$, say $\boldsymbol{l}_l$, is a vector that assigns the influence of each input acceleration, $x_{g,l}(t)$, on the system's response; and is a function of internal and boundary stiffnesses. Damping term in Eq. (3-5) is usually small relative to the inertia term, and maybe dropped (it is exactly zero when damping matrices are stiffness-proportional). Moreover, for lumped mass systems, the mass matrix is diagonal and the off-diagonal matrix $\mathbf{M}_g$ will be zero. So, Eq. (3-5) can be written in its final form as

$$\mathbf{M}\,\ddot{\boldsymbol{u}}(t) + \mathbf{D}\,\dot{\boldsymbol{u}}(t) + \mathbf{K}\,\boldsymbol{u}(t) = -\mathbf{M}\,\mathbf{L}\ddot{\boldsymbol{x}}_g(t). \tag{3-6}$$

Finally, by replacing $\boldsymbol{u}(t)$ by $\boldsymbol{x}(t) - \boldsymbol{u}^{s}(t)$ in Eq. (3-6), equation of motion can be expressed in an absolute framework as

$$\mathbf{M}\,\ddot{\boldsymbol{x}}(t) + \mathbf{D}\,\dot{\boldsymbol{x}}(t) + \mathbf{K}\,\boldsymbol{x}(t) = \mathbf{D}\,\mathbf{L}\,\dot{\boldsymbol{x}}_g(t) + \mathbf{K}\,\mathbf{L}\,\boldsymbol{x}_g(t) \tag{3-7}$$

3.3. QUADRATIC SUM-SQUARES ERROR MINIMIZATION

Eq. (3-7) can be written in the state-space as

$$\dot{\boldsymbol{z}}(t) = \mathbf{A}_c\,\boldsymbol{z}(t) + \mathbf{B}_c\,\boldsymbol{f}(t) + \boldsymbol{w}(t) \tag{3-8}$$

where $\boldsymbol{z}(t) = [\boldsymbol{x}(t)^T \quad \dot{\boldsymbol{x}}(t)^T]^T$ is a $2n \times 1$ state vector, $\boldsymbol{f}(t) = \left[\boldsymbol{x}_g(t)^T \quad \dot{\boldsymbol{x}}_g(t)^T\right]^T$ is a $2n_g \times 1$ excitation vector, and the continuous-time transition and input matrices $\mathbf{A}_c$ and $\mathbf{B}_c$ are defined as

$$\mathbf{A}_c = \begin{bmatrix} \mathbf{0} & \mathbf{I} \\ -\mathbf{M}^{-1}\mathbf{K} & -\mathbf{M}^{-1}\mathbf{D} \end{bmatrix}, \tag{3-9}$$

$$\mathbf{B}_c = \begin{bmatrix} \mathbf{0} \\ [\mathbf{M}^{-1}\mathbf{K}\,\mathbf{L}, \mathbf{M}^{-1}\mathbf{D}\,\mathbf{L}] \end{bmatrix}. \tag{3-10}$$

Above, $\boldsymbol{w}(t)$ is the model noise (uncertainty) vector with zero mean and covariance matrix $\mathbf{Q}$. Absolute acceleration at any discrete-time instant i can be related to the state and FIMs as

$$\boldsymbol{y}[i] = \mathbf{E}\,\boldsymbol{z}[i] + \mathbf{F}\,\boldsymbol{f}[i] + \boldsymbol{v}[i], \tag{3-11}$$

where

$$\mathbf{E} = \mathbf{V}\,[-\mathbf{M}^{-1}\mathbf{K} \quad -\mathbf{M}^{-1}\mathbf{D}], \tag{3-12}$$

$$\mathbf{F} = \mathbf{V}\,[\mathbf{M}^{-1}\mathbf{K}\,\mathbf{L} \quad \mathbf{M}^{-1}\mathbf{D}\,\mathbf{L}], \tag{3-13}$$

where $\mathbf{V}$ is an $l \times n$ matrix containing 1's and 0's to show which DOFs are being measured. $\boldsymbol{v}[i]$ is a measurement noise vector that is assumed to be Gaussian zero-mean white with covariance matrix $\mathbf{R}$. The vector $\boldsymbol{v}[i]$ represents the difference between the exact prediction, $\boldsymbol{h}[i] = \mathbf{E}\,\boldsymbol{z}[i] + \mathbf{F}\,\boldsymbol{f}[i]$ and the real-life measurement $\boldsymbol{y}[i]$ —i.e., $\boldsymbol{v}[i] = \boldsymbol{y}[i] - \boldsymbol{h}[i]$. According to the assumptions considered for this measurement noise, its Probability Distribution Function (PDF) can be expressed as

$$P(v) = \frac{1}{(2\pi)^{l/2}|\mathbf{R}|^{0.5}}\, e^{-\frac{1}{2}\boldsymbol{v}^T\mathbf{R}^{-1}\boldsymbol{v}} \tag{3-14}$$

where $|.|$ denotes a determinant. Let's put all of the system's uncertain parameters (superstructure and IF parameters) into a vector $\boldsymbol{\theta} = [\theta_1 \quad \cdots \quad \theta_{n_\theta}]^T$. The unknown FIMs ($\boldsymbol{f}$) and the system's parameters ($\boldsymbol{\theta}$) can be identified by maximization of joint PDF of $\boldsymbol{f}$ and $\boldsymbol{\theta}$, given the measured responses. According to the Bayes' rule [28], this a posteriori PDF can be expressed as

$$P(\boldsymbol{\theta}, \boldsymbol{f}|\boldsymbol{y}) = c\; P(\boldsymbol{y}|\boldsymbol{\theta}, \boldsymbol{f})\; P(\boldsymbol{\theta}, \boldsymbol{f}) \tag{3-15}$$

where $P(\boldsymbol{y}|\boldsymbol{\theta}, \boldsymbol{f})$ is the likelihood function, $P(\boldsymbol{\theta}, \boldsymbol{f})$ is the joint *a priori* PDF, and c is a constant. Assuming independences between $\boldsymbol{\theta}$ and $\boldsymbol{f}$ along with uniform PDFs for them (no initial information), maximization of $P(\boldsymbol{\theta}, \boldsymbol{f}|\boldsymbol{y})$ reduces to the maximization of likelihood function $P(\boldsymbol{y}|\boldsymbol{\theta}, \boldsymbol{f})$. This PDF at time instant $k+1$ can be calculated as

$$P(\boldsymbol{y}[1\!:\!k+1]|\boldsymbol{\theta}[k+1], \boldsymbol{f}[1\!:\!k+1]) = \prod_{i=1}^{k+1} P(\boldsymbol{v}[i]) \tag{3-16}$$

which can be rewritten as

$$P(\boldsymbol{y}[1\!:\!k+1]|\boldsymbol{\theta}[k+1], \boldsymbol{f}[1\!:\!k+1]) = \prod_{i=1}^{k+1} \frac{1}{(2\pi)^{l/2}|\mathbf{R}|^{0.5}}\, e^{-\frac{1}{2}\boldsymbol{v}[i]^T\mathbf{R}^{-1}\boldsymbol{v}[i]}. \tag{3-17}$$

To maximize the equation above, it is more convenient to minimize its negative natural logarithm—i.e., the following objective function:

$$J[k+1] = 1.83\,\frac{l(k+1)}{2} + \frac{1}{2}\sum_{i=1}^{k+1}|\mathbf{R}| + \frac{1}{2}\sum_{i=1}^{k+1}\boldsymbol{v}[i]^T\mathbf{R}^{-1}\boldsymbol{v}[i]. \tag{3-18}$$

Two first terms on the right-hand side do not play a role in the objective function, because they are not updated. Thus, the objective function can be simplified as

$$J[k+1] = \sum_{i=1}^{k+1} \boldsymbol{v}[i]^T \mathbf{R}^{-1} \boldsymbol{v}[i]. \tag{3-19}$$

As $\boldsymbol{h}[i]$ is a nonlinear function of $\boldsymbol{\theta}$, it should be linearized through Taylor's expansion so that the objective function becomes a quadratic function of $\boldsymbol{\theta}$ and $\boldsymbol{f}$. To do so, we can approximate $\boldsymbol{h}[i]$ as

$$\boldsymbol{h}[i] \approx \widehat{\boldsymbol{h}}[i] + \mathbf{H}_{\boldsymbol{\theta}}[i]\big(\boldsymbol{\theta}[i] - \widehat{\boldsymbol{\theta}}[i-1]\big) + \mathbf{H}_{\boldsymbol{f}}[i]\big(\boldsymbol{f}[i] - \hat{\boldsymbol{f}}[i-1]\big) \tag{3-20}$$

where

$$\widehat{\boldsymbol{h}}[i] = \boldsymbol{h}\left[\hat{\boldsymbol{z}}[i|i-1], \widehat{\boldsymbol{\theta}}[i-1], \hat{\boldsymbol{f}}[i-1]\right] \tag{3-21}$$

$$\boldsymbol{H}_{\boldsymbol{f}}[i] = \left.\frac{\partial \boldsymbol{h}[i]}{\partial \boldsymbol{f}[i]}\right|_{\boldsymbol{z}[i]=\hat{\boldsymbol{z}}[i|i-1], \boldsymbol{\theta}[i]=\widehat{\boldsymbol{\theta}}[i-1], \boldsymbol{f}[i]=\hat{\boldsymbol{f}}[i-1]} \tag{3-22}$$

and $\mathbf{H}_{\boldsymbol{\theta}}[i] = \bar{\mathbf{H}}_{\boldsymbol{\theta}}[i] + \mathbf{H}_{\boldsymbol{z}}[i]\mathbf{Z}_{\boldsymbol{\theta}}[i]$, in which

$$\bar{\mathbf{H}}_{\boldsymbol{\theta}}[\boldsymbol{i}] = \left.\frac{\partial \boldsymbol{h}[i]}{\partial \boldsymbol{\theta}[i]}\right|_{\boldsymbol{z}[i]=\hat{\boldsymbol{z}}[i|i-1], \boldsymbol{\theta}[i]=\widehat{\boldsymbol{\theta}}[i-1], \boldsymbol{f}[i]=\hat{\boldsymbol{f}}[i-1]} \tag{3-23}$$

$$\mathbf{H}_{\boldsymbol{z}}[i] = \left.\frac{\boldsymbol{\partial h}[i]}{\boldsymbol{\partial z}[i]}\right|_{\boldsymbol{z}[i]=\hat{\boldsymbol{z}}[i|i-1], \boldsymbol{\theta}[i]=\widehat{\boldsymbol{\theta}}[i-1], \boldsymbol{f}[i]=\hat{\boldsymbol{f}}[i-1]} \tag{3-24}$$

$$\mathbf{Z}_{\boldsymbol{\theta}}[i] = \left.\frac{\boldsymbol{\partial z}[i]}{\boldsymbol{\partial \theta}[i]}\right|_{\boldsymbol{\theta}[i]=\widehat{\boldsymbol{\theta}}[i-1]}. \tag{3-25}$$

In the equations above, $\widehat{\boldsymbol{\theta}}[i-1]$ and $\hat{\boldsymbol{f}}[i-1]$ are, respectively, the estimation of $\boldsymbol{\theta}[i]$ and $\boldsymbol{f}[i]$ at the previous step, and $\hat{\boldsymbol{z}}[i|i-1]$ is an *a priori* estimation of state, which can be obtained by using these estimates through the state equation. That is,

$$\hat{\boldsymbol{z}}[i|i-1] = \hat{\boldsymbol{z}}[i-1] + \mathbf{A}_c \Delta t\, \hat{\boldsymbol{z}}[i-1] + \mathbf{B}_c \Delta t\, \hat{\boldsymbol{f}}[i-1] \tag{3-26}$$

where Δt is the sampling time. $\mathbf{Z}_{\boldsymbol{\theta}}[i]$ is the sensitivity matrix of the state vector with respect to the system's parameters, and can be obtained by differentiating both sides of Eq. (3-26) with respect to $\boldsymbol{\theta}$ as in,

$$\mathbf{Z}_{\boldsymbol{\theta}}[i] = \mathbf{Z}_{\boldsymbol{\theta}}[i-1] + \Delta t\left\{\frac{\partial \mathbf{A}_c}{\partial \boldsymbol{\theta}[i]}\hat{\boldsymbol{z}}[i-1] + \mathbf{A}_c\, \mathbf{Z}_{\boldsymbol{\theta}}[i-1] + \frac{\mathbf{B}_c}{\partial \boldsymbol{\theta}[i]}\, \hat{\boldsymbol{f}}[i-1]\right\}. \tag{3-27}$$

By substituting the approximation of $\boldsymbol{h}[i]$ into the objective function, we have

$$J[k+1] = \sum_{i=1}^{k+1} \big(\bar{\boldsymbol{y}}[i] - \mathbf{H}_{\boldsymbol{\theta}}[i]\boldsymbol{\theta}[i] - \mathbf{H}_{\boldsymbol{f}}[i]\boldsymbol{f}[i]\big)^T \mathbf{R}^{-1} \big(\bar{\boldsymbol{y}}[i] - \mathbf{H}_{\boldsymbol{\theta}}[i]\boldsymbol{\theta}[i] - \mathbf{H}_{\boldsymbol{f}}[i]\boldsymbol{f}[i]\big) \tag{3-28}$$

where

$$\bar{\boldsymbol{y}}[i] = \boldsymbol{y}[i] - \hat{\boldsymbol{h}}[i] + \mathbf{H}_{\boldsymbol{\theta}}[i]\hat{\boldsymbol{\theta}}[i-1] + \mathbf{H}_{\boldsymbol{f}}[i]\hat{\boldsymbol{f}}[i-1]. \tag{3-29}$$

Huang et al. [24] showed that the objective function of Eq. (3-28) can be minimized through the following recursive solution

$$\hat{\boldsymbol{f}}[k+1] = \mathbf{S}[k+1]\mathbf{H}_{\boldsymbol{f}}[k+1]^T\mathbf{R}^{-1}(\boldsymbol{I} - \mathbf{H}_{\boldsymbol{\theta}}[k+1]\mathbf{G}_{\boldsymbol{\theta}}[k+1])(\boldsymbol{y}[k+1] - \hat{\boldsymbol{h}}[k+1] + \mathbf{H}_{\boldsymbol{f}}[k+1]\boldsymbol{f}[k]) \tag{3-30}$$

$$\hat{\boldsymbol{\theta}}[k+1] = \hat{\boldsymbol{\theta}}[k] + \mathbf{G}_{\boldsymbol{\theta}}[k+1]\{\boldsymbol{y}[k+1] - \mathbf{H}_{\boldsymbol{f}}[k+1](\hat{\boldsymbol{f}}[k+1] - \boldsymbol{f}[k])\} \tag{3-31}$$

where $\mathbf{G}_{\boldsymbol{\theta}}[k+1]$ is the Kalman Gain Matrix [29] and is calculated as

$$\mathbf{G}_{\boldsymbol{\theta}}[k+1] = \mathbf{P}_{\boldsymbol{\theta}}[k]\mathbf{H}_{\boldsymbol{\theta}}[k+1]^T(\mathbf{R} + \mathbf{H}_{\boldsymbol{\theta}}[k+1]\mathbf{P}_{\boldsymbol{\theta}}[k]\mathbf{H}_{\boldsymbol{\theta}}[k+1]^T)^{-1} \tag{3-32}$$

in which $\mathbf{P}_{\boldsymbol{\theta}}[k]$ is the covariance matrix of the estimation error of $\boldsymbol{\theta}$, and is calculated as

$$\mathbf{P}_{\boldsymbol{\theta}}[k] = (\mathbf{I} + \mathbf{G}_{\boldsymbol{\theta}}[k]\mathbf{H}_{\boldsymbol{f}}[k]\mathbf{S}[k]\mathbf{H}_{\boldsymbol{f}}[k]^T\mathbf{R}^{-1}\mathbf{H}_{\boldsymbol{\theta}}[k])(\mathbf{I} - \mathbf{G}_{\boldsymbol{\theta}}[k]\mathbf{H}_{\boldsymbol{\theta}}[k])\mathbf{P}_{\boldsymbol{\theta}}[k-1]. \tag{3-33}$$

In the equations above, $\mathbf{S}[k+1]$ is also the covariance matrix of the estimation error of $\boldsymbol{f}$ and is obtained as

$$\mathbf{S}[k+1] = \{\mathbf{H}_{\boldsymbol{f}}[k+1]^T\mathbf{R}^{-1}(\mathbf{I} - \mathbf{H}_{\boldsymbol{\theta}}[k+1]\mathbf{G}_{\boldsymbol{\theta}}[k+1])\mathbf{H}_{\boldsymbol{f}}[k+1]^T\}^{-1}. \tag{3-34}$$

Once the system's parameters and the FIMs are updated at each iteration, the state of the system can be updated similarly. That is,

$$\hat{\boldsymbol{z}}[k+1|k+1] = \hat{\boldsymbol{z}}[k+1|k] + \mathbf{G}_{\boldsymbol{z}}[k+1]\{\boldsymbol{y}[k+1] - \hat{\boldsymbol{h}}[k+1]\} \tag{3-35}$$

with the Kalman Gain matrix being

$$\mathbf{G}_{\boldsymbol{z}}[k+1] = \mathbf{P}_{\boldsymbol{z}}[k+1|k]\mathbf{H}_{\boldsymbol{z}}[k+1]^T(\mathbf{R} + \mathbf{H}_{\boldsymbol{z}}[k+1]\,\mathbf{P}_{\boldsymbol{z}}[k+1|k]\,\mathbf{H}_{\boldsymbol{z}}[k+1]^T)^{-1} \tag{3-36}$$

where $\mathbf{P}_{\boldsymbol{z}}[k+1|k]$ is an estimation of state error covariance matrix, obtained from the state equation as

$$\boldsymbol{P}_{\boldsymbol{z}}[k+1|k] = (\mathbf{I} + \mathbf{A}_c\Delta t\,)\mathbf{P}_{\boldsymbol{z}}[k](\mathbf{I} + \mathbf{A}_c\Delta t\,)^T + \mathbf{Q} \tag{3-37}$$

where $\mathbf{P}_{\boldsymbol{z}}[k]$ is the last step's error covariance matrix calculated through

$$\mathbf{P}_{\boldsymbol{z}}[k] = (\mathbf{I} - \mathbf{G}_{\boldsymbol{z}}[k]\,\mathbf{H}_{\boldsymbol{z}}[k+1]\,)\mathbf{P}_{\boldsymbol{z}}[k|k-1]. \tag{3-38}$$

Remark: The proposed method works when the number of measurements is greater than the number of unknown FIMs. While this is almost always satisfied with the bridges under study, we rewrite $\hat{\boldsymbol{f}}[k+1]$ in state and observation equations—as well as other related equations versus acceleration—at the current

time instant, and the displacement, velocity, and acceleration at the previous time step using Newmark's β-method [27], as in

$$\hat{\boldsymbol{f}}[k+1] = \left[\boldsymbol{x}_g[k+1]^T \quad \dot{\boldsymbol{x}}_g[k+1]^T\right]^T = \begin{bmatrix}\mathbf{T}_1\hat{\hat{\boldsymbol{f}}}[k]+\\ \mathbf{T}_2\hat{\hat{\boldsymbol{f}}}[k]+\end{bmatrix} + \begin{bmatrix}\beta\Delta t^2\boldsymbol{I}\\ \gamma\Delta t\boldsymbol{I}\end{bmatrix}\ddot{\boldsymbol{x}}_g[k+1] \tag{3-39}$$

where $\hat{\hat{\boldsymbol{f}}}[k] = \left[x_{g_1}[k], \dot{x}_{g_1}[k], \ddot{x}_{g_1}[k], \cdots, x_{g_{n_g}}[k], \dot{x}_{g_{n_g}}[k], \ddot{x}_{g_{n_g}}[k]\right]$ and

$$\mathbf{T}_1 = \begin{bmatrix}\boldsymbol{\varphi}_1{}^T & & \\ & \ddots & \\ & & \boldsymbol{\varphi}_1{}^T\end{bmatrix}_{n_g\times 3n_g} \tag{3-40}$$

$$\mathbf{T}_2 = \begin{bmatrix}\boldsymbol{\varphi}_2{}^T & & \\ & \ddots & \\ & & \boldsymbol{\varphi}_2{}^T\end{bmatrix}_{n_g\times 3n_g} \tag{3-41}$$

in which $\boldsymbol{\varphi}_1 = [1 \quad \Delta t \quad (0.5-\beta)\Delta t^2]^T$ and $\boldsymbol{\varphi}_2 = [0 \quad 1 \quad (1-\gamma)\Delta t]^T$. Thus, at the $(k+1)^{\text{th}}$ iteration, $\hat{\hat{\boldsymbol{f}}}[k]$ is a known excitation and the unknown FIMs are collected in $\ddot{\boldsymbol{x}}_g[k+1]$. This, then, reduces the number of unknown excitations by a factor of two.

3.3.1 Numerical Verification

To verify the proposed output-only identification method, we simulate the responses of a two-span bridge with continuous deck (Figure 3-2). It is assumed that mass of the foundation-bridge system is concentrated at 13 points, and there is no rotational mass moment of inertia. As such, stiffness and damping matrices can be statically condensed. Two horizontal ground motions recorded at the "Alhambra-1st & Woodward Station (CSMIP24030)" during the 2001 West Hollywood earthquake are applied the remote ends of the soil-foundation springs at the two abutments (left- and right-ends) of the bridge, as shown in Figure 3-2. Also, the abutment motion is multiplied by −1 and applied at the middle pier. These ground motions thus produce a combination of both independent and delayed input motions.

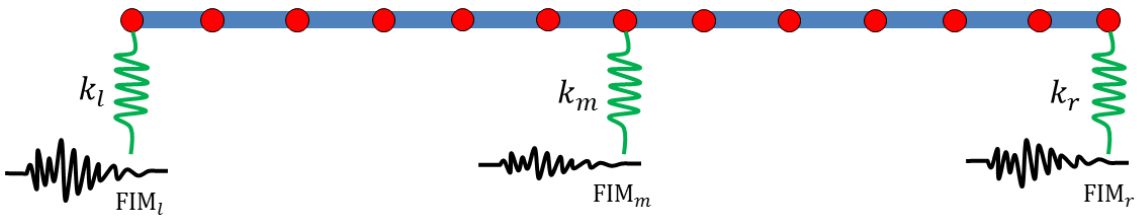

Figure 3-2: Synthetic bridge model with multiple support excitation.

Modulus of elasticity and moment of inertia of the deck beam are set at 1×10^9 and 0.05, respectively. Lumped masses, each with a value of 500, are placed at every 10 units of length. The stiffness of three

springs are 12000, 12000, and 16000, respectively from left to right (all units are consistent). A Rayleigh damping with mass and stiffness factors of 0.2 and 0.002, respectively, is considered to create a classical damping matrix. Natural frequencies and modal damping ratios of this soil-foundation-bridge structure are listed in Table 2-1. As seen, the system is designed such that it is a fair representation of very long and flexible bridges that will be eventually studied in the present project.

Table 3-1: Modal characteristics of the bridge model.

Mode No.	1	2	3	4	5	6	7	8	9	10	11	12	13
$f_n(Hz)$	0.30	0.36	0.65	0.84	1.29	1.97	2.93	4.07	5.40	6.85	8.35	9.69	10.67
$\xi_n(\%)$	5.43	4.59	2.87	2.42	2.04	2.05	2.39	2.95	3.69	4.54	5.43	6.25	6.85

Out of the 13 DOFs, only 5 channels (three foundations, left mid-span, and right mid-span) are used for identification. Stiffnesses of all three springs, modulus of elasticity of the bridge, and the two damping coefficients are assumed as the system's unknown parameters (a total of 6 parameters) along with three FIM acceleration signals. Figure 3-3 displays the convergence rate of the estimation error for all of the 6 parameters (as well as ±1 standard deviation). As seen, all errors converge to zero. Standard deviation around the identified values quantifies how reliable these estimations are. For example, this figure indicates that while the identified damping parameters are very close to their exact values, the uncertainty in these identified values is relatively high compared to the identified spring stiffnesses and the elastic modulus.

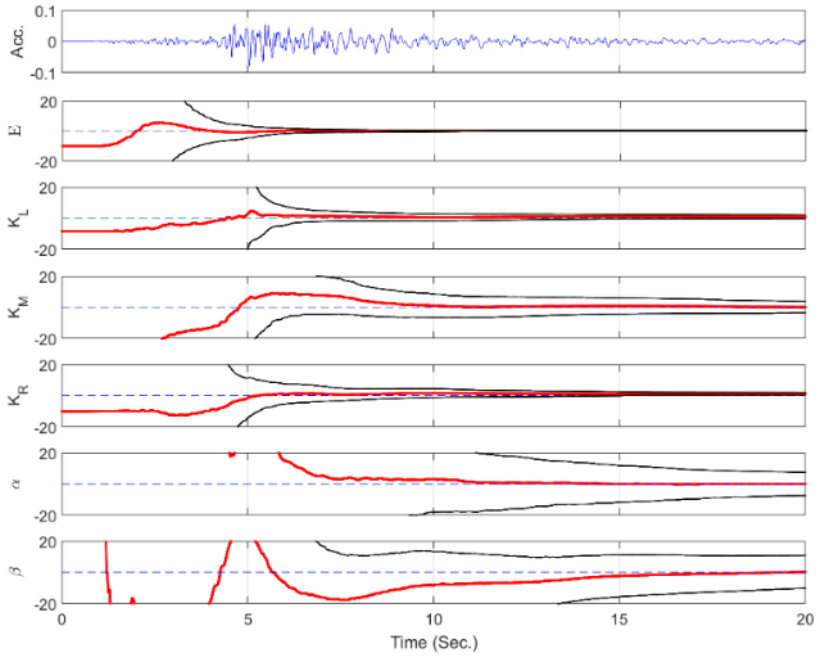

Figure 3-3: Error convergence rate.

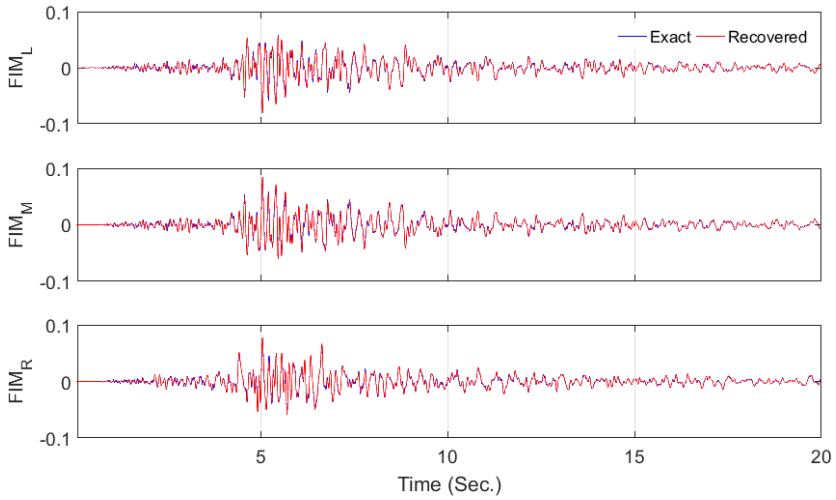

Figure 3-4: Comparison between exact and identified FIMs.

The most important results of the identification process are the recovered FIMs. These signals are plotted together with their exact counterparts in Figure 3-4. As seen, the identified FIMs are very accurate. The standard deviation curves are not shown here, because they were very close to the identified signals. These results indicate that the proposed method is a viable ingredient for the present project, and will produce accurate estimates of FIMs.

CHAPTER 4: SEQUENTIAL OUTPUT-ONLY BAYESIAN IDENTIFICATION

4.1. INTRODUCTION

In the previous chapter, we devised an output-only Bayesian identification. However, the method is only applicable to small scale problems with linear-elastic behavior, while real-life bridge structures under earthquake excitation behave nonlinearly. Herein, we extend the method to a practical solution to be able to solve real problems.

4.2. THE PROPOSED METHOD

4.2.1 Parameter Estimation

The developed joint system and input estimation approach is based on the unscented Kalman filtering method [20], and is briefly described in this section. The response of the Finite Element (FE) model of a bridge structure at each time step to a multi-support earthquake excitation can be expressed as a (nonlinear) function of the model parameter vector, $\boldsymbol{\theta}$, and the time history of the base input motions, $\ddot{\boldsymbol{u}}_{1:i}^{g}$, i.e.,

$$\widehat{\boldsymbol{y}}_i = h_i\left(\boldsymbol{\theta}, \ddot{\boldsymbol{u}}_{1:i}^{g}\right), \tag{4-1}$$

where $h_i(.)$ is the nonlinear response function of the FE model at time step i, encapsulating all the dynamics of the model from time step 1 to i. The measured response vector of the structure, $\boldsymbol{y}_i$, is related to the FE predicted response, $\widehat{\boldsymbol{y}}_i$, as

$$\boldsymbol{v}_i\left(\boldsymbol{\theta}, \ddot{\boldsymbol{u}}_{1:i}^{g}\right) = \boldsymbol{y}_i - \widehat{\boldsymbol{y}}_i\left(\boldsymbol{\theta}, \ddot{\boldsymbol{u}}_{1:i}^{g}\right), \tag{4-2}$$

in which $\boldsymbol{v}_i \in \mathrm{R}^{n_y \times 1}$ is the simulation error vector and accounts for the misfit between the measured and FE predicted response of the structure. The simulation error is ideally modeled as a zero-mean Gaussian white noise vector (i.e., $\boldsymbol{v}_i \sim N(\mathbf{0}, \mathbf{R})$) by neglecting the effects of modeling error [30]. The objective of the estimation problem is to find the estimates of the unknown parameter vector, i.e., $\boldsymbol{\psi}_i = \left[\boldsymbol{\theta}^T, \ddot{\boldsymbol{u}}_{1:i}^{g\ T}\right]^T$, for which the discrepancies between the measured and FE predicted responses are minimized in a probabilistic sense. Since the estimation problem is highly nonlinear, a sequential estimation approach is used in this study to improve estimation efficiency. In this approach, the time domain is divided into successive overlapping time windows, referred to as the estimation windows. The estimation problem is solved at each estimation window to estimate the unknown parameter vector. Assume that the m-th estimation window spans from time step t_1^m to time step t_2^m. Therefore, the unknown parameter vector at this estimation

window is defined as $\boldsymbol{\psi}_m = \left[\boldsymbol{\theta}^T, \ddot{\boldsymbol{u}}_{t_1^m:t_2^m}^{g,m\ T}\right]^T$, where $\boldsymbol{\psi}_m \in \mathrm{R}^{(n_{\boldsymbol{\theta}}+t_l \times n_{\ddot{u}^g})\times 1}$, in which $t_l = t_2^m - t_1^m$ is the estimation window length, and $n_{\ddot{\boldsymbol{u}}^g}$ is the number of unknown components of the base input motions. The unknown parameter vector, $\boldsymbol{\psi}_m$, is estimated using a parameter-only Kalman filtering method. To this end, the unknown parameter vector is modeled as a random vector, the evolution of which is characterized by a Gaussian Markov process – also known as a random walk. Then, a state-space model is set up, in which the state equation governs the evolution of the random parameter vector and the measurement equation corresponds to the discrepancies between the measured and FE predicted structural responses [31], i.e.,

$$\boldsymbol{\psi}_{m,k+1} = \boldsymbol{\psi}_{m,k} + \boldsymbol{\gamma}_{m,k}, \tag{4-3}$$

$$\boldsymbol{y}_{t_1^m:t_2^m} = \hat{\boldsymbol{y}}_{t_1^m:t_2^m,k+1}\left(\boldsymbol{\psi}_{m,k+1}\right) + \boldsymbol{v}_{t_1^m:t_2^m,k+1}, \tag{4-4}$$

in which $\boldsymbol{\gamma}_{m,k} \sim N(\mathbf{0}, \mathbf{Q})$, $\boldsymbol{v}_{t_1^m:t_2^m,k+1} \sim N(\mathbf{0}, \widetilde{\mathbf{R}})$, where $\widetilde{\mathbf{R}} \in \mathrm{R}^{(t_l \times n_y)\times(t_l \times n_y)}$ is a block diagonal matrix, whose block diagonals are the simulation error covariance matrix $\mathbf{R}$. In Eqs. (4-3) and (4-4), k denotes the iteration number. As can be observed, the estimation process at each estimation window is iterative, i.e., the mean vector and covariance matrix of the unknown parameter vector is iteratively updated based on the discrepancies between the time histories of the measured and estimated responses.

An Unscented Kalman Filtering (UKF) method is used to update the unknown parameter vector at each iteration. In this method, the nonlinear FE model is evaluated separately at a set of deterministically selected realizations of the unknown parameter vector, which are referred to as the sigma points (SPs) denoted by $\boldsymbol{\vartheta}^j$. The sigma points are selected around the prior mean estimate $\hat{\boldsymbol{\psi}}^-$. In this study, a scaled Unscented Transformation (UT) based on $2n_{\boldsymbol{\psi}} + 1$ sigma points (i.e., $j = 1,2,\ldots,2n_{\boldsymbol{\psi}} + 1$) is used, where $n_{\boldsymbol{\psi}}$ denotes the size of the extended parameter vector. The mean and covariance matrix of the FE predicted structural responses, and the cross-covariance matrix of $\boldsymbol{\psi}$ and $\boldsymbol{y}$ are respectively computed using a weighted sampling method as

$$\bar{\boldsymbol{y}} = \sum_{j=1}^{2n_{\boldsymbol{\psi}}+1} W_m^j\, \hat{\boldsymbol{y}}_i\left(\boldsymbol{\vartheta}^j\right), \tag{4-5}$$

$$\hat{\mathbf{P}}_{\boldsymbol{yy}} = \sum_{j=1}^{2n_{\boldsymbol{\psi}}+1} W_e^j \left[\hat{\boldsymbol{y}}_i\left(\boldsymbol{\vartheta}^j\right) - \bar{\boldsymbol{y}}\right]\left[\hat{\boldsymbol{y}}_i\left(\boldsymbol{\vartheta}^j\right) - \bar{\boldsymbol{y}}\right]^T + \mathbf{R}, \tag{4-6}$$

$$\hat{\mathbf{P}}_{\boldsymbol{\psi y}} = \sum_{j=1}^{2n_{\boldsymbol{\psi}}+1} W_e^j \left[\boldsymbol{\vartheta}^j - \hat{\boldsymbol{\psi}}^-\right]\left[\hat{\boldsymbol{y}}_i\left(\boldsymbol{\vartheta}^j\right) - \bar{\boldsymbol{y}}\right]^T, \tag{4-7}$$

where W_m^j and W_e^j denote weighting coefficients [26]. Now, the UKF prediction-correction procedure can be employed to estimate the posterior parameter mean vector $\hat{\boldsymbol{\psi}}^+_{m,k+1}$ and covariance matrix $\hat{\mathbf{P}}^+_{\boldsymbol{\psi},m,k+1}$ at each iteration. The identification algorithm is summarized in Table 4-1.

Table 4-1: Identification algorithm for joint estimation of the model parameters and the FIM time history.

1. Set the estimation window length t_l, and the start and end points of each estimation window.
2. Set the initial mean vector and covariance matrix of the unknown parameter vector as $\widehat{\boldsymbol{\psi}}^{+}{}_{0} = \left[\widehat{\boldsymbol{\theta}}_0{}^{T}, \ddot{\boldsymbol{u}}_{t_1^0:t_2^0}^{g,0}{}^{T}\right]^{T}$, and $\mathbf{P}_{\boldsymbol{\psi},0}^{+} = \begin{bmatrix} \widehat{\mathbf{P}}_{\boldsymbol{\theta\theta},0} & \mathbf{0} \\ \mathbf{0} & \widehat{\mathbf{P}}_{\ddot{\boldsymbol{u}}^{g,0}} \end{bmatrix}$.
3. Define the process noise covariance matrix $\mathbf{Q}$ and the simulation error covariance matrix $\mathbf{R}$. Set up matrix $\widetilde{\mathbf{R}}$.
4. For the m-th estimation window:
   4.1. Retrieve the posterior estimates of the mean vector and covariance matrix of the unknown parameter vector from the last estimation window (i.e., $\widehat{\boldsymbol{\psi}}^{+}{}_{m-1}$, and $\mathbf{P}_{\boldsymbol{\psi},m-1}^{+}$). Set up $\widehat{\boldsymbol{\psi}}^{+}{}_{m,0}$ and $\mathbf{P}_{\boldsymbol{\psi},m,0}^{+}$ based on $\hat{\boldsymbol{\psi}}_{\boldsymbol{m}-1}^{+}$ and $\mathbf{P}_{\boldsymbol{\psi},m-1}^{+}$.
   4.2. Iterate (k = 1, 2, …):
      a. Set $\widehat{\boldsymbol{\psi}}^{-}{}_{m,\mathrm{k}+1} = \widehat{\boldsymbol{\psi}}^{+}{}_{m,\mathrm{k}}$, $\mathbf{P}_{\boldsymbol{\psi},m,k+1}^{-} = \mathbf{P}_{\boldsymbol{\psi},m,k}^{+} + \mathbf{Q}$.
      b. Generate sigma points. Run the FE model for $(2n_{\boldsymbol{\psi}} + 1)$ sigma points. Derive $\overline{\boldsymbol{y}}$, $\widehat{\mathbf{P}}_{\boldsymbol{yy}}$, and $\widehat{\mathbf{P}}_{\boldsymbol{\psi y}}$ using Eqs. (4-5)-(4-7).
      c. Compute the Kalman gain matrix: $\mathbf{K} = \widehat{\mathbf{P}}_{\boldsymbol{\psi y}}\left(\widehat{\mathbf{P}}_{\boldsymbol{yy}}\right)^{-1}$.
      d. Find the corrected estimates of the mean vector and covariance matrix of the unknown parameter vector:
      $\widehat{\boldsymbol{\psi}}^{+}{}_{m,\mathrm{k}+1} = \widehat{\boldsymbol{\psi}}^{-}{}_{m,\mathrm{k}+1} + \mathbf{K}\left(\boldsymbol{y}_{t_1^m:t_2^m} - \overline{\boldsymbol{y}}\right)$, $\mathbf{P}_{\boldsymbol{\psi},m,k+1}^{+} = \mathbf{P}_{\boldsymbol{\psi},m,k+1}^{-} - \mathbf{K}\left(\widehat{\mathbf{P}}_{\boldsymbol{yy}} + \widetilde{\mathbf{R}}\right)\mathbf{K}^{T}$.
      e. Check for convergence: if $\left|\widehat{\boldsymbol{\psi}}^{+}{}_{m,k+1} - \widehat{\boldsymbol{\psi}}^{+}{}_{m,k}\right| < 0.02 \times \widehat{\boldsymbol{\psi}}^{+}{}_{m,k-1}$ or $k + 1 > 10$, then move to the next estimation window ($m = m + 1$, go to step 4); otherwise, iterate again at the current estimation window ($k = k + 1$, go to step 4.2).

4.2.2 Constraint Correction

Model-based identification method provides an option to devise feasibility constraints for updating parameters based on their physical meaning. For this purpose, the posterior multi-dimensional joint Gaussian probability distribution function (GPDF) of the parameter vector ($\boldsymbol{\theta}$) must be truncated at each time step based on the feasibility limits as follows [32].

Suppose that there are n_c linear constraints for the parameter vector $\boldsymbol{\theta}$ as follows

$$l_i \le \boldsymbol{\varphi}_i^{T}\boldsymbol{\theta} \le u_i, \quad i = 1 \ldots n_c, \tag{4-8}$$

where $\boldsymbol{\varphi}_i$ is a $n_c \times 1$ vector containing the coefficients of linear constraints, and l_i and u_i are the lower and upper bounds, respectively. We transform the parameter vector to a new random vector $\boldsymbol{\eta} \sim N(\mathbf{0}, \mathbf{I}_{n_\theta \times n_\theta})$ as

$$\boldsymbol{\eta} = \boldsymbol{\phi}\mathbf{W}^{-\frac{1}{2}}\mathbf{T}^{T}\left(\boldsymbol{\theta} - \widehat{\boldsymbol{\theta}}_k^{+}\right), \tag{4-9}$$

where $\mathbf{W}$ is the diagonal eigenvalue matrix and $\mathbf{T}$ is the eigenvector matrix of $\widehat{\mathbf{P}}_{\boldsymbol{\theta\theta},k}^{+}$. The $n_\theta \times n_\theta$ matrix $\boldsymbol{\phi}$ is an orthogonal matrix obtained using the Gram-Schmidt orthogonalization process in order to satisfy the following relationship

$$\boldsymbol{\phi}\mathbf{W}^{\frac{1}{2}}\mathbf{T}^T\boldsymbol{\varphi}_i = \left[\left(\boldsymbol{\varphi}_i^T\widehat{\mathbf{P}}_{\boldsymbol{\theta\theta},k}^{+}\boldsymbol{\varphi}_i\right)^{1/2} \quad 0 \quad 0\right]^T. \tag{4-10}$$

By replacing $\boldsymbol{\theta}$ with its transformed version in Eq. (4-8), we have

$$l_i \le \boldsymbol{\varphi}_i^T(\mathbf{T}\mathbf{W}^{\frac{1}{2}}\boldsymbol{\phi}^T\boldsymbol{\eta} + \widehat{\boldsymbol{\theta}}_k^{+}) \le u_i,\ i = 1 \dots n_c, \tag{4-11}$$

which can be rewritten as

$$\frac{l_i - \boldsymbol{\varphi}_i^T\widehat{\boldsymbol{\theta}}_k^{+}}{\left(\boldsymbol{\varphi}_i^T\widehat{\mathbf{P}}_{\boldsymbol{\theta\theta},k}^{+}\boldsymbol{\varphi}_i\right)^{1/2}} \le \frac{\boldsymbol{\varphi}_i^T\mathbf{T}\mathbf{W}^{\frac{1}{2}}\boldsymbol{\phi}^T}{\left(\boldsymbol{\varphi}_i^T\widehat{\mathbf{P}}_{\boldsymbol{\theta\theta},k}^{+}\boldsymbol{\varphi}_i\right)^{1/2}}\boldsymbol{\eta} \le \frac{u_i - \boldsymbol{\varphi}_i^T\widehat{\boldsymbol{\theta}}_k^{+}}{\left(\boldsymbol{\varphi}_i^T\widehat{\mathbf{P}}_{\boldsymbol{\theta\theta},k}^{+}\boldsymbol{\varphi}_i\right)^{1/2}},\ i = 1 \dots n_c, \tag{4-12}$$

which can be simplified according to Eq. (4-10) as

$$\frac{l_i - \boldsymbol{\varphi}_i^T\widehat{\boldsymbol{\theta}}_k^{+}}{\left(\boldsymbol{\varphi}_i^T\widehat{\mathbf{P}}_{\boldsymbol{\theta\theta},k}^{+}\boldsymbol{\varphi}_i\right)^{1/2}} \le [1 \quad 0 \quad 0]\boldsymbol{\eta} \le \frac{u_i - \boldsymbol{\varphi}_i^T\widehat{\boldsymbol{\theta}}_k^{+}}{\left(\boldsymbol{\varphi}_i^T\widehat{\mathbf{P}}_{\boldsymbol{\theta\theta},k}^{+}\boldsymbol{\varphi}_i\right)^{1/2}},\ i = 1 \dots n_c. \tag{4-13}$$

This means that the i-th constraint is only applied to the first element of $\boldsymbol{\eta}$ as

$$\frac{l_i - \boldsymbol{\varphi}_i^T\widehat{\boldsymbol{\theta}}_k^{+}}{\left(\boldsymbol{\varphi}_i^T\widehat{\mathbf{P}}_{\boldsymbol{\theta\theta},k}^{+}\boldsymbol{\varphi}_i\right)^{1/2}} \le \eta_1 \le \frac{u_i - \boldsymbol{\varphi}_i^T\widehat{\boldsymbol{\theta}}_k^{+}}{\left(\boldsymbol{\varphi}_i^T\widehat{\mathbf{P}}_{\boldsymbol{\theta\theta},k}^{+}\boldsymbol{\varphi}_i\right)^{1/2}} \tag{4-14}$$

By calculating the mean ($\bar{\eta}_1$) and variance (σ_1^2) of η_1 after the constraint application, the constrained parameter mean and covariance matrix can be derived as follows

$$\widehat{\boldsymbol{\theta}}_c^{+} = \mathbf{T}\mathbf{W}^{\frac{1}{2}}\boldsymbol{\phi}^T\boldsymbol{\mu}_c + \widehat{\boldsymbol{\theta}}_k^{+} \tag{4-15}$$

$$\widehat{\mathbf{P}}_{\boldsymbol{\theta\theta},c}^{+} = E\left[(\boldsymbol{\theta} - \widehat{\boldsymbol{\theta}}_c^{+})(\boldsymbol{\theta} - \widehat{\boldsymbol{\theta}}_c^{+})^T\right] = \mathbf{T}\mathbf{W}^{\frac{1}{2}}\boldsymbol{\phi}^T\boldsymbol{\Sigma}_c\boldsymbol{\phi}\mathbf{W}^{-\frac{1}{2}}\mathbf{T}^T, \tag{4-16}$$

where

$$\boldsymbol{\mu}_c = [\bar{\eta}_1 \quad 0 \quad 0]^T \tag{4-17}$$

$$\boldsymbol{\Sigma}_c = \begin{bmatrix} \sigma_1^2 & 0 & \cdots & 0 \\ 0 & 1 & \ddots & \vdots \\ \vdots & \ddots & \ddots & 0 \\ 0 & \cdots & 0 & 1 \end{bmatrix}. \tag{4-18}$$

By replacing $\widehat{\boldsymbol{\theta}}_k^{+} = \widehat{\boldsymbol{\theta}}_c^{+}$ and $\widehat{\mathbf{P}}_{\boldsymbol{\theta\theta},k}^{+} = \widehat{\mathbf{P}}_{\boldsymbol{\theta\theta},c}^{+}$, we repeat the constraint correction process for all n_c constraints one at a time.

4.2.3 Identifiability

Successful identification of the FE model parameters depends on the information that the measurement data contain about those model parameters. It also depends on the sensitivity of the FE model responses with respect to the estimation parameters. To quantify the information content of the measurement data and, therefore, to assess the identifiability of parameters, we hereby follow an approach similar to one presented in [33]. Entropy gain, or the gain in the information about a model parameter θ_i from measurement data, is expressed as the difference between the a priori and the a posteriori information entropy, which can be calculated as

$$\Delta H(\theta_i) = \frac{1}{2} ln([\mathbf{I}]_{ii} P_i + 1), \tag{4-19}$$

where P_i is the a priori variance of θ_i and $[\mathbf{I}]_{ii}$ is the i-th diagonal element of the Fisher Information Matrix defined as

$$\mathbf{I} = \sum_{k=1}^{n} \frac{\partial \hat{\mathbf{y}}_k}{\partial \boldsymbol{\theta}}^T \Big|_{\boldsymbol{\theta}=\hat{\boldsymbol{\theta}}} \tilde{\mathbf{R}}^{-1} \frac{\partial \hat{\mathbf{y}}_k}{\partial \boldsymbol{\theta}} \Big|_{\boldsymbol{\theta}=\hat{\boldsymbol{\theta}}} \tag{4-20}$$

where n is the number of time samples. To calculate the sensitivity terms (i.e., $\partial \hat{\mathbf{y}}_k / \partial \boldsymbol{\theta}$), we employ a Finite Difference Method (FDM). The entropy gain (ΔH) of different parameters should be compared to find out which parameters receive more information from the measurement data—i.e., which parameters are more likely to be identified. A parameter with higher entropy gain is relatively more likely to be identifiable, unless it has a strong dependency on another parameter. The mutual dependency can be quantified through a mutual gain metric that is defined as

$$\Delta M(\theta_i, \theta_j) = \frac{1}{2} ln \left[\frac{([\mathbf{I}]_{ii} {P_i}^{-1} + 1)([\mathbf{I}]_{jj} {P_j}^{-1} + 1)}{|\tilde{\mathbf{I}} + \mathbf{P}_{ij}{}^{-1}|} \right], \text{ with } \tilde{\mathbf{I}} = \begin{bmatrix} [\mathbf{I}]_{ii} & [\mathbf{I}]_{ij} \\ [\mathbf{I}]_{ji} & [\mathbf{I}]_{jj} \end{bmatrix} \tag{4-21}$$

where $\mathbf{P}_{ij}$ is the a priori covariance matrix of θ_i and θ_j. In case of strong dependency between two parameters, one parameter should be put aside (i.e., fixed), to ensure the identifiability of the other one.

CHAPTER 5: A PILOT STUDY ON THE GOLDEN GATE BRIDGE

5.1. INTRODUCTION

This chapter presents results of an extensive verification and validation of the proposed method for a large-scale bridge, the Golden Gate bridge, with only geometrical nonlinearity.

5.2. THE STRUCTURAL SYSTEM

The Golden Gate (Figure 5-1) is a strait that connects the San Francisco Bay to the Pacific Ocean. The Golden Gate Bridge (GGB) is a suspension bridge over Golden Gate, which connects the city of San Francisco to the Marin County. GGB was the longest (main span) suspension bridge in the world until 1964. It has been also declared as one of the wonders of the modern world by the American Society of Civil Engineers (ASCE).

Figure 5-1: The Golden Gate Bridge.

The GGB was completed and opened to traffic on May 28, 1937 [34]. The total length of the GGB from abutment to abutment is 2737 m (8981 ft), and other detailed dimensions of the bridge are shown in Figure 5-2. Summarizing from [35], the structural system of GGB is briefly reviewed next (the geometrical and mechanical properties of structural elements can be found, for example, in [36], [37] and are omitted here for brevity). As a suspension bridge, the GGB consists of several structural systems (Figure 5-3). The approach viaducts are of steel girder, truss and arch construction. Anchorage blocks (south one is not shown in Figure 5-3), piers, and pylons are of reinforced concrete construction. The towers, deck, and cables (main cable and hangers) are of steel construction. The towers are founded directly on the underlying rock. The deck—which was originally reinforced concrete and was replaced in the 1980s by orthotropic steel plates at the center and with reinforced concrete sidewalks—is carried on floor beams every 25 ft. These beams are connected to stiffening trusses at both sides. In the original construction, stiffening trusses were connected to each other with only a top lateral bracing system. Later, in the 1950s, a bottom lateral bracing system was added to make the roadway supporting system a closed box in order to reduce the deck's twist. This stiffening system, which is suspended at every 50 ft with hangers on each side—was replaced in the 1970s. The main span is fixed laterally and vertically to the towers at its both ends and has a limited amount of free movement in the longitudinal direction. It is fully released for rotation at its both ends through joints.

While the GGB experienced several partial retrofits as mentioned above, the GGB Highway and Transportation District[6] initiated a series of studies of the bridge— prompted by the 1989 Loma Prieta earthquake—, which concluded that a massive retrofit was necessary, including [38]:

- Installation of dampers between the stiffening trusses and the towers,
- Replacement of one-quarter of the stiffening truss lateral braces with new ductile members,
- Stiffening of the bridge towers to prevent undesirable plate buckling,
- Strengthening of the bridge piers,
- Strengthening of the saddles supporting cables on the tops of the towers,
- Strengthening of the wind-locks connecting the suspended structure and the towers, and
- Strengthening of the pedestals supporting the orthotropic deck.

The retrofit started in 1997 and was initially planned to be completed in 2012, which was later changed several times (lately to 2021). The retrofit is being carried out in three phases due to several factors such as level of vulnerability, provided funds, and traffic closure. In Phase 1 (1997-2002), the Marin (North) approach viaduct was retrofitted. In Phase 2 (2002-2007), San Francisco (South) approach viaduct, anchorage housing, arch, and pylons were retrofitted. Phase 3 (2008-2021) is being conducted in two sub-phases A and B. In Phase 3A (2008-2014), the North Anchorage housing and pylon were retrofitted. In Phase 3B, the main suspension span, main towers, and the south tower pier and the fender are going to be retrofitted. This phase is the most challenging part and mainly due to this reason the completion date of the

[6] This is a special district of the state of California formed in 1928.

retrofit project has been extended to 2021. As a summary, details of the retrofit measures conducted at each phase are shown in Figure 5-4.

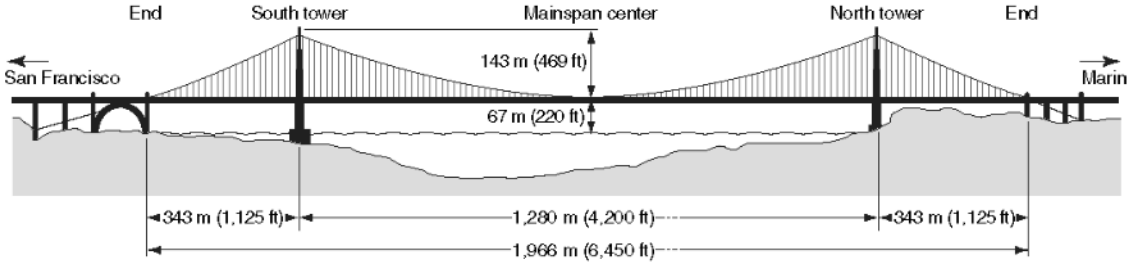

Figure 5-2: Dimensions of the bridge [39].

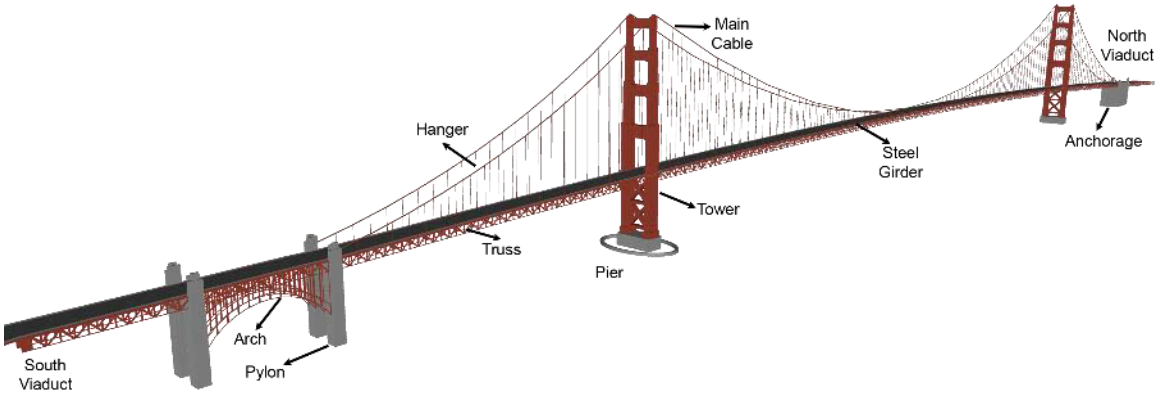

Figure 5-3: Various parts of the GGB (3D model is taken from Google Earth).

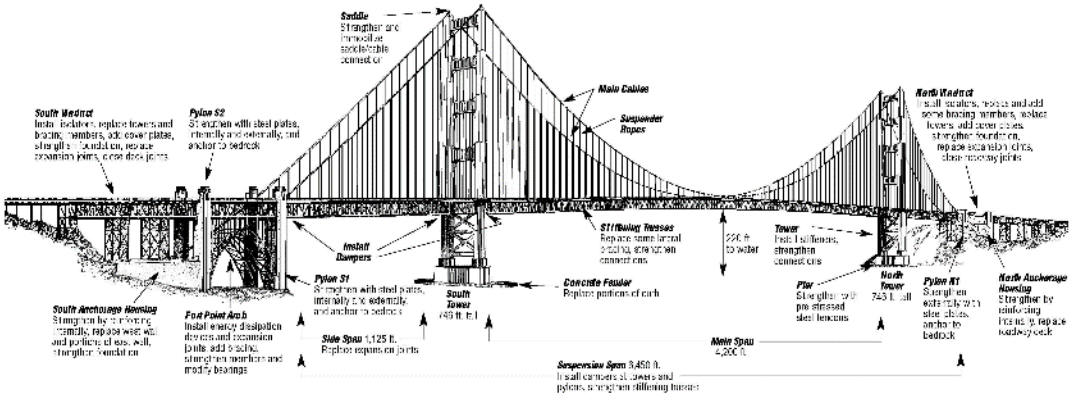

Figure 5-4: GGB retrofit measures (http://goldengatebridge.org/projects/retrofit.php).

5.3. PRIOR IDENTIFICATION STUDIES

The oldest study on vibration-based identification of the GGB goes back to 1947 when Nishkian measured the vertical movement of the bridge deck under operational conditions [40]. Later, Vincent carried out similar measurements using more accurate sensors and compared real-life data and model predictions [41], [42]. He used data recorded during a 15-year period by suspended mass accelerometers and identified the first asymmetric, and the first and second symmetric vertical natural frequencies of the deck as 0.095, 0.125, and 0.158 Hz, respectively. He also reported the torsional frequency of deck as 0.20 Hz. The rate of studies (not specifically on the system identification topic) on this bridge accelerated in the 90s. Tanaka and Davenport [43] re-examined the data used by Vincent [41]. They also experimentally tested a taut-strip model in the laboratory under wind turbulence and concluded that at low-speed winds first, the asymmetric mode is the dominant one. Abdel-Ghaffar and Scanlan [36], [37] conducted extensive experimental investigations on the bridge to determine natural frequencies, mode shapes, and damping ratios from ambient data. They used spectral peak-picking for natural frequency identification, cross-spectrum analysis for mode shape identification, and half-power bandwidth method for damping ratio estimation. They could identify 20 vertical, 18 torsional, 33 lateral, and 20 longitudinal modes of the suspended span in the frequency range of 0 to 1.5 Hz, and 20 longitudinal, 15 torsional, and 11 lateral modes of the towers in the frequency range of 0 to 5 Hz.

Pakzad et al. [44] designed and implemented a scalable wireless sensor network and used it for modal identification of the GGB from ambient data collected during the summer of 2006. They limited their analyses to modes below 5 Hz. As they used a wireless sensor network, they could measure the vibrations using various instrumentation layouts. Through their study, it was clearly understood that for such a large and flexible structure, identification results may suffer from spatial aliasing[7] if the number of measurement nodes is small. Based on their results, frequencies of the first vertical, transverse and torsional modes are 0.106, 0.228, and 0.230 Hz, respectively, and all these modes are asymmetric [45].

The same dataset was later used several times for verification and validation of some identification methods and frameworks. For example, Pakzad et al. [46] verified the performance of a "distributed modal identification" approach through the same dataset. Also, Chang and Pakzad [47] verified their modified Natural Excitation Technique (NExT) using the same data. Also in 2014, same data was analyzed by Matarazzo and Pakzad [48] through pseudo mobile sensing data[8] and they used structural identification using expectation maximization (STRIDE) [49] to identify modal properties of the GGB from ambient data. Their results were as accurate as those identified before [45].

In 2012, Çelebi [39] carried out an extensive study on the GGB. He analyzed data recorded during three weak earthquakes (Bolinas 1999, Yountville 2000, and Alum Rock 2007). He employed spectral analysis [50] for output-only, and Auto-Regressive with eXogenous input (ARX) [51] for input-output

[7] This is a conclusion provided by this paper's authors based on the results presented in [44].

[8] Actually, pseudo-mobile sensing data were used/simulated in this study without actually implementing a mobile sensor network. These data were extracted directly from a fixed sensor data matrix.

identification purposes. Çelebi's study is the first one in which modal characteristics are identified from earthquake data. He filtered out frequencies below 0.05 and above 50 Hz. While this study provides us with valuable information, it suffers from various deficiencies. Namely, (*i*) peak-picking from amplitude spectra is generally not a reliable method for modal identification from earthquake data as there is no direct/objective way to determine those peaks that represent the structure only, and (*ii*) the input-output ARX technique cannot consider multiple support excitations. Even under a uniform excitation assumption, any input-output identification technique would yield modal characteristics between the input and output locations only—thereby excluding potential flexibilities provided by the boundaries.

5.4. RECORDED EARTHQUAKE DATA

Following the 1989 Loma Prieta earthquake, A recommendation was issued for instrumenting large bridges in the California [52]. Detailed seismic instrumentation plans were developed in 1992 through CSMIP by the GGB Highway and Transportation District in cooperation with an appointed seismic instrumentation advisory board [53]. In 1995 (prior to retrofit), 72 accelerometers (15 on the north viaduct and anchorage housing; 33 on the suspension bridge; 22 on the south viaduct and anchorage housing and Fort Arch; 3 at the south free-field; 3 at a downhole under the south viaduct) and 4 relative displacement sensors were installed [54]. After the completion of Phase 1 of the retrofit, 18 sensors additional were installed on the north viaduct and anchorage housing and a geotechnical array with 6 sensors was installed near the north viaduct. Finally, 22 more sensors were added after the completion of Phase 2. The current locations[9] of the sensors on the suspension bridge are shown in Figure 5-5.

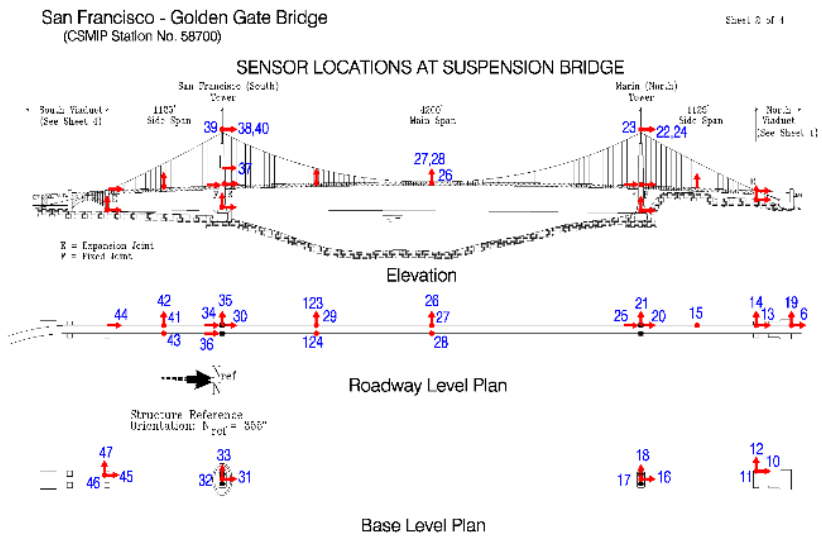

Figure 5-5: Locations of strong-motion sensors on the suspension span of the Golden Gate Bridge (www.strongmotioncenter.org, last accessed 1/1/2017).

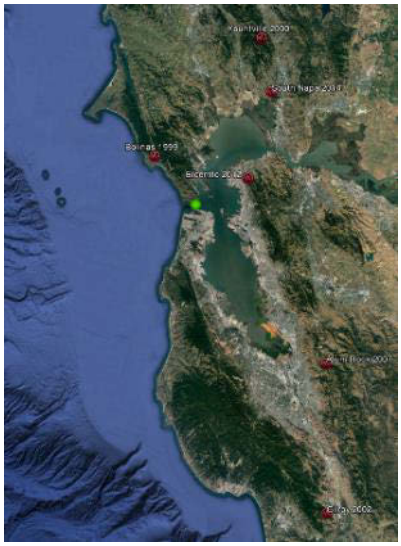

Figure 5-6: Geographical distribution of earthquake centers around the Golden Gate Bridge.

[9] Last update: 10/31/2016

Six earthquakes have been recorded by the GGB instrumentation system to date. Table 5-1 and Figure 5-6 provides various attributes and geographical distributions of these earthquakes around the GGB. As described above, earthquake data up to 2007 were already studied by Çelebi [39], and results from that study will be briefly examined below. Here, we only study the latest earthquake, i.e., 2014 South Napa earthquake, which, incidentally, caused the largest Peak Structural Acceleration (PSA), as it can be seen in Table 5-1.

Table 5-1: Earthquakes recorded by GGB instrumentation system (Last update: 1/1/2017)

Earthquake	Date/Time UTC	Magnitude	Depth (km)	Epicentral Dist. (km)	PGA (g)	PSA (g)
Bolinas	8-17-1999/1:06	4.5 (Mw)	7.0	20.6	0.020	0.112
Yountville	9-3-2000/8:36	5.0 (Mw)	5.0	62.1	0.009	0.039
Gilroy	5-13-2002/05:00	4.9 (Mw)	7.6	122.5	0.010	0.071
Alum Rock	10-30-2007/03:04	5.4 (Mw)	9.2	75.5	0.012	0.036
Elcerrito[#]	3/5/2012/13:33	4.0 (ML)	9.2	19.6	0.016	0.084
South Napa	8-24-2014/10:30	6.0 (Mw)	11.3	46.7	0.012	0.181

[#] Data from this event are not available at CESMD.

Due to very sparse instrumentation (Figure 5-5), it is crucial to limit the frequency band to prevent the "spatial aliasing" phenomenon. As it was described in the previous section, due to the size and flexibility of the system, there are many modes within the original frequency range of data (0-50 Hz). So, using such sparse instrumentation it will not be possible to distinguish modes. As an example, the first 8 mode shapes of the suspension part, which are identified from ambient signals through dense instrumentation by Abdel-Ghaffar [36] are redrawn in Figure 5-7. On this figure, the available sensors deployed through CSMIP, which were able to measure the bridge responses during the 2014 South Napa earthquake are shown by red circles. In the best-case scenario, we can only identify mode shapes displayed by the red solid lines. As can be seen from this figure, there is no meaningful difference between the first symmetric and the fourth asymmetric modes shapes as measured by the available sensors, for example. Or, AS3 and S4 mode shapes are very similar to each other. Note that these modes are all low-frequency modes and the similarity of mode shapes will increase for higher modes.

The proposed output-only identification method is computationally expensive. To reduce the computational cost, we apply a low-pass filter to only keep a few fundamental modes. As studied by Pakzad and Fenves [45], there are, for example, 15 vertical modes below 1 Hz, so we filter out frequencies higher than this value. Also, due to low-frequency errors observed in the signals, frequencies below 0.05 Hz are also filtered out through the high-pass filter. Recorded acceleration signals on the suspension part are shown in Figure 5-8 in which all of the records are shown with the same scale. Also, the first 20 seconds of the signals are not shown, because there is no significant motion during that period of time. As this figure shows, responses of the deck in the vertical direction and the longitudinal and transverse vibrations of the towers have the highest level of motion.

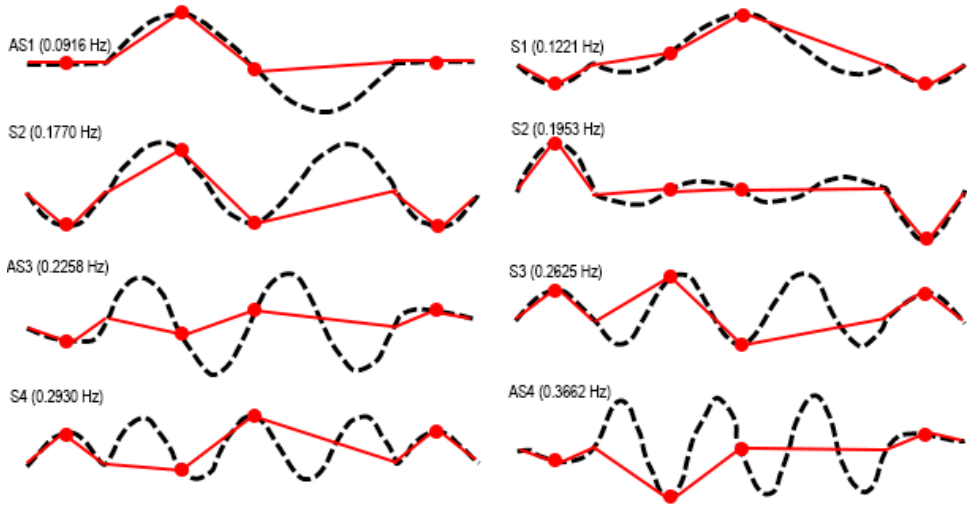

Figure 5-7: Mode shapes identified from ambient testing [36] (black curves), permanent sensors (red circles), and identifiable mode shapes (red lines).

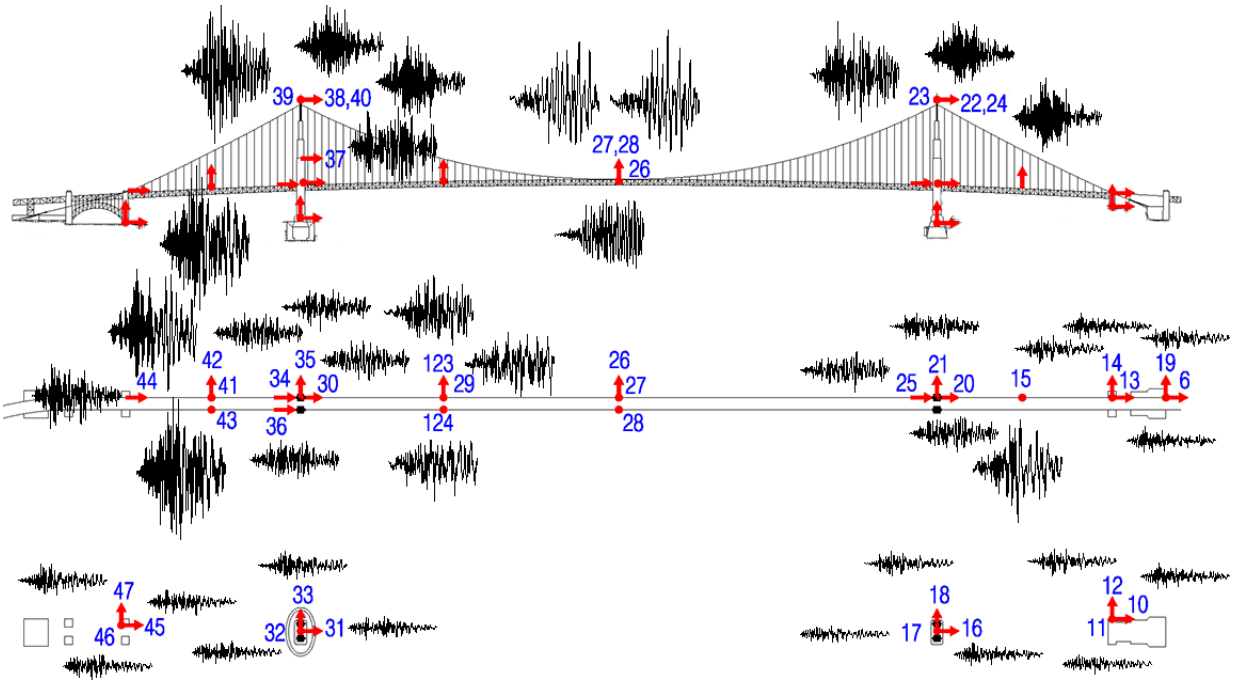

Figure 5-8: Recorded acceleration signals on the suspension part of the GGB.

To make sure that the frequency range under study contains most of the energy content of the signals, the maximum displacement responses after filtering are normalized with the original values and are shown in Figure 5-9. As it can be seen, this ratio is higher than 0.8 for most of the channels. Specifically, for those

channels recorded on the suspension part (foundation, deck, and tower levels), this value is close to 0.9. Note that those few cases with values < 0.8 are related to low-frequency errors which are removed through high-pass filtering.

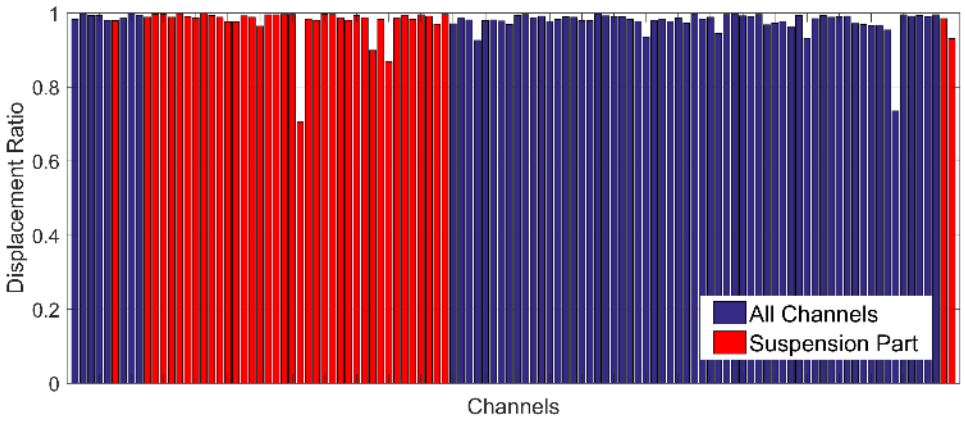

Figure 5-9: Ratio of after filtering maximum displacement values to the original values.

As will be discussed later, the material nonlinearity will not be included in the model. Here, we carried out a visual observation on the time variations of dominant frequencies to make sure that there is no significant nonlinearity in the system. To do so, we present here the time-frequency representation [55] of a few signals. As a first example, the time-frequency representation of CH27+CH28 (vertical movement of the mid-span) is presented in subplot (b) of Figure 5-10(left). Acceleration time-history of the signal is also shown in subplot (a). As can be seen, a very dominant frequency at 0.3067 Hz with a minor contribution from 0.6733 Hz is observed in this figure. High level of energy of the 0.3067 Hz component may mask the contribution of other components. To resolve this issue, the time-history is scaled by its instantaneous amplitude as described in [56]. This figure is shown in subplot (c) of Figure 5-10 (left). Interestingly, two other frequencies appear now. During the first ~20 seconds, the bridge is vibrating in its fundamental mode ~0.1333 Hz due to ambient excitations. After the arrival of the seismic waves, higher modes at 0.3067, 0.6733, and 0.8867 Hz become excited, whereas mode at 0.3067 Hz persistently exists until the end of the record.

Figure 5-10 (right) displays similar graphs for the deck's torsional vibrations, estimated through CH27-CH28. Again, through the time-frequency representation and with the help of amplitude scaling, it is possible to observe the contributions of different modes at different time instants. At the very beginning, a mode at 0.3333 Hz is dominant, then a mode at 0.2333 Hz appears for 20 seconds until the arrival of severe seismic waves. After a short period of time in which a higher frequency of 0.8133 Hz is present, most part of the signal is affected by a mode at 0.5733 Hz.

Frequencies named at the two paragraphs above can be labeled according to prior studies and their proximity to each other. These labels are shown in Table 5-2 and are deduced from Abdel-Ghaffar's experimental study [36].

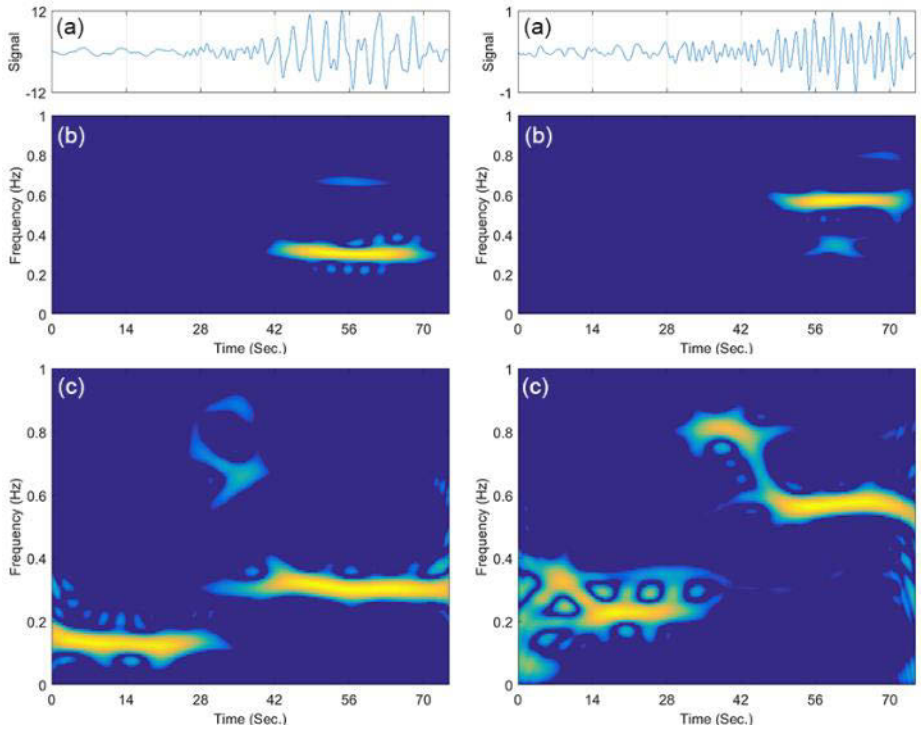

Figure 5-10: Time and time-frequency representation of CH27+CH28 (left) and CH27-CH28 (right).

Table 5-2: Labels of the modes observed in Figure 5-7 [36].

Frequency (Hz)	0.1333	0.2333	0.3067	0.3333	0.6733	0.5733	0.8133	0.8867
Mode	VS1	TS1	VS4	TS2	VS7	TS4	TS6	VS9

V: Vertical; T: Torsional; S: Symmetric.

5.5. NUMERICAL MODELING

To the best knowledge of the authors, the first numerical study on the GGB was carried out by Baron et al. [57] in 1976. They created a linear 2D (with 278 nodes) and 3D (with 120 nodes) models to investigate the dynamic behavior of the bridge along with the longitudinal-vertical and transverse-torsional directions, respectively. Both models were fixed at the towers' bases. Static, eigenvalue, and time-history analyses were carried out in this study. The model was excited under both uniform and multiple support excitations. However, only wave passage effects were considered. Also, a Rayleigh damping matrix with mass and stiffness proportional factors of 0.04805 and 0.0065 was used.

Abdel-Ghaffar [58] was one of the pioneering researchers who studied the dynamic response of suspension bridges. He employed a frequency-domain random vibration approach to analyze the GGB under multi-support excitations. Both vertical (induced by vertical and longitudinal excitations) [59], [60] and lateral [109, 110] earthquake-induced responses of the GGB under multiple support excitations were studied. 2D linearized Finite Element models developed by Abdel-Ghaffar, which were later used in several other studies [84, 85], consisted of 283 beam elements with 193 movable nodes, resulting in a system with 1146 degrees of freedom. Axial tension effects of the cables were included by the addition of a geometric stiffness matrix to the elastic stiffness matrix [63]. In the most fundamental symmetric and ten asymmetric vertical, torsional, and transverse modes, there was a very good agreement between the numerical and experimental mode shapes and natural frequencies. He also showed that his simpler 2D models work as accurately as the 3D model developed by Baron et al. [57].

As mentioned earlier, after the 1989 Loma Prieta earthquake, a series of studies for the purpose of seismic evaluation and possible retrofit was initiated. The district retained T. Y. Lin International (TYLI) to perform these evaluation studies [64] along with sub-consultants Imbsen & Associates, Inc. (IAI) and Geospectra, Inc. (GI). The 3D model of the main bridge used in that evaluation had been originally developed for TYLI's Transit Feasibility study [65]. This model was composed of 9933 frame elements connecting 4775 nodes, which was reduced by using a super-element formulation such that the total number of active degrees of freedom was around 4000 [35]. Similar to Abdel-Ghaffar's studies, dynamic loads and responses were regarded as disturbances to the dead-load configuration, so the analysis problem was linearized with respect to the dead-load state of the structure. Kinematic nonlinearity was considered by using a geometric stiffness matrix. This global model went under several analyses including linearized time-history analysis under multiple-support earthquake excitations. In addition to this global model, several, more detailed, linear and nonlinear analyses were carried out using local models—e.g., tower-to-pier connection. Results of these studies were later published in several papers and reports [38], [66]–[71]. In very recent work, Game et al. [72] created a 3D model of the GGB in Strand7 [73]. While they kindly shared their model with the authors here, the model was not accurate in geometry and details.

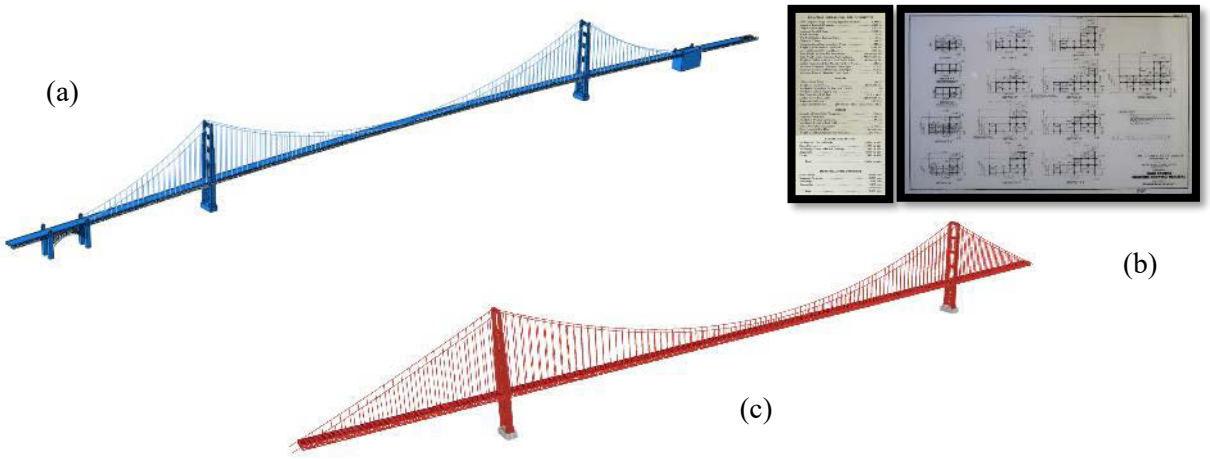

Figure 5-11: (a) Abaqus model, (b) samples of available structural details, and (c) SAP2000 model.

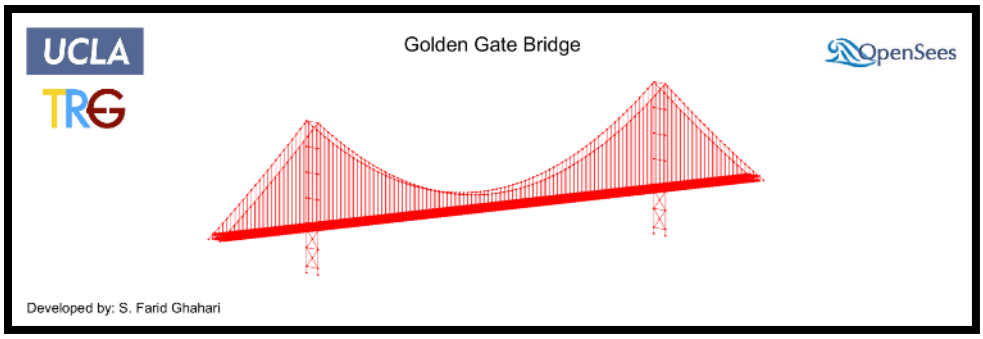

Figure 5-12: OpenSEES model of the GGB.

In the present study, a new 3D model is created. The geometry was obtained from Google Earth (see, Figure 5-3). This geometry model was then imported into ABAQUS [74] to convert faces and lines to a 3D model with solid elements. This new model is shown in Figure 5-11(a). A model with solid elements is computationally expensive and thus, it cannot be gainfully used at the present time in the output-only identification framework described in the previous section. Hence, the solid elements were replaced with structural elements and a SAP2000 was created [75]. This model is shown in Figure 5-11(c). To refine this model, publicly available details [34] on GGB—a sample of which is shown in Figure 5-11(b)—were taken into account along with all quantitative and qualitative descriptions found in other researcher's studies reviewed in prior sections. Finally, to take advantage of parallel processing, the SAP2000 model was transformed to OpenSEES [76] using a Matlab [22] interface developed by the authors, which uses the SAP Application Programming Interface (API). It is expedient to note here that the said Matlab translator code enables us to repeat the process for any other structure. The final OpenSees model is shown in Figure 5-12.

The OpenSees model is composed of more than 20,000 Degrees-Of-Freedom (DOFs) with more than 8000 frame elements and 2000 area elements. In the original SAP2000 model, the cables and hangers were modeled as cable elements and the main cables' geometry was determined iteratively, such that after imposing the dead load the cables had the internal stress and maximum sag reported by Abdel-Ghaffar [36]. In the OpenSees model, cables and hangers are modeled using co-rotational truss element with a material model that can accept initial stress. While there is no material nonlinearity in the model—except for zero-compression in cables and hangers—, geometrical nonlinearity was considered, because it is crucial for suspension bridges.

5.6. PARALLEL PROCESSING FRAMEWORK

The application of the proposed method on real-life problems, like GGB, needs huge computational resources, which hinders its application. Let's assume that we are only going to estimate unknown FIMs of the GGB at its four major piers. Assuming a 5-second time windows (t_1^m: t_2^m) with a 100 Hz sampling rate, we need to run the entire model 12001 times at each iteration. Assuming an average[10] of 10 minutes to run

[10] The analysis run time increases from first time window to the last one.

each model, it will take about 80 days to complete each iteration. Considering multiple iterations per time window, it is almost impossible to use the proposed method. To reduce this huge run time, herein, we propose a double parallel-processing framework as shown in Figure 5-13 to solve this issue. In this framework, an FE model (here an OpenSEES [76] model) is created using structural drawings and/or Google images or any available FE model. In the latter case, we do the conversion through a Matlab [22] code and the FE software's Application Programming Interface (API). The FE model is then decomposed into m domains to take advantage of Domain Decomposition (DD) capabilities of the OpenSEES. At each iteration, n (e.g., 12001) OpenSEES models are created and run in parallel by $m \times n$ devoted cores (see Figure 5-13). As the access to the High-Performance Computational (HPC) resources is getting easier every day, the proposed framework could potentially reduce that mention 80 days to even less than a minute (depending to the chosen m and inter cores' communication overhead).

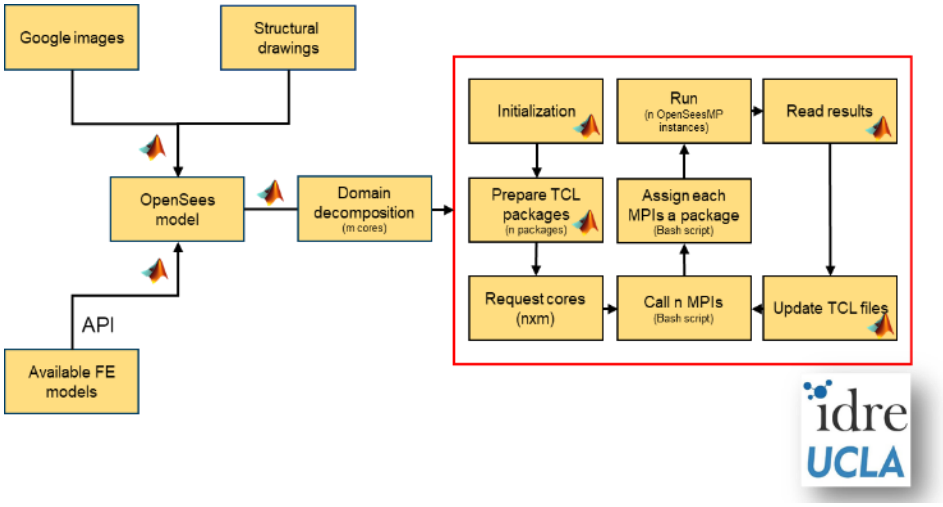

Figure 5-13: Designed double parallel processing framework.

5.7. IDENTIFIABILITY

The first step in any identification is to figure out possible sources of uncertainties and identifiability of these uncertainties. As we did not have access to the actual details of the GGB and also because this bridge experienced several retrofit stages during its service life as stated in prior sections, nearly all of the material properties are uncertain. In addition, all of the connections (e.g. spans' connections to the towers) and boundaries (e.g., soil-abutment and soil-foundation systems) are modeled by linear springs with expected values, which must be updated through the identification process. Also, parameters of the Rayleigh damping model (which is the most commonly used damping model at the present time) are considered as other potential updating parameters.

In total, there are 66 parameters that are potential candidates for identification along with FIMs. However, it is neither possible nor needed to consider all of these parameters in the identification process. Through two sifting steps, the number of updating parameters can be highly reduced. In the first step, those parameters that are free or fixed (instead of having a floating value) are delineated. For example, according

to the structural drawings and prior studies, towers do not have any relative translation with respect to the main and side spans, and thus, these connections were fixed and excluded from the identification process. Assuming non-fixed connections makes the modal properties of the model deviate from what was reported in previous studies. Because the inertial SSI effects are expected to be insignificant for GGB[11], the translational and rotational springs of the soil-foundation systems were considered to be fixed. The initial tension in cables and hangers were also excluded, because they have already been implicitly considered by applying the gravity loads. After the first sifting process, 28 parameters out of the initial 66 parameters remained as potential updating parameters, which are listed in Table 5-3. However, it is not possible to uniquely identify these parameters given the available (sparse) instrumentation layout. To examine the identifiability of these parameters, which is the second sifting step, sensitivity analyses were carried out to calculate the total information [77] for each parameter θ_i using

$$I_i = \sum_{j=1}^{m} \left(\frac{\partial y_j}{\partial \theta_i}\right)^2 \quad \text{for} \quad i = 1 \dots 28 \tag{5-1}$$

where $\partial y_j / \partial \theta_i$ is the sensitivity of response at the j-th channel with respect to θ_i, and m is the number of all recorded channels. The values of θ_i were perturbed around their nominal values and finite differences were used for approximating $\partial y_j / \partial \theta_i$. Figure 5-14(a) displays the information entropy for all these 28 parameters. Assuming a threshold of 1, for example, 7 parameters are observed to be the most informative parameters. This figure shows that from this model and the given instrumentation layout, it is not possible to infer any reliable information about the abutment's springs, primarily because GGB is a very flexible bridge.

Even then, not all of the 7 parameters can be uniquely identified. By looking at mutual information among parameters shown in Figure 5-14(b), it is seen that some parameters are highly correlated with each other. For example, the modulus of elasticity of the chords is correlated with those of the diagonal bars, the hangers, and the deck. So, these parameters were slaved and updated together. This then led to 4 important modulus parameters (namely, the moduli of elasticity of the towers, cables, chords-bars-hangers-deck, and the bottom bracings), which are identifiable through the present instrumentation layout. While the damping parameters are not very informative in comparison to the modulus parameters, they were also considered as they do not have any apparent correlation with the other parameters. So, the overall identification was carried out with 6 unknown parameters along with 6 time-series of FIMs (3 components at each pier). It was assumed that the FIMs in the south and north abutments are identical to those at the south and north piers, respectively.

Table 5-3: Candidate parameters after the first sifting step.

No.	Element	Parameter
1	Bottom Bracing	Elastic Modules
2	Cable	Elastic Modules
3	Chord	Elastic Modules

[11] In fact, this is why we choose GGB for the present validating study.

4	Deck	Elastic Modules
5	Diagonal Bar	Elastic Modules
6	Floor Beam	Elastic Modules
7	Hanger	Elastic Modules
8	Kneebrace	Elastic Modules
9	Top Bracing	Elastic Modules
10	Tower	Elastic Modules
11	Track Girder	Elastic Modules
12	Transverse Strut	Elastic Modules
13	Vertical Rod	Elastic Modules
14	Vertical Bar	Elastic Modules
15	South Tower-South Side Span	Spring Stiffness, M2
16	North Tower-North Side Span	Spring Stiffness, M2
17	South Abutment	Spring Stiffness, P
18	South Abutment	Spring Stiffness, V2
19	South Abutment	Spring Stiffness, V3
20	South Abutment	Spring Stiffness, T
21	South Abutment	Spring Stiffness, M2
22	North Abutment	Spring Stiffness, P
23	North Abutment	Spring Stiffness, V2
24	North Abutment	Spring Stiffness, V3
25	North Abutment	Spring Stiffness, T
26	North Abutment	Spring Stiffness, M2
27	Damping	Alpha
28	Damping	beta

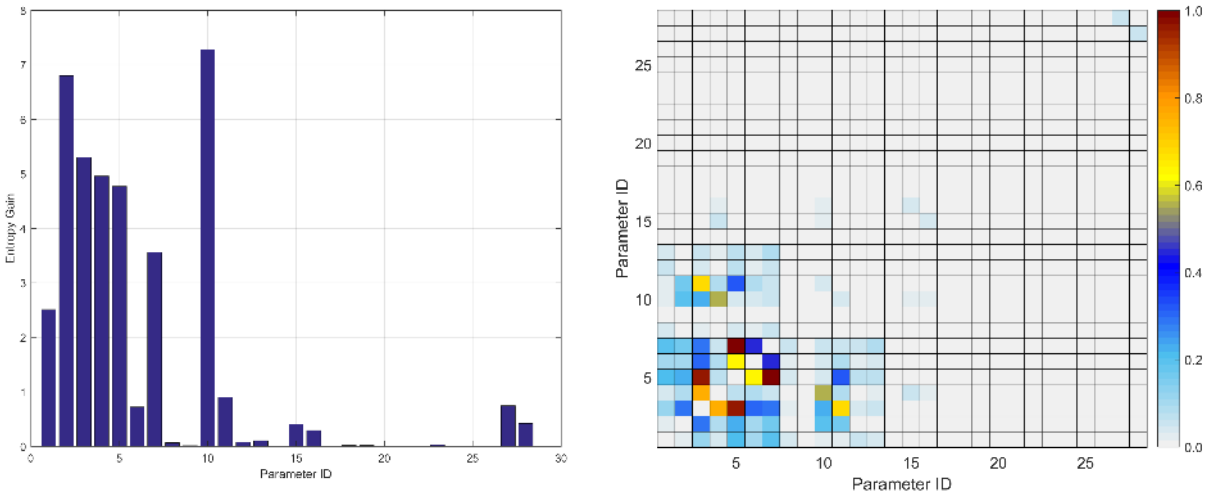

(a) Information entropy

(b) Mutual information

Figure 5-14: Identifiability analysis. (a) information entropy for each parameter, (b) mutual information among parameters, and (left) list of parameters.

5.8. IDENTIFICATION RESULTS

5.8.1 Verification: Simulation Data

Before applying the proposed identification method to real-life data, it is crucial to verify the method through simulated data. The proposed method is applicable to a wide range of scenarios—i.e., linear, nonlinear, Input-Output (IO), or Output-Only (OO). As an initial test, we used it for input-output identification. Input-output identification is quite useful, because one way to consider soil-structure interaction effects is to modify the input motions to include those feedback effects. In other words, it is possible to exclude compliance beyond a location by imposing a prescribed motion at that location. In fact, Shirkhande and Gupta [78] followed this same approach to estimate the responses of the GGB using a fixed-base model. In addition, the complexity of an OO identification task will decrease if an IO identification using foundation-level measurements is carried out first to estimate the superstructure's parameters. Of course, it should be noted here that the IO approach is possible and useful for GGB because measurements at its foundations are available.

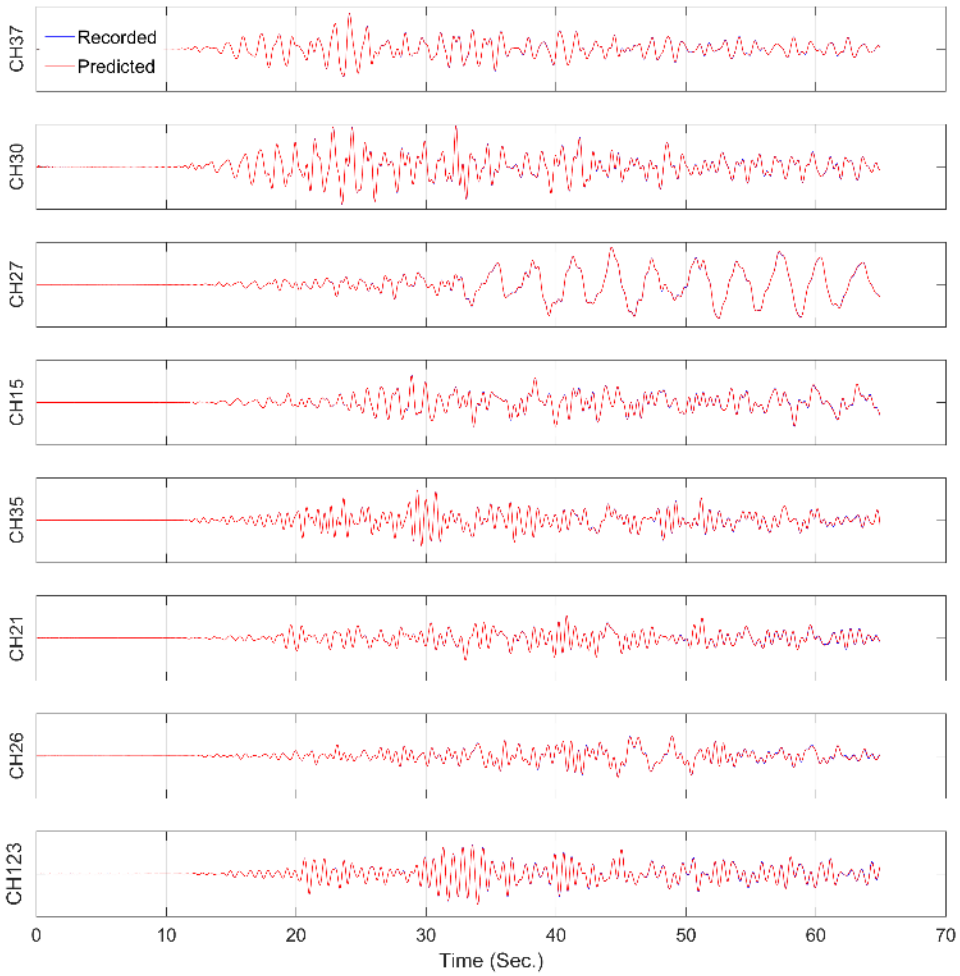

Figure 5-15: Comparison between simulated and predicted acceleration responses at select channels (IO case).

The IO identification on the simulated data of the GGB was carried out and Figure 5-15 displays both the recorded (i.e., synthetically simulated) and the predicted (at the last iteration of the last updating step) responses at some selected channels. As seen, the prediction is perfect. While a 50% initial error was added on to all 6 parameters, the final/converged results show 0.03%, 0.04%, 0.23%, 1.59%, 2.38%, and 13.76% errors at the end of updating process. As expected, the damping parameters are not identified as accurately as the others in which the stiffness proportional factor is more erroneous, which is in agreement with Figure 5-14(a).

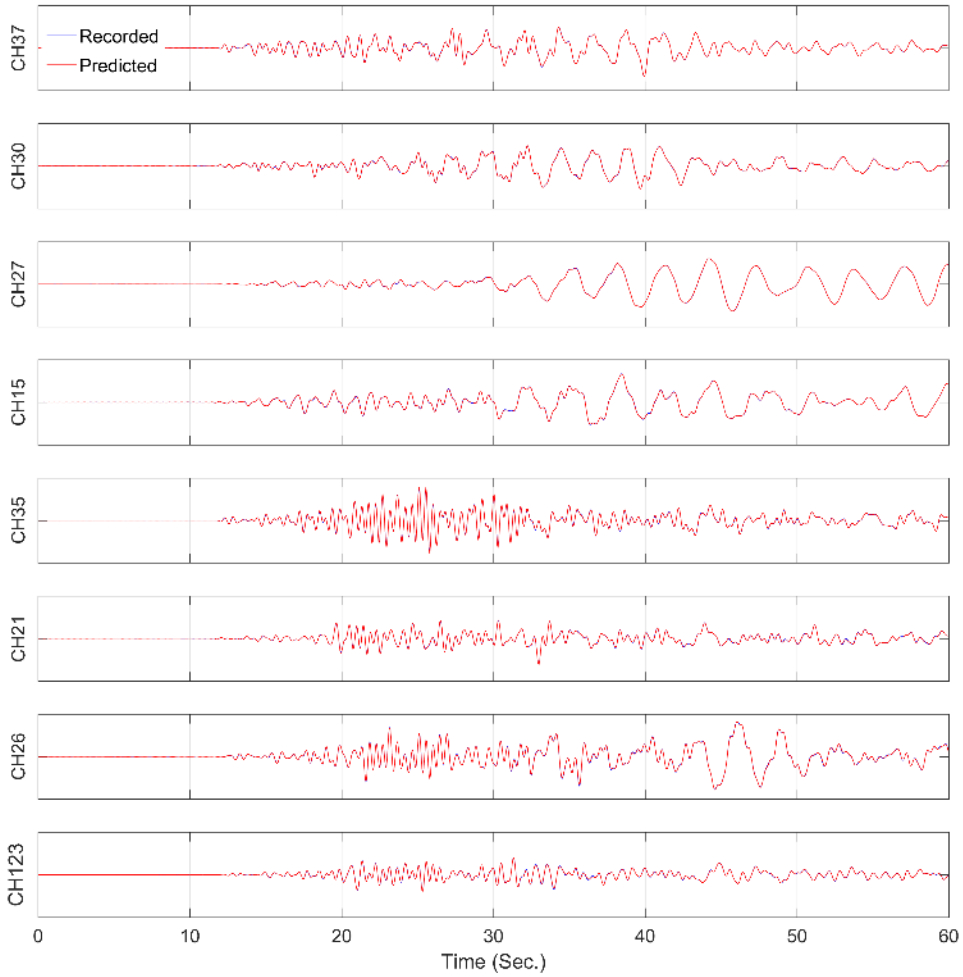

Figure 5-16: Comparison between simulated and predicted acceleration responses at select channels (OO case).

While it is possible to use information obtained in the IO identification step to reduce the parameter uncertainties in the OO identification, we opted not to use it because the response of the foundations/abutments might not be recorded at all piers in real-life. Therefore, we carried out OO identification for all 6 parameters together with the FIMs. Assuming an initial error of 25%, we obtained 0.05%, 3.51%, 0.19%, 0.01%, 8.47%, and 16.33% for the moduli of elasticity of the towers, cables, chords, and braces, and for the mass and stiffness proportional damping coefficients, respectively. Comparisons of

recorded and predicted responses at some selected channels are shown in Figure 5-16. As seen, even though some of the parameters are not identified very accurately, the predicted responses are very close to the recorded ones.

Finally, the most important identification results are FIMs. The identified FIMs are shown in Figure 5-17 along with their exact counterparts. As this figure indicates, the input motions are identified with very good accuracy.

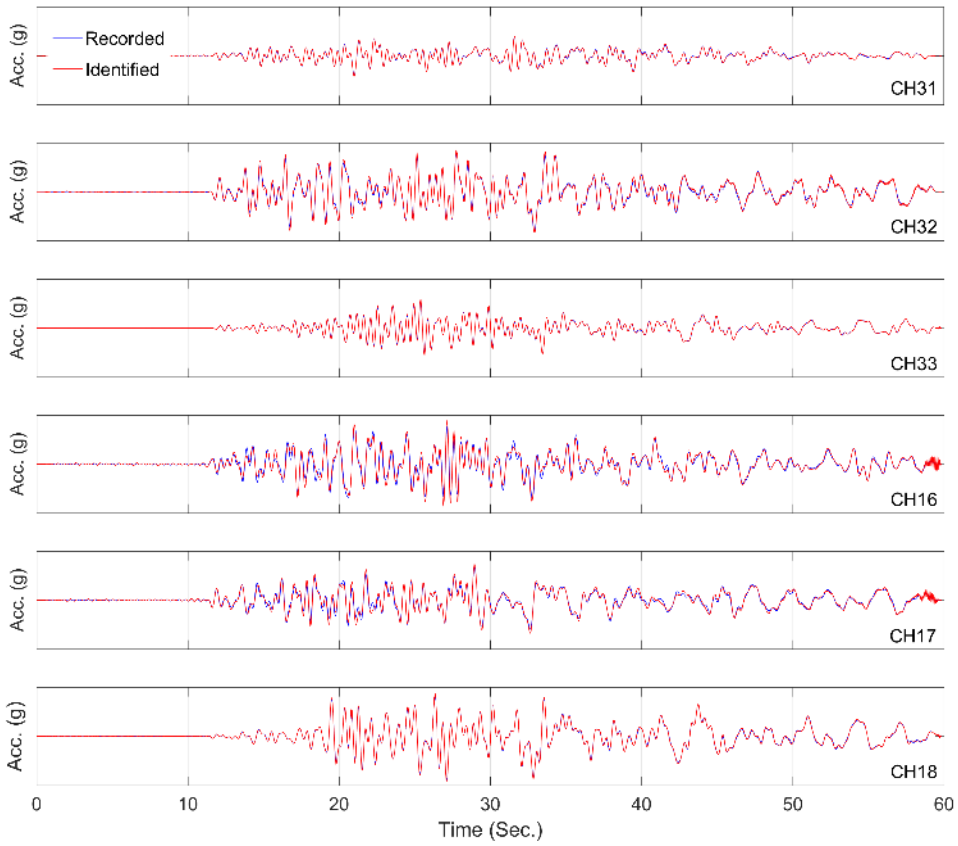

Figure 5-17: Comparison between exact and identified FIMs (verification study).

5.8.2 Validation: Real-Life Data

In the validation study, the simulated signals are replaced with their real-life recorded counterparts, and the same IO and OO identification steps are carried out as in the previous section. Figure 5-18 compares the recorded and predicted acceleration responses at various selected channels after the IO identification. As expected, the results are not as good as synthetic data. However, the results are not uniformly good/bad, and the level of accuracy varies among channels. The predicted responses at channels 37, 30, 35, and 21 are very close to the real-life data. All these channels are on the towers or very close to the towers. The response predicted at Channel 15 is acceptable, although there are some high-frequency components which are not captured in the prediction. The major discrepancies are observed at channels 26, 27, and 123. All these channels are on the main span. Several reasons can be cited as possible sources of these

inconsistencies. First, we did not have access to all of the structural details of the bridge, so there could be some modeling errors. Second, the responses at these channels are highly affected by other co-existing excitations such as wind and moving vehicles, which are not considered here. Finally, the damping was modeled through the Rayleigh method, which may not be able to accurately model the damping ratios for all modes. This could be significant for the main-span channels, because many modes are contributing to these signals and there is also likely effects of wind-structure interaction generating some form of radiation damping, while the channels on the tower mostly contain only a few fundamental modes of the system.

While wide constraint boundaries were considered for the updating parameters during optimization, all of the elasticity moduli are identified around $2 \times 10^{11}\ \mathrm{N/m^2}$ except those of the bottom bracings, which are around $2.5 \times 10^{11}\ \mathrm{N/m^2}$. This indicates that perhaps the dimensions of the bottom bracing elements were underestimated in the model. The identified Rayleigh damping parameters are both around 0.1.

The predicted responses and identified FIMs obtained from the output-only identification are shown in Figure 5-19 and Figure 5-20, respectively. As seen, the level of similarity between the recorded and predicted responses is close to what we observed for the input-output case (Figure 5-15), and here the FIMs are also identified. We had assumed that accelerations recorded on the foundations are the true FIMs (i.e., inertial SSI is negligible), which are also shown in Figure 5-20. From this figure, it can be observed that there is a fairly good agreement between the identified FIMs and the accelerations recorded at the foundations in the transverse direction. However, there are no similarities between recorded and predicted responses in the vertical and longitudinal directions. It is not surprising to see such discrepancies in the vertical direction, because the available vertical channels are all on the deck, which are mostly affected by the longitudinal excitation rather than the vertical excitation. However, we should have observed similarities in the longitudinal direction. Without a further detailed study wherein modeling errors are reduced, we believe that this discrepancy could be due to kinematic interaction. In the presence of kinematic interaction, there would be a rocking excitation, which is not considered here. If so, then the identified horizontal FIM has to also compensate for the rocking excitation effect by imposing larger amplitudes. Reduction of superstructure modeling errors, as well as consideration of foundation rocking, would like to improve the accuracy attained in a follow-up validation study.

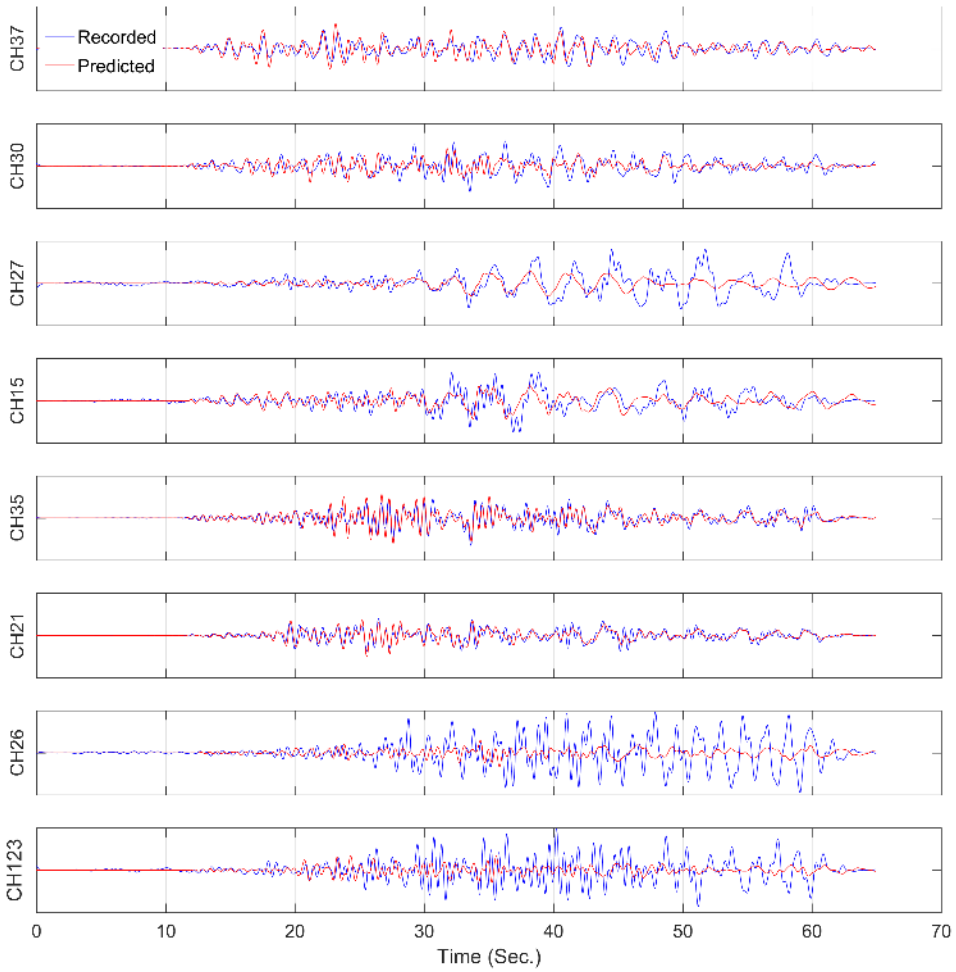

Figure 5-18: Comparison between recorded and predicted acceleration responses at select channels (IO case).

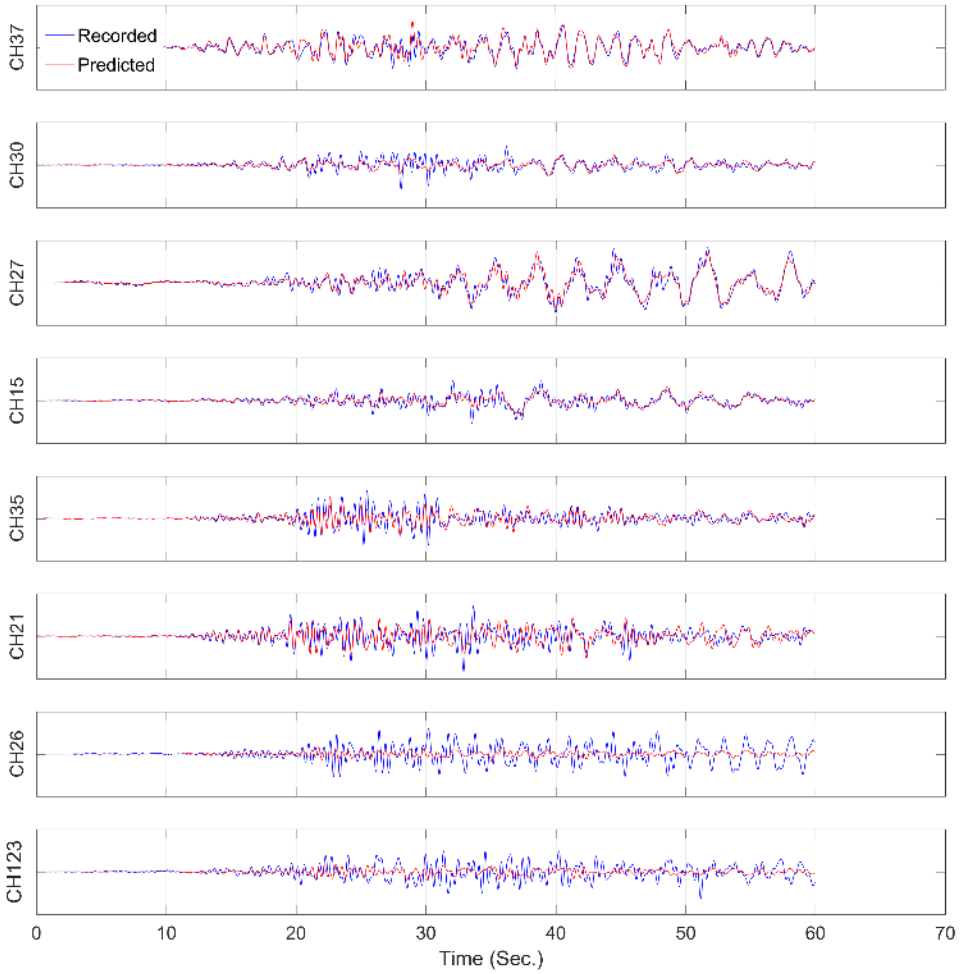

Figure 5-19: Comparison between recorded and predicted acceleration responses at select channels (OO case).

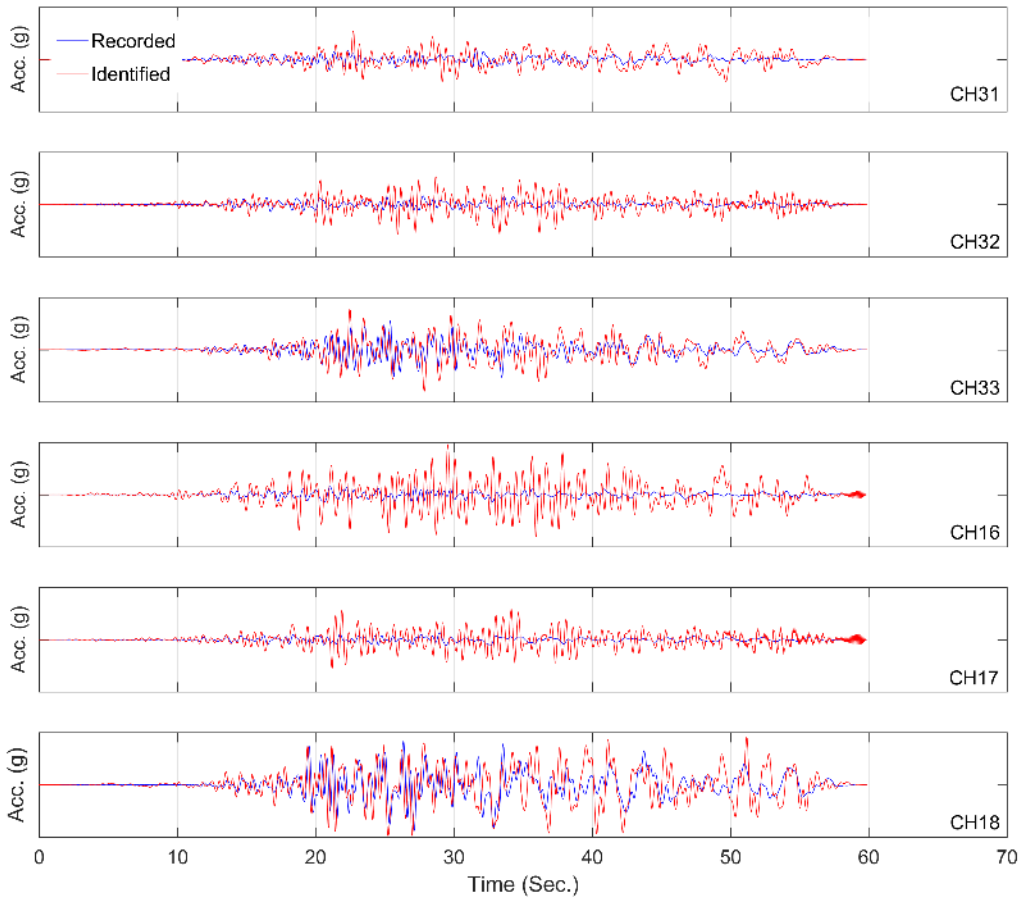

Figure 5-20: Comparison between recorded foundation responses and identified FIMs.

CHAPTER 6: A PILOT STUDY ON THE MELOLAND ROAD OVERPASS

6.1. INTRODUCTION

In the previous chapter, the proposed method was verified for a large-scale bridge with only geometrical nonlinearity. Herein, we show the performance of the method by using several sets of real earthquake data recorded by a densely instrumented bridge, the Meloland Road Overpass, which is believed to be highly influenced by soil-structure interaction effects.

6.2. THE STRUCTURAL SYSTEM

The Meloland Road Overpass (MRO), shown in Figure 6-1, was designed in 1968-69 and constructed in 1970 above interstate 8 near El Centro in south-eastern California (32.7735 N, 115.4481 W). It is a reinforced concrete bridge with two continuous 31.7 m (104 ft) spans and monolithic abutments. It has a single column with 1.5 m (5 ft) diameter and 5.2 m (17 ft) above ground height. The column is placed on a $4.6 \times 4.6 \times 1$ m ($15 \times 15 \times 3.5$ ft) concrete foundation cap which is supported by 25 timber piles. The bridge deck is a 1.7 m (5.5 ft) prestressed reinforced three-cell box girder which is fully attached to the column through a 1.7×1.8 m (5.5×6 ft) rigid cap beam. It is also supported at both ends by integral monolithic straight abutments. Each abutment is supported on a row of 7 timber piles in the transverse direction.

The MRO has been the subject of many studies in the past few decades. Indeed, this bridge is one of the earliest seismically instrumented bridges in the US which was instrumented in 1978 by 26 channels through CSMIP [23] and recorded 1979 Imperial Valley earthquake less than one year later [79]. The instrumentation was upgraded in 1991 to 32 channels as a part of the interagency agreement between Caltrans and DOC. The distribution of these 32 channels is shown in Figure 6-2. Through this dense instrumentation, several earthquakes have been recorded as listed in Table 6-1. Instrumentation is not the only reason for which MRO was studied extensively. As the bridge is quite stiff, the effects of Soil-Structure Interaction (SSI) has been well observed in this structure [11]. In the following paragraphs, some of the prominent studies on the MRO are briefly reviewed.

Table 6-1: Earthquakes recorded by MRO instrumentation system (Last update: 02/17/2018)

No.	Earthquake	Date	Mag.	Dist. (km)	PGA (g)	PSA (g)	Comment
1							Recorded by 26 channels
2	Superstition Hills	11/23/1987	6.2 Mw	46.0	0.030	0.070	Data is not available
3	Superstition Hills	11/24/1987	6.6 ML	46.3	0.182	0.242	17 channels available
4	Cerro Prieto	02/08/2008	5.4 ML	37.2	0.020	0.058	---
5	Cerro Prieto	02/11/2008	5.1 ML	45.8	0.012	0.035	---
6	Cerro Prieto	02/11/2008	5.0 ML	37.1	0.014	0.042	---
7	Calexico	11/20/2008	5.0 ML	50.5	0.017	0.027	---
8	Calexico	12/27/2008	4.5 ML	24.5	0.006	0.020	---
9	Calexico	12/30/2009	5.8 Mw	41.5	0.174	0.509	28 channels available
10	Calexico	12/30/2009	4.8 M	35.0	0.015	0.039	---
11	Calexico	04/04/2010	7.2 ML	55.2	0.213	0.474	28 channels available
12	Calexico	05/22/2010	4.9 Mw	35.1	0.031	0.061	---
13	Borrego Springs	07/07/2010	5.4 ML	120.8	0.012	0.054	---
14	Borrego Springs	06/10/2016	5.2 Mw	118.1	0.013	0.031	---

Figure 6-1: Meloland Road Overpass.

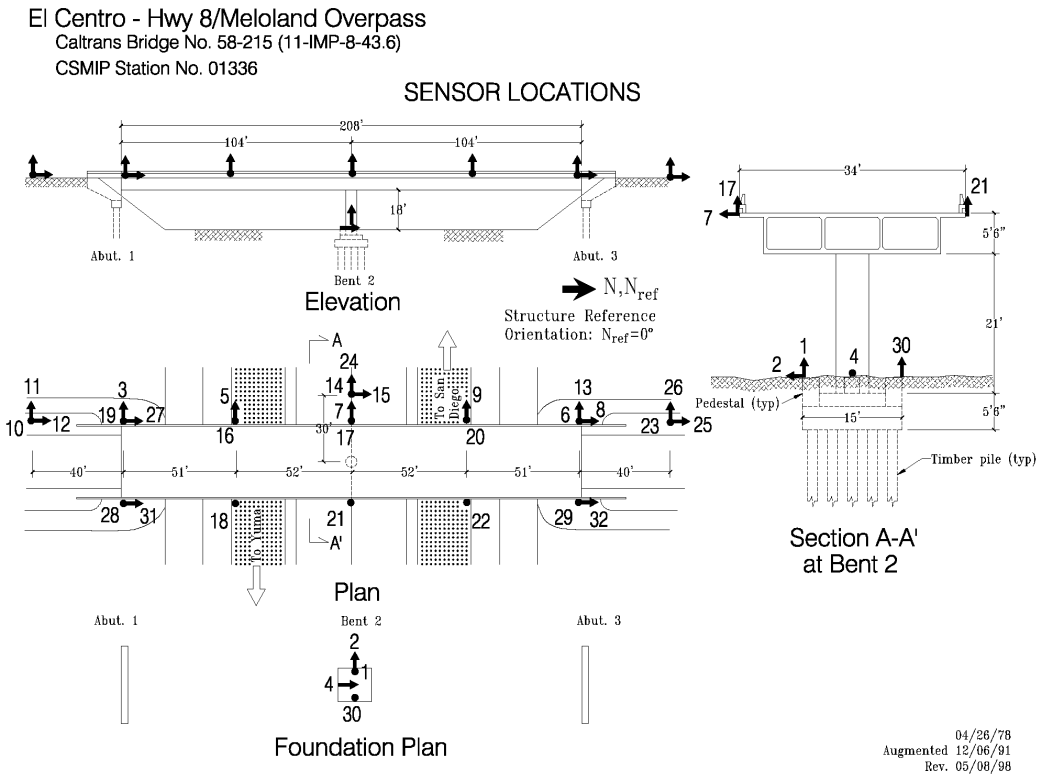

Figure 6-2: Instrumentation layout [23].

Werner et al. [79] were the first researchers who applied a system identification method to identify modal characteristics of the MRO from seismic signals recorded during the 1979 Imperial Valley earthquake. They concluded that 1- linear models work excellently for this bridge, 2- the transverse response of the MRO is mostly controlled by the movement of the abutments, while the deck moves almost rigidly, and 3- the vertical response of the bridge deck at the middle of spans is dominated by a single vertical-translation mode, while it is the vertical motion of the central pier base and torsional behavior of the deck which controls the deck's vertical response above the central pier. As there is no clear distinction between input and output signal in the MRO, they carried out two sets of identification study. In the "case 1", they used channels 6, 13, 3, 19, 1, and 2 as input data and channels 9, 20, 22, 1, 17, 21, 5, 16, and 18 as output signal (note that at that time channels 27 to 32 were not available). It is well accepted that if a DOF's movement is prescribed in system identification, the compliance beyond that DOF would be excluded from the system (see, e.g., [80]). In other words, they have identified a so-called pseudo-flexible system [81] in which compliance provided by the soil is partially included in the identified system through, for example, central pier foundation rotation. They identified deck vertical symmetric and transverse symmetric modes around 4.74 Hz and 3.72 Hz, respectively, through the case 1 scenario. In case 2, they consider motions on the bridge edges as output too and used channels 23, 26, 10, and 11 as input. In this case, they found deck vertical symmetric mode around 4.56 Hz, which is quite close to case 1, while transverse mode around 2.47 Hz, which is far from case 1. This study clearly showed the importance of the soil-foundation flexibility in the dynamic response of the MRO.

In a study by Wilson and Tan [82], Single-Input-Single-Output (SISO) output-error identification approach [83] was employed to identify the fundamental mode of the abutment-embankment of the MRO. They used Free-Field Motion (FFM) channel in the transverse direction, i.e. channel 24, as input and channels 11 and 26 on the embankment as output. They found that the frequency of the identified system, which was believed to be the abutment-embankment system[12], varies between 2.43 and 1.34 Hz during the Imperial Valley earthquake 1979 due to soil nonlinearity. In an almost concurrent study, Marie et al. [84] modeled the MRO using a stick model and considered rotational compliance provided by abutment/embankment by putting rotational springs at the boundaries, as translational motions at boundaries were used as input motions. By comparing natural frequencies from the model with those identified by Werner et al. [79], they concluded that rotational stiffness of the abutment-embankment about vertical and transverse axis should be almost negligible. Also, the rotational stiffness about the longitudinal direction is very large (~fixed). In the central pier, soil-foundation stiffness about the vertical axis is infinity, while in two other directions pile cap could rock.

In 2001, Zhang and Makris carried out an extensive research study on the MRO [85], which were published later in 2002 as two separate papers [11], [86]. They developed a simple but yet dependable method to estimate the seismic response of freeway overcrossings and validated it by using data from the MRO. In that study, but kinematic and inertial SSI [13] were taken into account. Arici and Mosalam [10] employed parametric and non-parametric system identification methods multi-input-single-output to identify MRO's modal characteristics. However, as it is not exactly determined which channels were being used as input, it is hard to make statements on modal characteristics under which boundary conditions have been identified.

With the increasing software and hardware capabilities to analyze large scale FE models, several studies were carried out in which MRO along with its surrounding soil boundaries was directly modeled. Studies by Kwon and Elnashai [87], Kotsoglu and Pantazopoulou [88], and Rahmani et al. [89] are among some distinguished works in this area. Based on these types of analyses, it was even shown that favorable substructure methodology to analyze the soil-structure system could result in some errors in forward simulations [90].

As can be seen from the brief review above, while the MRO has been studied by several research groups, there have been some important questions not answered yet. There is no study in which the contribution of various damping sources is determined. Also, FIMs are only studied in a direct way; that is, they are estimated using numerical modeling the embankment/abutments. Moreover, while soil-foundation impedance functions (springs and dashpots) are identified by matching identified and predicted modal characteristics, uncertainties related to the measurement noises are not quantified. Herein, we employ the proposed solution to deeply identify the MRO from several earthquake data sets, to be able to answer the questions above. To do so, we create a details FE model of the superstructure and identify its uncertain

[12] It is obvious that output signal is still influenced by the bridge structure too.

parameters (material's properties and Rayleigh damping parameters) along with soil-foundation stiffness and damping. In addition, FIMs at abutments and central pier are simultaneously identified.

6.3. FINITE ELEMENT MODELING

The MRO is a simple structure and its FE model has been already created by several researchers with various level of details. Shamsabadi et al. [91] has already created a highly accurate model of this bridge in various FE software packages, whose SAP2000 [75] version shown in Figure 6-3 is used here. The model with its boundary elements showed relatively close agreement with identification results obtained from an ambient modal identification study [92]. The deck is modeled as a combination of several shell elements to be able to accurately capture the box-girder section. Cap beam and column are modeled using frame elements. Back walls of the abutments are also modeled using shell elements to mimic rigidity provided by these elements.

As we are going to use this model within the FE model updating framework, we converted this model to the Opensees [76] which could be called in parallel to speed up analyses. Using a nominal value of $22\ GPa$ for concrete's modulus of elasticity [85], first ten numerically calculated mode shapes and natural frequencies of the MRO under fixed-base boundary conditions are shown in Figure 6-4. These natural frequencies must be higher than or equal to those values identified by Werner et al. [79] in Case 1, as their results are pseudo-flexible base frequencies. As seen, the first vertical symmetric fixed-base natural frequency is 5.49 Hz (mode 3), which is higher than 4.74 Hz obtained in their study. Also, the first transverse symmetric mode's fixed-base frequency is 5.28 Hz (mode 2), which is much higher than 3.72 Hz identified by Werner et al. [79] in Case 1. To further verify the feasibility of the developed FE model of the superstructure, we compare our results with a more recent identification study by Mosquera et al. [93], in which they used more recent 2008 earthquake data sets recorded after instrumentation upgrade in 1991. Based on the chosen input channels (1, 2, 3, 4, 6, 8, 13, 19, 27, 28, 29, 30, 31, and 32), identified frequencies should be very close to the ideal fixed-base values. They identified six modal frequencies corresponding to f_1, f_2, f_3, f_4, f_5T, f_9 as 3.43, 4.47, 4.92, 7.32, 10.20, and 14.79 Hz, respectively. As seen, while all these values are close to those obtained from the FE model. However, they are all smaller than what is obtained from FE model, which is expected because they are identified from a naturally flexible-base system.

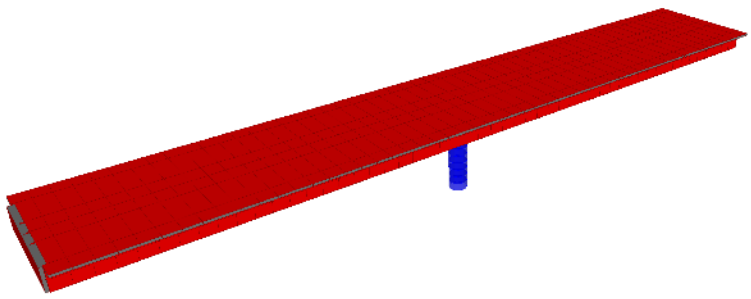

Figure 6-3: SAP2000 [75] model of the MRO.

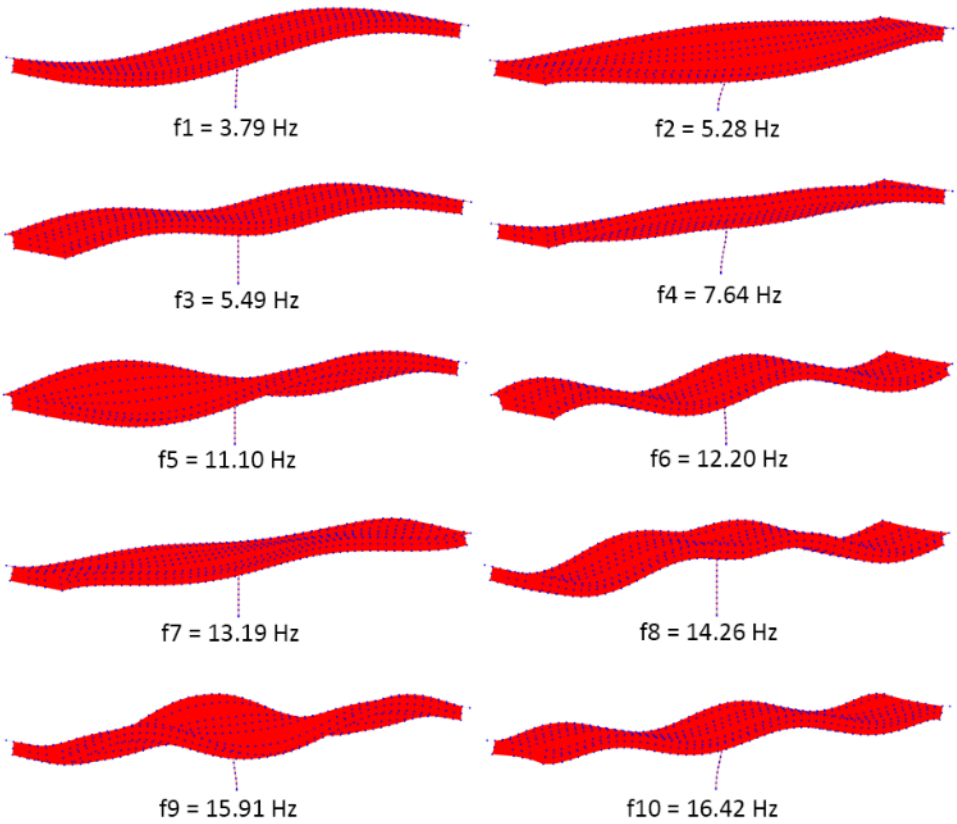

Figure 6-4: First 10 mode shapes of the MRO obtained from eigen analysis in Opensees.

6.4. IDENTIFICATION RESULTS

Among the available earthquake data sets shown in Table 6-1, we only use events 4-8, 10, and 12-14, because there were some issues with other events as reported in the Comment column of Table 6-1. In this chapter, we are interested in a large number of parameters and FIMs, so we consider a linear-elastic material behavior for structural elements. Also, soil-structure interaction effects are modeled by using discrete springs and dashpots at boundaries of the model (at left and right ends of the deck and at the bottom of the column). Note that we consider the same parameters for left and right abutments. As the superstructure is considered linear-elastic, concrete's elastic modulus and Rayleigh damping parameters are only uncertain parameters which are going to be identified along with soil-foundation parameters and input motions. Due to significant kinematic interaction effects reported in the literature for this bridge, we consider different FIMs at abutments and column (totally 6 unknown FIMs).

Comparison between recorded and predicted acceleration responses for all events are shown in Figure 6-5 to Figure 6-12. To show the performance of the updated model, we compared the difference or summation of Channels 20 and 22, for example, instead of a direct comparison. As seen, the predicted and recorded responses in all events are almost matched.

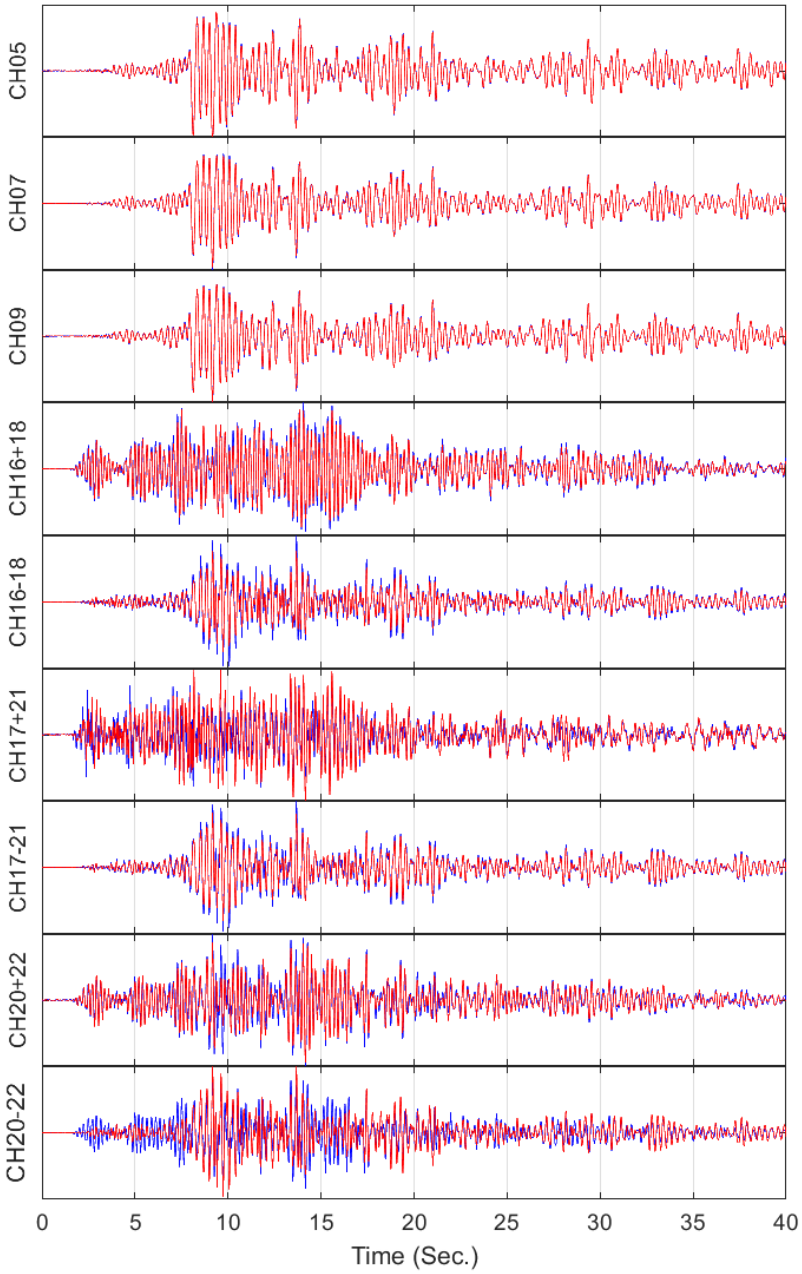

Figure 6-5: Comparison between recorded (blue) and predicted (red) acceleration responses in Event 4.

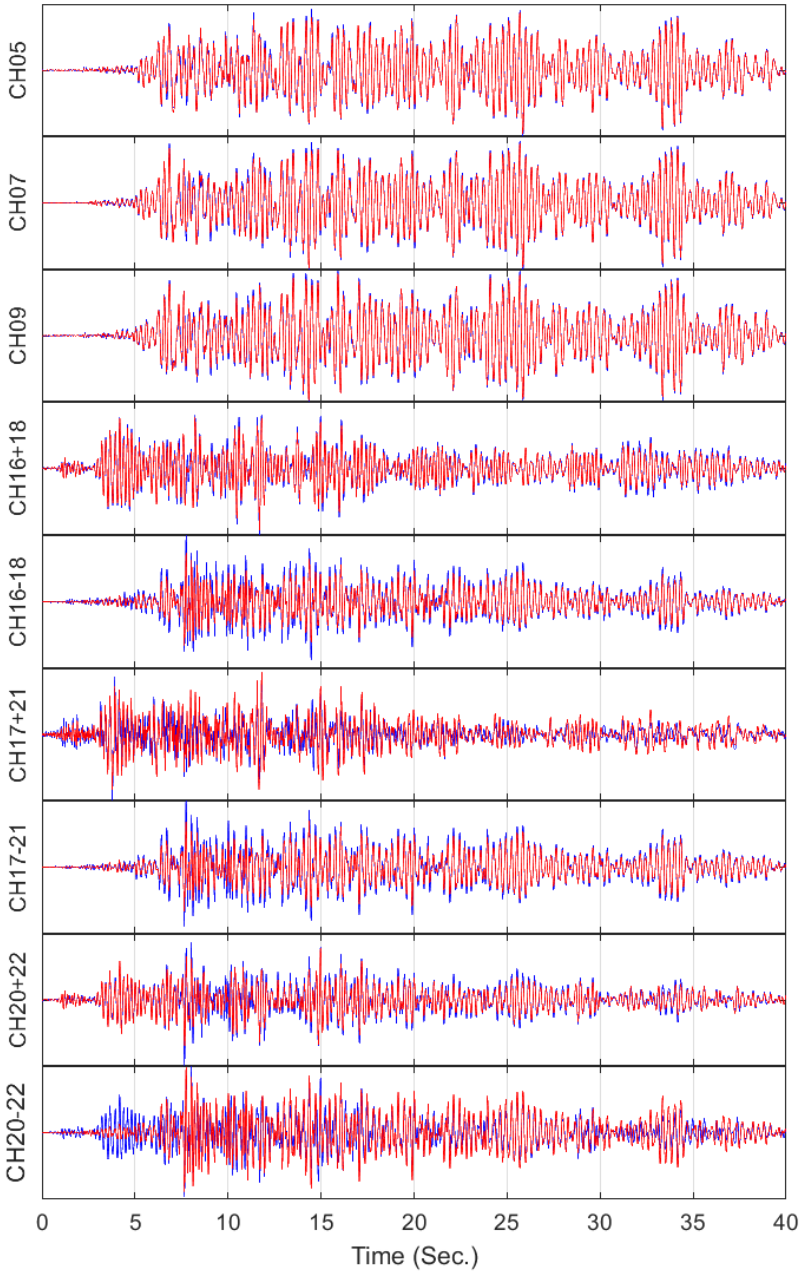

Figure 6-6: Comparison between recorded (blue) and predicted (red) acceleration responses in Event 5.

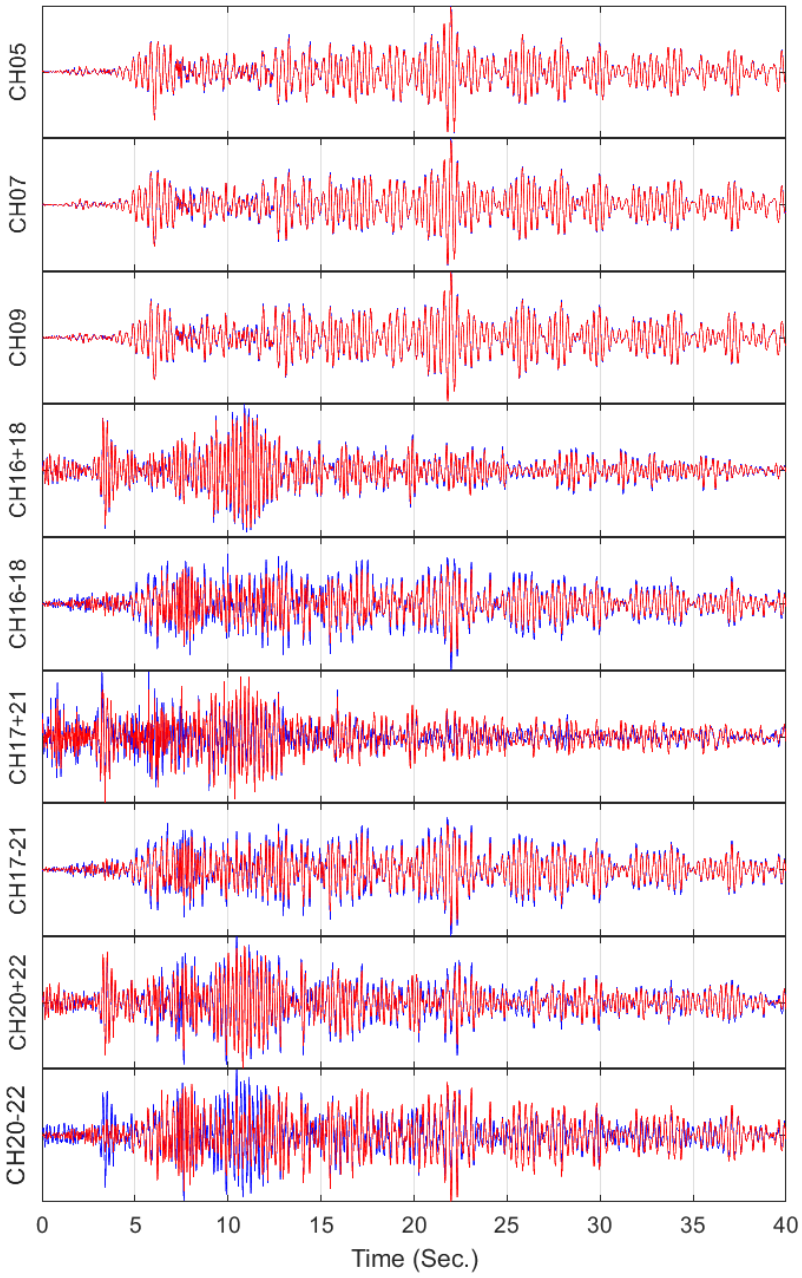

Figure 6-7: Comparison between recorded (blue) and predicted (red) acceleration responses in Event 6.

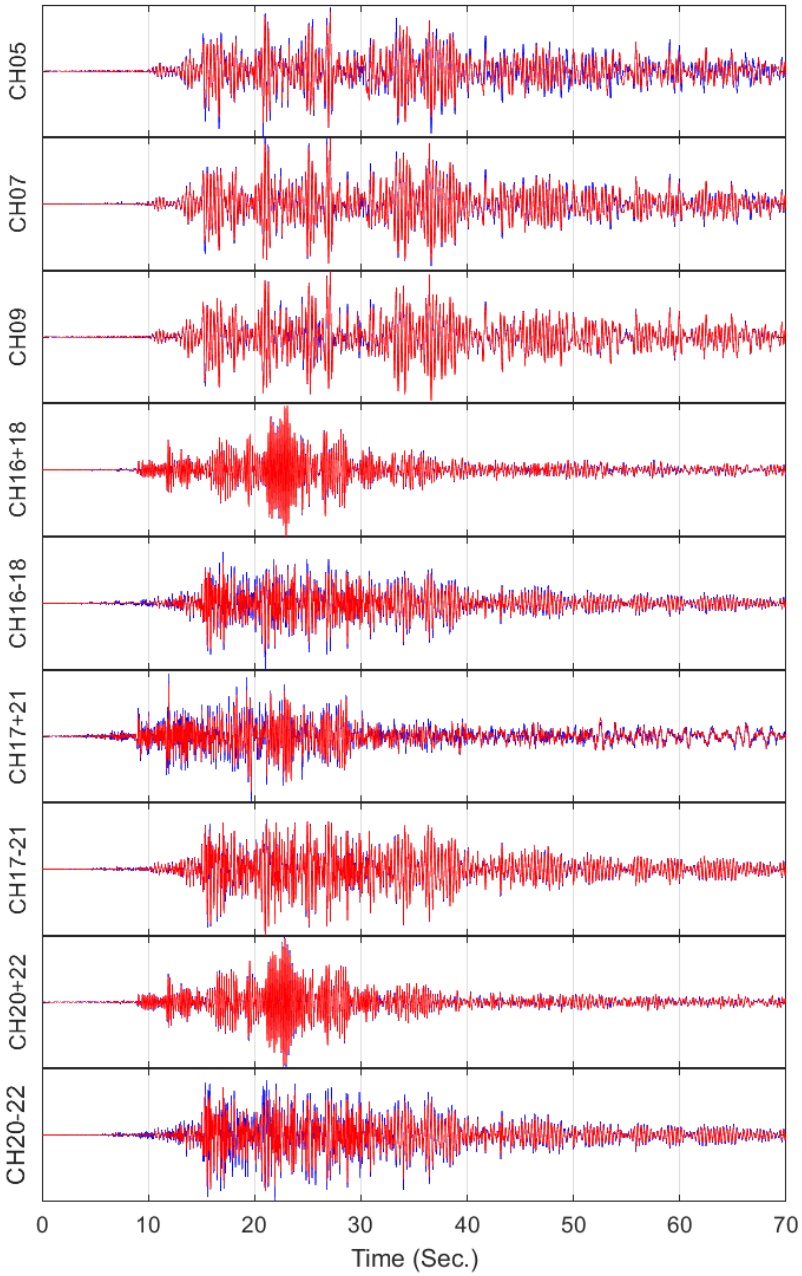

Figure 6-8: Comparison between recorded (blue) and predicted (red) acceleration responses in Event 7.

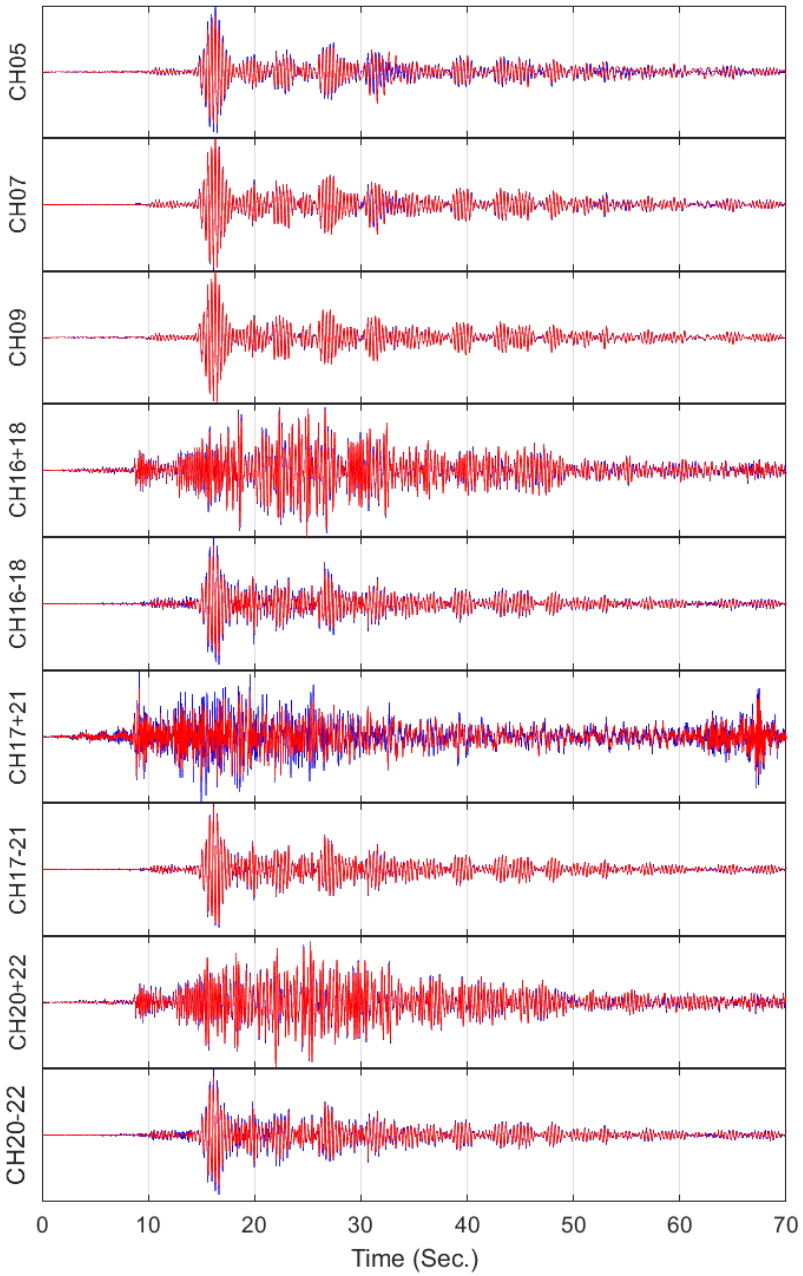

Figure 6-9: Comparison between recorded (blue) and predicted (red) acceleration responses in Event 10.

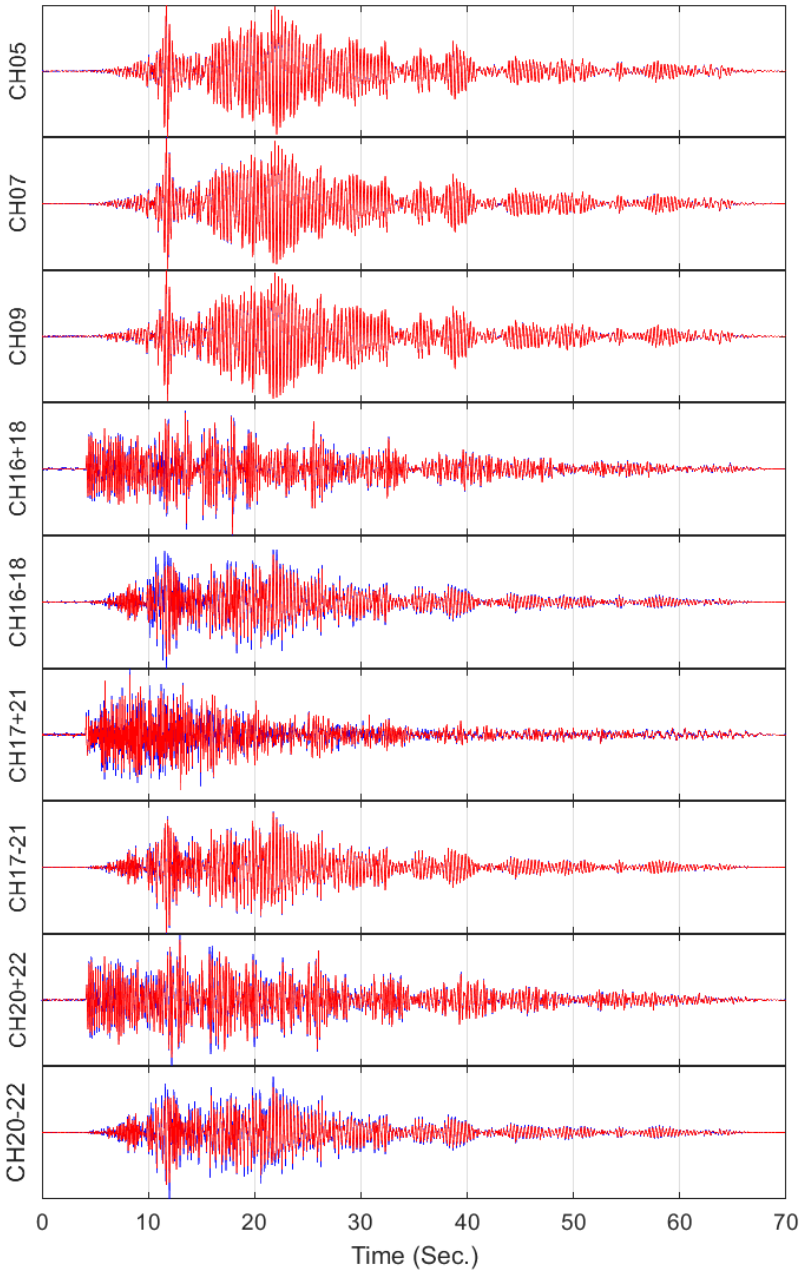

Figure 6-10: Comparison between recorded (blue) and predicted (red) acceleration responses in Event 12.

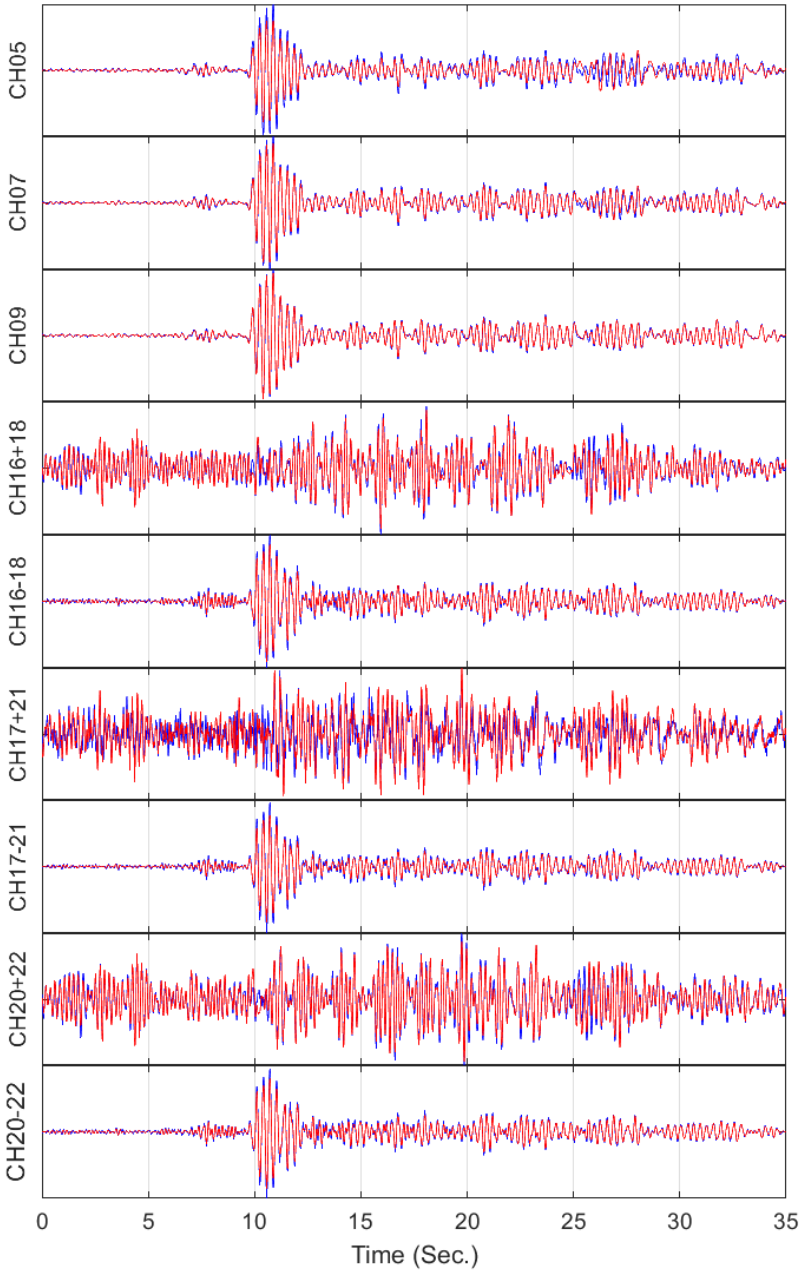

Figure 6-11: Comparison between recorded (blue) and predicted (red) acceleration responses in Event 13.

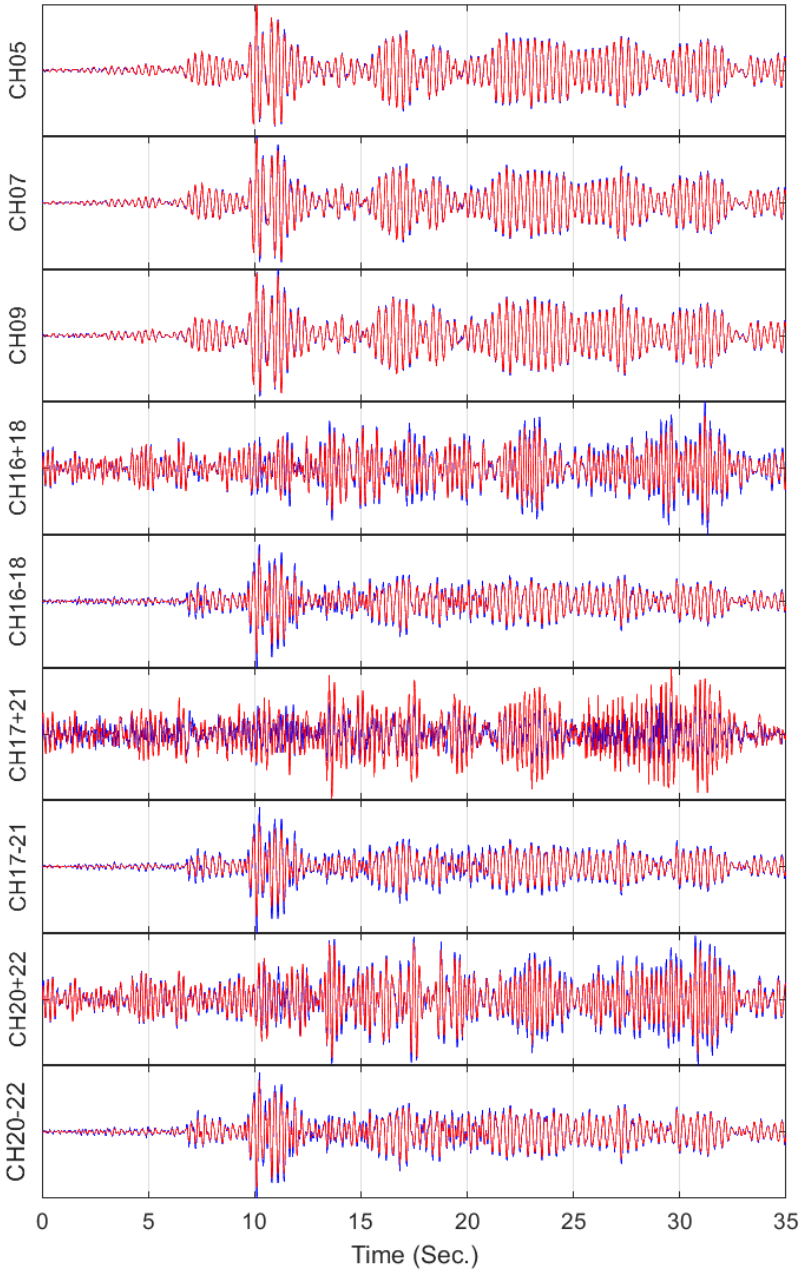

Figure 6-12: Comparison between recorded (blue) and predicted (red) acceleration responses in Event 14.

The 21 identified parameters by which these perfect response matches are obtained are shown in Table 6-2 and Table 6-3. Table 6-2 shows stiffness-related parameters along with the estimation Coefficient of Variation (COV), while Table 6-2 presents damping-related parameters and their COVs. The initial values are set based on the values found in the literature or based on the judgment. As seen, there is event-dependency in all parameters. That is, frequency content and level of intensity of the input motions change the identified values. Two examples of such inter-event variation are shown in Figure 6-13 along with their $\pm$ one standard deviation. As seen, while c_z^c (soil-foundation damping in verthe tical direction at central

column) is close to the value suggested by Rahmani et al. [89], the corresponding stiffness is always below the reference value. The benefit of the proposed solution is that parameters are identified along with their COVs, so it is possible to understand which value is not reliable (for example, responses are not too sensitive to its variation. As an example, rotational stiffness of the abutment around the transverse axis (k_{yy}^{a}) is about 20 $MN.m$ in most events in Table 6-2, while it is obtained 76 $MN.m$ in the Event 13. First of all, as seen, the estimated COVs are generally too high (~10%) in all events showing that this parameter is not a very observable parameter in the current instrumentation. Moreover, the COV of this parameter is 44% in the Event 13 which depicts that this specific identified value is not reliable at all.

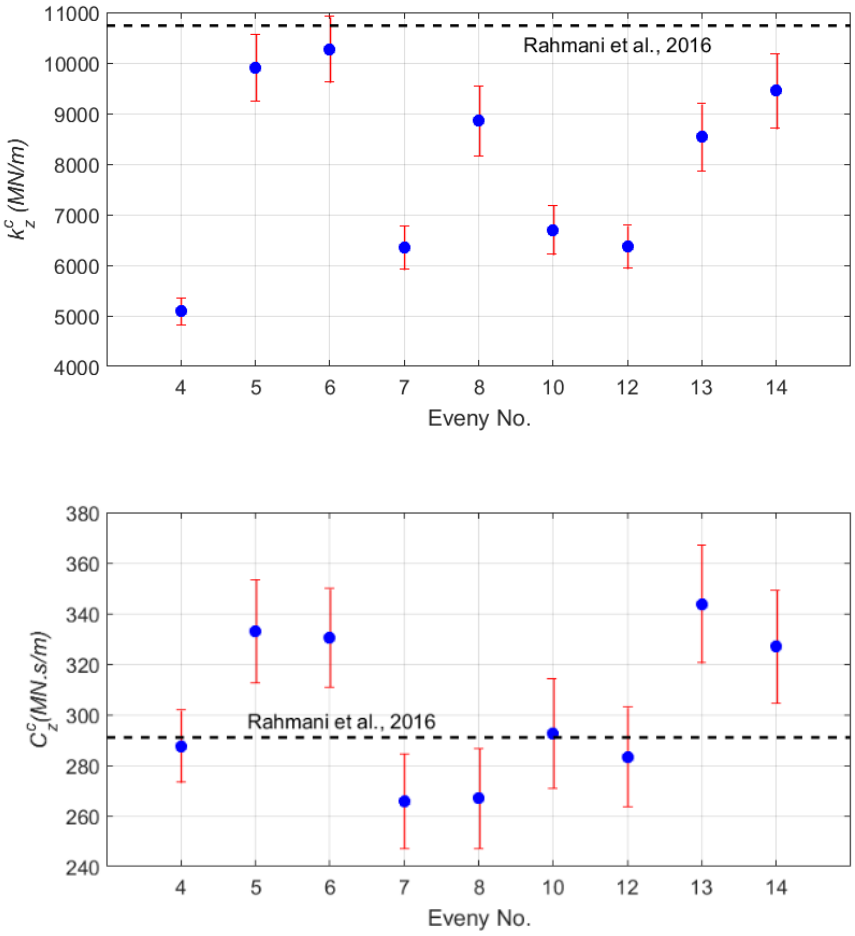

Figure 6-13: Identified parameters along with their variations.

Table 6-2: Mean (and %COV) values of the identified stiffness parameters.

			Event No.								
	Parameter	**Initial**	**4**	**5**	**6**	**7**	**8**	**10**	**12**	**13**	**14**
1	$E_c(GPa)$	22 [11]	20.3 (0.11)	23.4 (0.16)	21.7 (0.13)	16.5 (0.14)	21.5 (0.24)	15.2 (0.19)	17.9 (0.13)	22.2 (0.31)	25.7 (0.46)
2	$k_x^a(MN/m)$	410 [90]	5.9 (0.52)	418.7 (1.61)	423.6 (1.50)	369.9 (2.63)	412.1 (2.75)	325.1 (3.20)	415.0 (1.14)	412.3 (2.99)	448.5 (2.84)
6	$k_y^a(MN/m)$	49 [90]	43.8 (0.18)	49.7 (0.24)	54.9 (0.23)	48.2 (0.52)	54.8 (0.48)	41.5 (0.38)	44.6 (0.22)	55.2 (0.39)	54.1 (0.41)
4	$k_z^a(MN/m)$	418 [94]	483.4 (1.87)	429.5 (2.51)	326.4 (1.97)	124.7 (0.91)	207.6 (2.80)	102.1 (1.52)	106.8 (0.85)	388.2 (4.80)	482.9 (5.36)
8	$k_{xx}^a(MN.m)$	113 [84]	4350.9 (0.11)	3659.4 (0.16)	4243.0 (0.14)	7460.4 (0.32)	2110.2 (0.32)	4771.1 (0.28)	6382.1 (0.19)	2257.3 (0.28)	2152.9 (0.33)
12	$k_{yy}^a(MN.m)$	2260 [84]	23.2 (3.94)	25.6 (10.24)	22.8 (6.12)	13.9 (10.10)	26.9 (32.85)	26.1 (7.91)	11.6 (12.46)	76.0 (44.41)	44.8 (38.50)
10	$k_{zz}^a(MN.m)$	294 [84]	1239.4 (2.05)	787.1 (3.54)	1173.2 (2.28)	8.3 (10.13)	779.4 (3.70)	7.9 (10.21)	8.0 (10.49)	402.6 (7.19)	366.4 (7.94)
16	$k_x^c(MN/m)$	273 [90]	177.8 (0.69)	180.0 (0.88)	207.1 (0.84)	245.0 (2.08)	64.8 (1.43)	223.6 (1.92)	252.5 (1.03)	193.9 (1.68)	167.5 (1.87)
16	$k_y^c(MN/m)$	273	177.8 (0.69)	180.0 (0.88)	207.1 (0.84)	245.0 (2.08)	64.8 (1.43)	223.6 (1.92)	252.5 (1.03)	193.9 (1.68)	167.5 (1.87)
14	$k_z^c(MN/m)$	10740 [90]	5094.0 (5.25)	9908.4 (6.64)	10271.0 (6.29)	6351.5 (6.86)	8856.4 (7.86)	6698.0 (7.22)	6369.1 (6.68)	8535.1 (7.80)	9449.4 (7.81)
18	$k_{xx}^c(MN.m)$	19116 [90]	12484.0 (0.76)	10202.0 (1.95)	11224.0 (1.43)	59309 (4.49)	13235.0 (6.46)	19079.0 (2.60)	18445.0 (1.39)	6479.4 (1.58)	6187.2 (2.25)
18	$k_{yy}^c(MN.m)$	19116	12484.0 (0.76)	10202.0 (1.95)	11224.0 (1.43)	59309 (4.49)	13235.0 (6.46)	19079.0 (2.60)	18445.0 (1.39)	6479.4 (1.58)	6187.2 (2.25)

Table 6-3: Mean (and %COV) values of the identified damping parameters.

			Event No.								
	Parameter	**Initial**	**4**	**5**	**6**	**7**	**8**	**10**	**12**	**13**	**14**
20	α	0.04	0.04 (1.97)	0.04 (1.67)	0.04 (1.00)	0.05 (11.38)	0.04 (2.21)	0.11 (7.73)	0.14 (4.33)	0.04 (7.96)	0.04 (6.02)
21	β	0.0004	0.0019 (0.94)	0.0026 (1.16)	0.0021 (1.01)	0.0004 (5.22)	0.0014 (4.57)	0.0006 (2.43)	0.0005 (3.52)	0.0013 (2.56)	0.0030 (3.70)
3	$c_x^a(MNs/m)$	11 [90]	3.6 (0.97)	12.1 (1.94)	11.0 (1.87)	12.0 (3.26)	12.0 (3.31)	11.7 (3.65)	12.7 (1.32)	11.9 (3.67)	13.2 (3.31)
7	$c_y^a(MNs/m)$	1 [90]	1.4 (0.61)	0.9 (1.36)	1.3 (0.75)	2.1 (1.34)	0.6 (4.68)	1.4 (1.38)	1.9 (0.65)	1.2 (2.09)	0.8 (3.55)
5	$c_z^a(MN.s/m)$	11	16.6 (2.15)	13.2 (2.94)	9.6 (2.58)	4.0 (3.08)	10.9 (3.26)	2.2 (4.61)	3.1 (2.10)	12.3 (5.55)	11.2 (6.84)
9	$c_{xx}^a(MN.s)$	10	24.4 (0.65)	51.1 (0.43)	57.3 (0.36)	0.5 (10.19)	62.9 (0.56)	0.7 (9.16)	0.4 (11.84)	33.4 (0.87)	40.1 (0.88)
13	$c_{yy}^a(MN.s)$	10	0.3 (64.30)	4.6 (15.76)	2.3 (21.00)	0.2 (9.74)	5.3 (16.01)	0.2 (9.84)	0.1 (10.26)	9.9 (9.21)	8.2 (11.91)
11	$c_{zz}^a(MN.s)$	10	1.2 (48.17)	0.1 (236.03)	0.2 (65.24)	0.7 (10.08)	2.8 (34.95)	0.7 (9.92)	0.8 (8.47)	3.4 (28.51)	5.7 (17.36)
17	$c_x^c(MN.s/m)$	8 [90]	11.3 (0.91)	9.3 (1.17)	6.7 (1.26)	26.5 (2.18)	3.7 (2.25)	21.8 (2.28)	29.7 (1.04)	7.2 (2.22)	8.4 (2.18)
17	$c_y^c(MN.s/m)$	8	11.3 (0.91)	9.3 (1.17)	6.7 (1.26)	26.5 (2.18)	3.7 (2.25)	21.8 (2.28)	29.7 (1.04)	7.2 (2.22)	8.4 (2.18)
15	$c_z^c(MN.s/m)$	291 [90]	187.6 (4.95)	333.0 (6.14)	330.4 (5.91)	265.9 (7.04)	266.9 (7.39)	292.7 (7.43)	283.3 (6.94)	343.8 (6.79)	326.9 (6.83)
19	$c_{xx}^c(MN.s)$	532 [90]	121.9 (1.29)	159.0 (2.89)	104.6 (4.00)	220.5 (8.80)	255.2 (11.68)	107.8 (2.73)	203.9 (4.67)	16.2 (1.56)	80.1 (7.04)
19	$c_{yy}^c(MN.s)$	532	121.9 (1.29)	159.0 (2.89)	104.6 (4.00)	220.5 (8.80)	255.2 (11.68)	107.8 (2.73)	203.9 (4.67)	16.2 (1.56)	80.1 (7.04)

Finally, it is interesting and important to see the variation of the inherent damping during these nine events. To do so, the obtained modal damping ratios in the frequency range of 2 to 16 Hz are shown in Figure 6-14. While the level of earthquake intensity shown in Peak Structural Acceleration (PSA) values is

low in all these events, there is a trend in the inherent damping. Neglecting those events whose PSA are shown in red, the inherent damping decreases when the level of bridge response increases. While this may look counter-intuitive at first, it is expected for this specific bridge structure. Indeed, when the level of excitation increases the bridge mostly remains undeformed and moves as a rigid body due to significant soil-structure interaction effects. So, the contribution of superstructure's damping reduces.

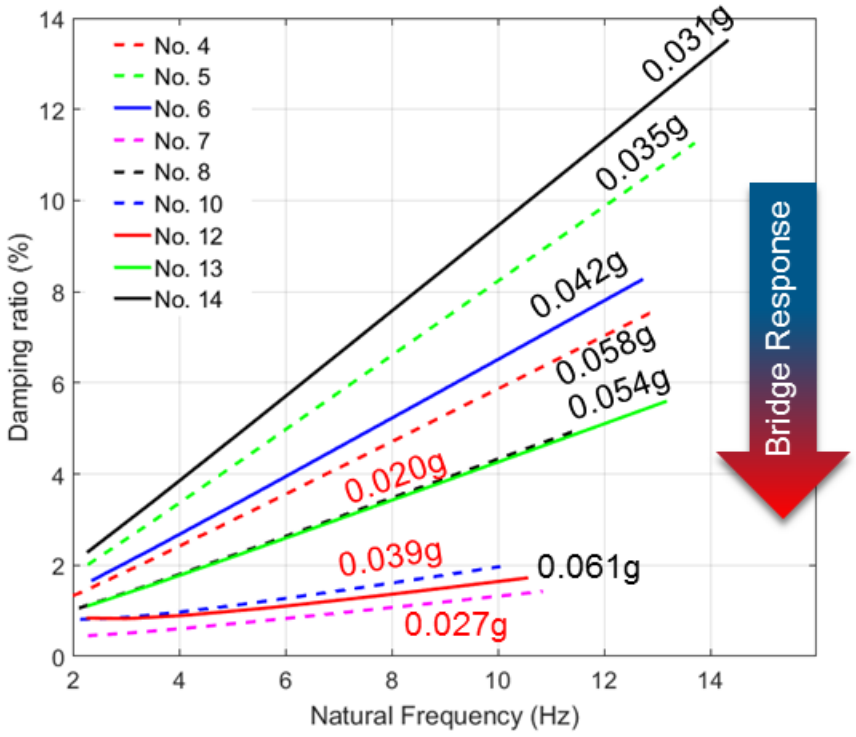

Figure 6-14: the identified modal damping ratios from MRO earthquake data sets.

CHAPTER 7: REAL-LIFE APPLICATION

7.1. THE SAN ROQUE CANYON BRIDGE

The GGB case was shown to see the applicability and performance of the proposed framework for a large scale linear system with only geometrical nonlinearity. Also, the MRO was used to show how the method could work for a bridge hugely affected by SSI contribution. Herein, we verify the performance of the method for a medium-size bridge structure under uniform excitation but with various sources of material nonlinearity. We later use this example to test the method under real-life data, as we are able to create a very detailed FE model of the bridge due to the access to its all as-built structural drawings.

The San Roque Canyon (SRC) Bridge Figure 7-1 is over San Roque Creek river in Santa Barbara, California. It is a continuous concrete box girder bridge with two hexagonal concrete piers (one column per pier). It has spread footings supporting the piers and seat type abutments at its two ends. The SRC was instrumented in 1996 (12 years after its construction) under the interagency agreement between Caltrans and DOC. As shown in Figure 7-2, there are six accelerometers on the bridge and three at a nearby free-field station. Three sensors out of six accelerometers measure the response of the deck in the transverse direction, one accelerometer records the vertical motion of the deck at its center, and two other accelerometers recording the longitudinal response of the deck, especially to check if the deck hits the abutment backwall.

Figure 7-1: The SRC bridge.

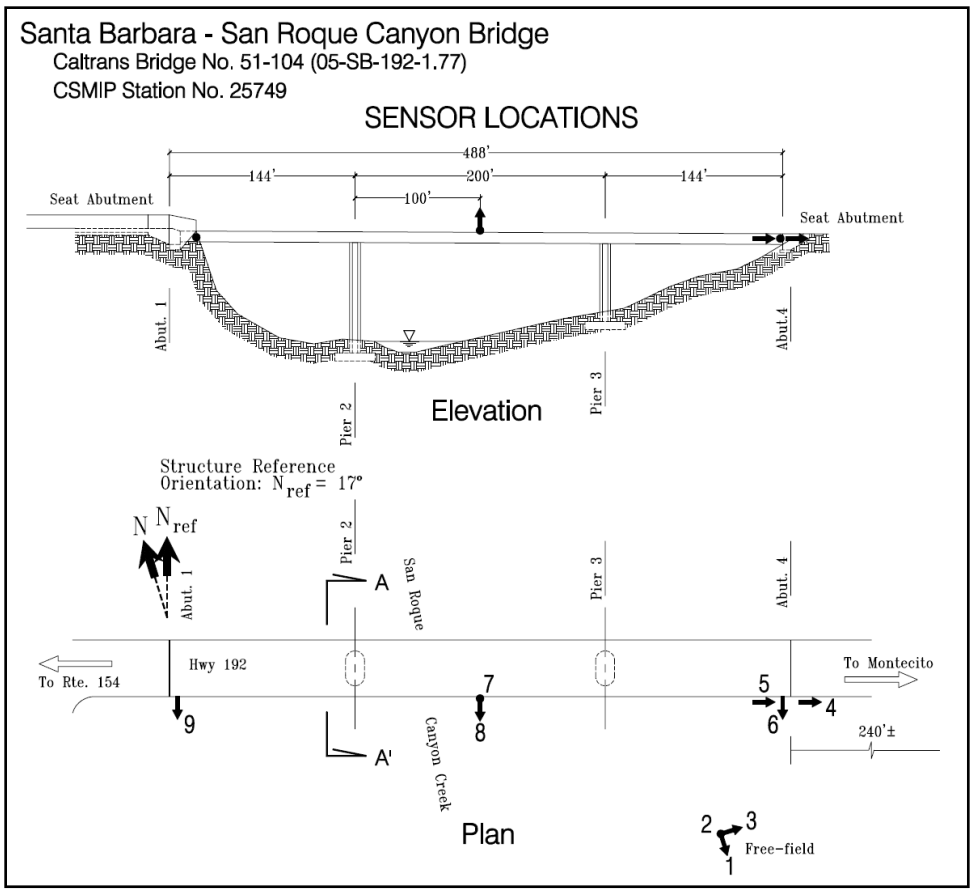

Figure 7-2: The SRC bridge instrumentation layout.

We create a very detailed FE model of the SRC bridge based on the most recent technical resources on various parts of a bridge (e.g., [95]). The nominal values of all the material properties are taken from as-built structural drawings and Caltrans Seismic Design Criteria [96]. This model is schematically shown in Figure 7-3. Based on the recommendation provided in [97], the deck (No 1) is modeled using linear-elastic beam elements, as it is capacity protected. To account for the torsional effects, torsional mass moment of inertia is added at nodes (No. 2). The foundation at piers is modeled using linear-elastic shell elements (No. 3). To connect columns to the deck, small rigid frame elements (No. 4) are used to account for rigidity provided by the cap beam. Rigid elements are also used in the model to represent the end of the deck and body of the abutment system (shown in blue). Nonlinear force-based beam-column elements are utilized to model the columns (No. 5). Five fiber-discretized sections are used along the height of each element considering 5 integration points [98]. These sections are carefully created to replicate variation of the columns in height. The confinement effects are taken into account based on the Mander's model [99]. Also, the elastic shear and torsional stiffnesses are aggregated with the uniaxial fibers. To connect the end of the deck to the abutment system, rigid frame elements with the number of nodes (No. 6) equal to the number of bearing pads are added at two ends of the deck. These nodes are connected to the rigid abutment body (think of it as stemwall) through bearing pads and shear keys. Bearing pads (No. 7) provide compression-

only vertical compliance up to a specific deformation. They also resist longitudinal motion through friction (No. 8) which is modeled by elastic-perfectly plastic material in the model. Once the gap between the deck and the abutment backwall is closed, the backwall stiffness along with soil pressure provide resistant. The backwall stiffness (No. 9), which is calculated using the theory of plate and shell [100], is modeled using compression-only gap-elastic-perfectly-plastic behavior. The transverse response of the deck is controlled by the parallel combination of the bearing pad stiffness and shear keys (No. 10). According to the structural drawings, the shear keys of this bridge are ductile so the model proposed by Silva et al. [101] is used to consider the nonlinear compression-only behavior of the shear keys after the gap between the deck and the shear key closes.

Soil-Structure Interaction effects are considered in two levels: 1- near-field, and 2- far-field effects. The near-filed effects are the nonlinear soil response at the very close region to the structure, which is highly evident at the abutments. In the longitudinal direction, passive soil pressure behind the backwall (No. 11) provides resistance which is modeled using Generalized Hyperbolic Force–Displacement (GHFD) backbone curve [102]. The most common soil type in the abutments in California is silty-sand [103] whose properties are taken from [104]. At the end of near-filed soil springs, the far-filed effects of the soil (No. 12) is modeled using the approximate formula provided by Gazetas [105]. At the foundations, the near-filed effects are neglected and only far-filed effects in all six degrees of freedom (No. 13) are modeled using approximate formula proposed by Pais and Kausel [106].

In addition to the explicit sources of damping in the model (dashpots and nonlinear elements), the inherent damping property of the structure is modeled using Rayleigh damping. We make sure to apply stiffness-proportional damping only to the non-rigid deck and column elements.

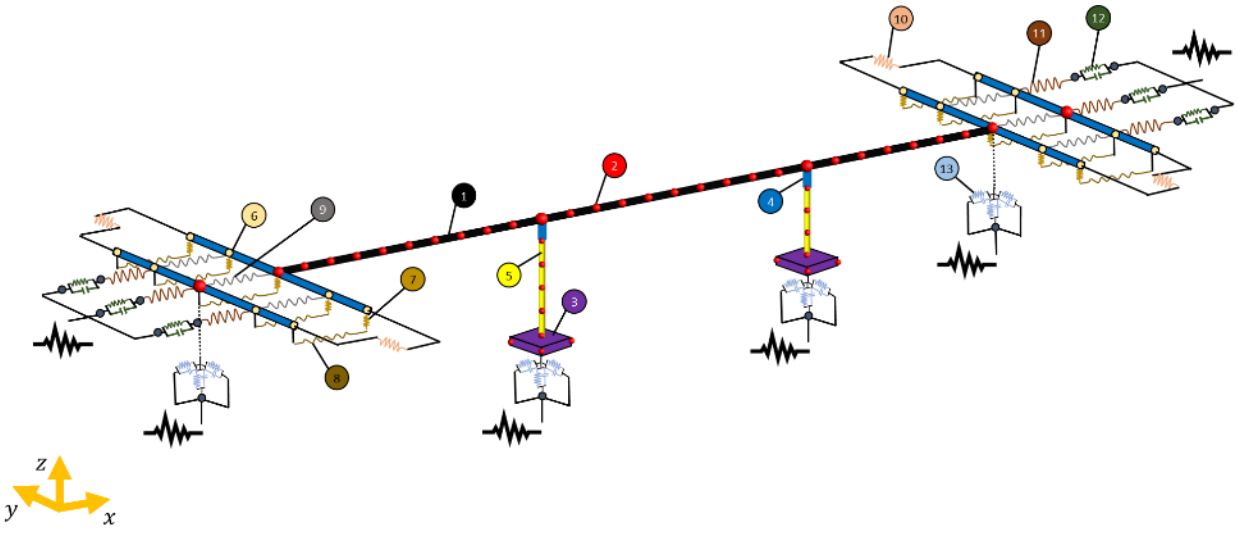

Figure 7-3: The components of the SRC Finite Element model.

Since its instrumentation, the SRC bridge has recorded five earthquakes whose data is publicly available in Center for Engineering Strong Motion Data (CESMD)[13]. These earthquakes are listed in Table 7-1 along with their date, distance to the SRC bridge, the Peak Ground Acceleration (PGA) and the Peak Structural Acceleration (PSA) at the SRC site. All these real earthquake data will be later analyzed.

Table 7-1: Earthquakes recorded by the SRC bridge.

No.	Earthquake	Date	Distance (km)	PGA (g)	PSA (g)
1	San Simeon	12/22/2003	187.0	0.015	0.045
2	Isla Vista	05/09/2004	27.2	0.016	0.047
3	Isla Vista	05/29/2013	18.0	0.041	0.152
4	Montecito	04/23/2017	9.0	0.022	0.046
5	Santa Cruz	04/05/2018	67.9	0.016	0.058

7.1.1 Identifiability

Similar to the previous cases, we first carry out the identifiability study to find out the most identifiable parameters by using available instrumentation. A list of nominated structural parameters after first sifting step is shown in Table 7-2. Excluding some obvious unidentifiable parameters (e.g., far-field soil-foundation rotational stiffness about the transverse direction at abutments), we include all physically meaningful parameters, and we carry out the identifiability using Isla Vista 2004 earthquake excitation.

To find the most identifiable parameters, the information gain is shown in Figure 7-4. As seen, there are 10 parameters which are potentially identifiable due to their high information gain. These parameters sorted in descending order are parameters No. 5, 1, 4, 3, 19, 33, 34, 20, 13, and 15. To see the mutual information among these parameters, Figure 7-5 is shown. As seen, there is no significant mutual information among the first four dominant parameters (5, 1, 4, and 3), so they are chosen to be parameters which can be identified. However, some level of correlation is observed among other parameters. To make this existing correlation more visible, Figure 7-6, which is a scaled version of Figure 7-5, is presented. Parameters 15 and 13 are removed from the list, because they are sharing information with two already selected parameters 5 and 3, respectively. While parameters 33 and 34 have a mutual correlation with each other, we keep them because they are not dependent on other parameters can we are interested in their collective effects, i.e., inherent damping. The two remaining parameters are parameters No. 19 and 20, which are identifiable according to the carried out identifiability analysis. However, the verification studies part of which will be presented later showed that they cannot be identified accurately. The reason is that the identifiability analysis was carried out assuming known input, while the identification is carried out in an output-only way. As the number of sensors in the longitudinal direction is very limited, the input is

[13] https://www.cesmd.org

unknown, and there are already several parameters contributing in this direction, parameters No. 19 and 20 (respectively, the far-field soil-foundation stiffness and damping in the longitudinal direction at abutments) cannot be identified accurately. So, we remove these two parameters from verification and application results presented in this chapter. In summary, the updating parameters are 1, 3, 4, 5, 33, and 34.

Table 7-2: Candidate parameters after the first sifting step.

No.	Description	No.	Description
1	Modulus of elasticity of the concrete (deck)	18	Rot. soil-found. damping about the Vert. axis (piers)
2	compressive strength of the concrete (columns)	19	Long. soil-found. stiffness (abutment)
3	Initial modulus of elasticity of the concrete (columns)	20	Long. soil-found. damping (abutment)
4	Stiffness of the bearing pad/shear key in the Tran. Dir.	21	Tran. soil-found. stiffness (abutment)
5	Stiffness of the bearing pad in the Long. Dir.	22	Tran. soil-found. damping (abutment)
6	Mass of the embankment-abutment	23	Vert. soil-found. stiffness (abutment)
7	Vert. soil-found. stiffness (piers)	24	Vert. soil-found. damping (abutment)
8	Vert. soil-found. damping (piers)	25	Rot. soil-found. stiffness about the Long. axis (abutment)
9	Long. soil-found. stiffness (piers)	26	Rot. soil-found. damping about the Long. axis (abutment)
10	Long. soil-found. damping (piers)	27	Rot. soil-found. stiffness about the Vert. axis (abutment)
11	Tran. soil-found. stiffness (piers)	28	Rot. soil-found. damping about the Vert. axis (abutment)
12	Tran. soil-found. damping (piers)	29	Far-field soil-embankment stiffness in the Long. Dir.
13	Rot. soil-found. stiffness about the Long. axis (piers)	30	Far-field soil-embank. radiation damping in the Long. Dir.
14	Rot. soil-found. damping about the Long. axis (piers)	31	Far-field soil-embank. material damping in the Long. Dir.
15	Rot. soil-found. stiffness about the Tran. axis (piers)	32	Initial stiffness of the soil-backwall in the Long. Dir.
16	Rot. soil-found. damping about the Tran. axis (piers)	33	Mass-proportional damping coefficient
17	Rot. soil-found. stiffness about the Vert. axis (piers)	34	Stiffness-proportional damping coefficient

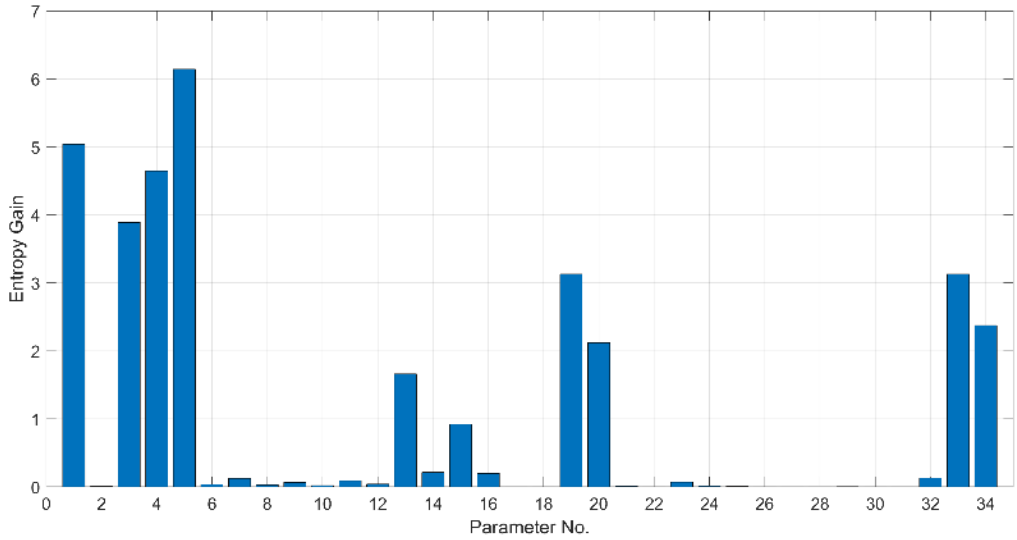

Figure 7-4: The information gain.

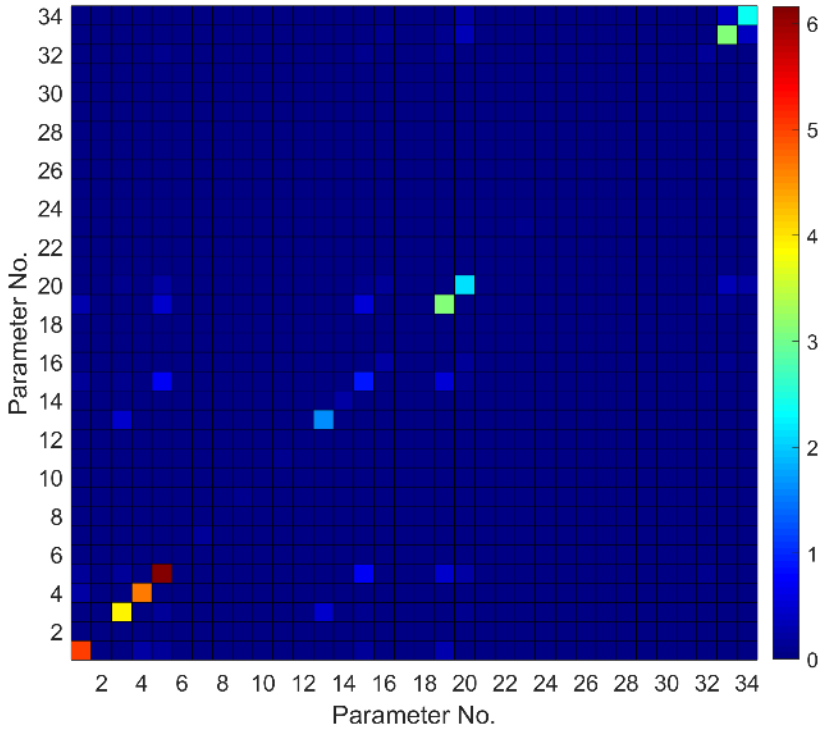

Figure 7-5: The mutual information.

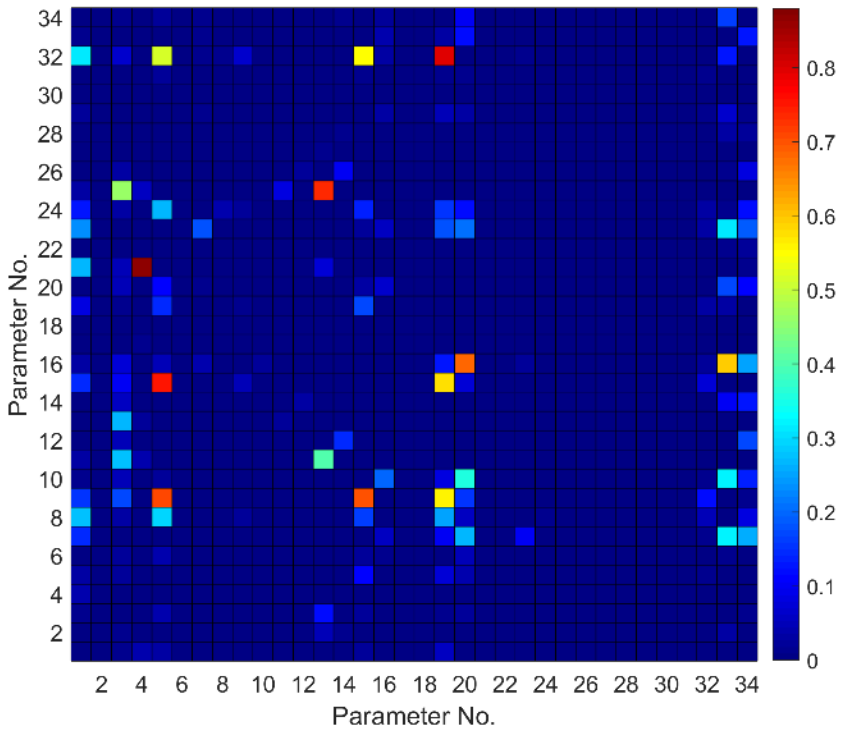

Figure 7-6: The mutual information after scaling.

7.1.2 Verification

Herein, we simulate the response of the SRC bridge under recorded FFMs (after properly projecting motions into transverse and longitudinal directions) and use the developed identification to estimate 6 unknown parameters and FIMs using response signals recorded exactly at the locations which are instrumented in the real case (see Figure 7-2). However, as there is only 1 vertical sensor, which is located at the middle of the bridge, and as we are going to analyze several real earthquake data sets, we remove Channel 7 from measurements and consequently remove vertical excitation from the problem, which is fairly decoupled from other two directions. Also, to reduce the computational cost, we estimate FIMs up to 10 Hz by properly lowpass filtering measured and predicted response signals. Note that the nonlinear time history analyses during the updating process are still carried out at the original sampling rate to maintain the needed accuracy.

We carried out the identification with assuming a 20% initial error of the unknown parameters. Figure 7-7 shows a comparison between recorded (synthetically simulated) and predicted responses at channels 4, 5, 6, 8, and 9. As seen, except for the beginning time instants of the signals in the transverse direction, the prediction is perfect. At the beginning of the estimation, both updating parameters and input motions are inaccurate. By moving to the end of the data, both parameters and input motions are identified very accurately, but the input motions identified at the very beginning are not updated anymore, so the predicted response at the end would have some error at its beginning. While it is possible to repeat the identification

with the identified parameters and obtain accurate inputs and consequently perfect response prediction, we keep the results as to show what results would like if the algorithm used in nearly online.

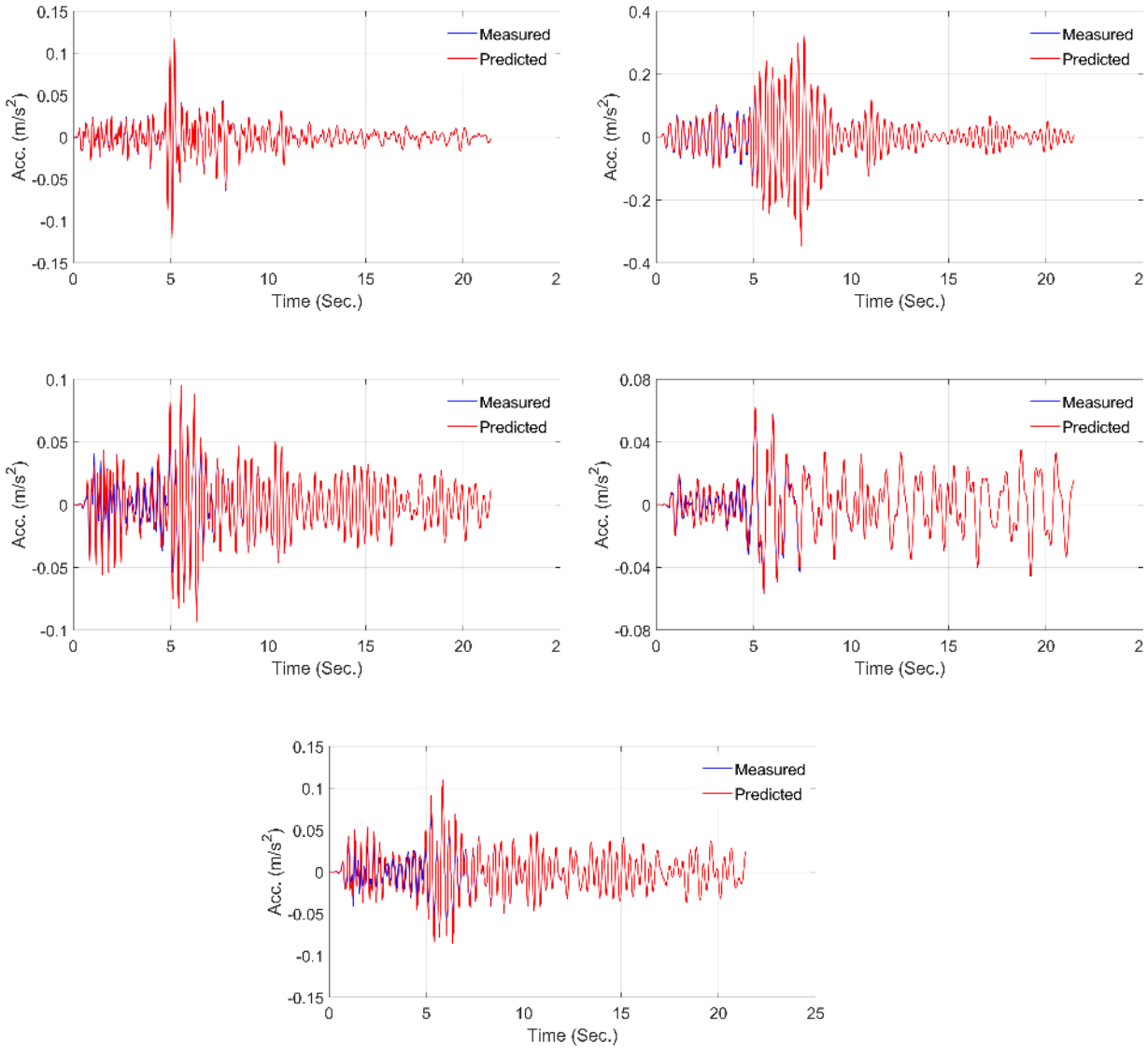

Figure 7-7: Comparison between measured and predicted responses at channels 4 (top-left), 5 (top-right), 6 (mid-left), 8 (mid-right), and 9 (bottom).

To verify the statement made above, the error of the parameters at the end of time windows is shown in Figure 7-8. As seen, at the first 5 seconds, the parameters are still inaccurate although concrete's modulus of elasticity of deck and columns converge very quickly to their true values. Based on this fact, the estimated FIMs, which are compared to their exact time histories in Figure 7-9, are inaccurate (especially in the transverse direction) at their beginning time instants.

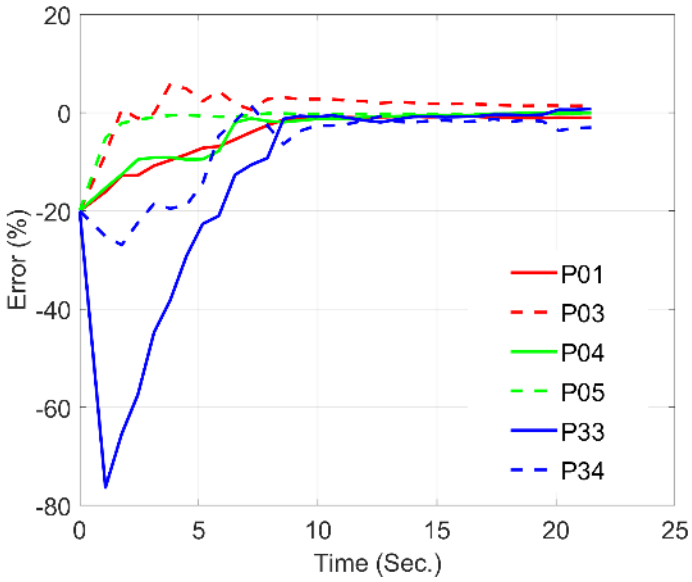

Figure 7-8: The relative error of the parameters in time.

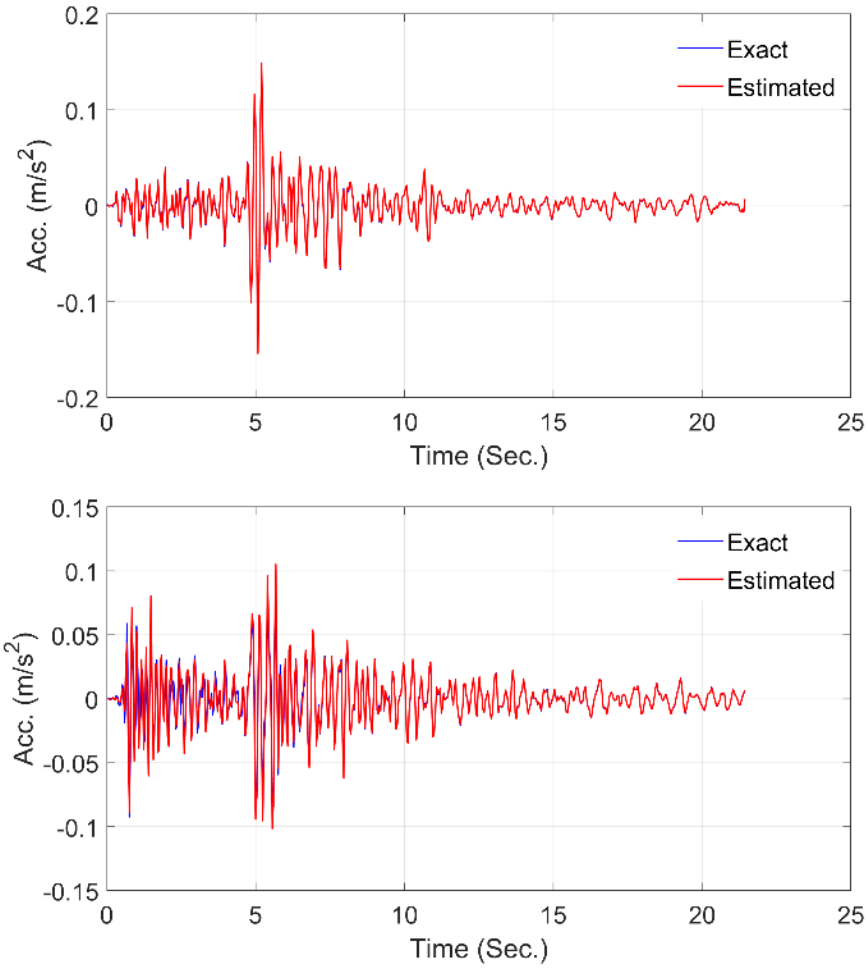

Figure 7-9: Comparison between exact and estimated longitudinal (top) and transverse (bottom) FIMs.

7.1.3 Real Data

In this section, the SRC bridge model is used along with real earthquake data sets (Table 7-1) to identify six unknown parameters specified in the identifiability section and two FIMs. Similar to the verification study of the previous section, FIMs are estimated in the frequency band 0-10 Hz and vertical FIM and Channel 7 are excluded from the analysis. All recorded signals by the SRC bridge is shown in Figure 7-10 in which channels used for the identification are specified by red rectangles. As shown in this figure, only the significant portion of the signals are used for the identification. Also, the noise variance used within the identification framework is estimated using pre-event memory of the signals.

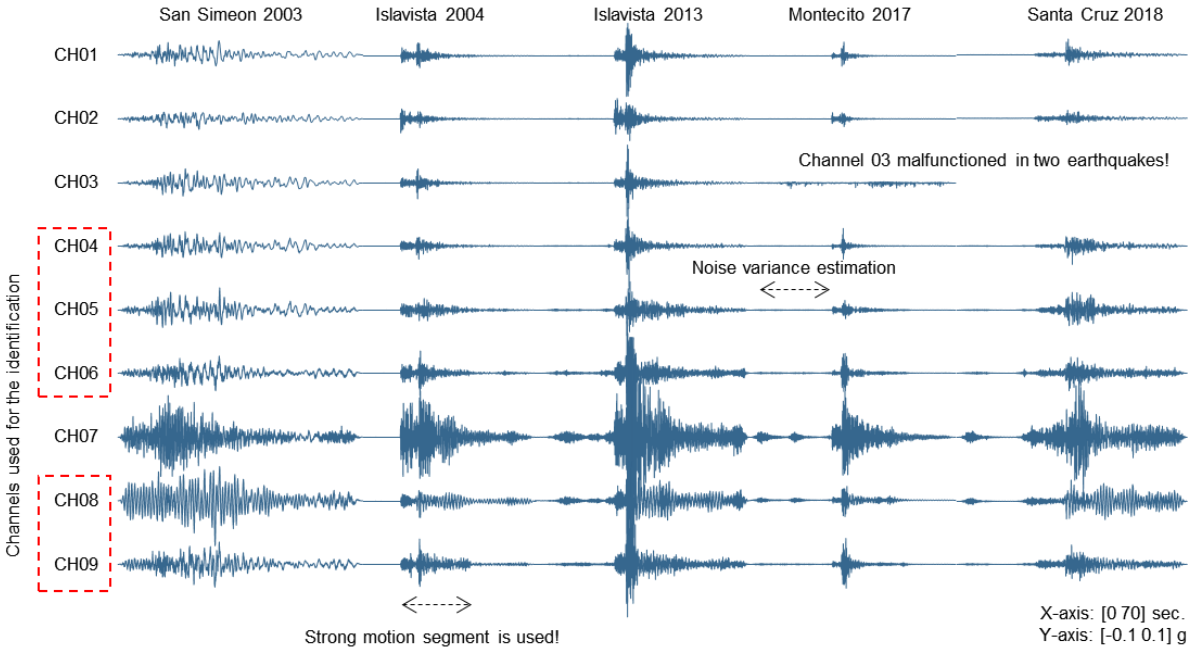

Figure 7-10: Recorded signals at SRC bridge.

Figure 7-11 to Figure 7-15 show the comparison between recorded acceleration responses and predicted ones at the end of the updating process. As mentioned earlier, we selected the significant portion of the data, which has a high signal to noise ratio, for the identification analysis. The only exemption is the San Simeon 2003 earthquake which is too long (due to the long distance from the earthquake source) and we stopped the analysis after 30 seconds. Considering the fact that these are real-life data, the similarity between recorded and prediction is very high. That is, the updated model is capable to predict the response of the SRC bridge.

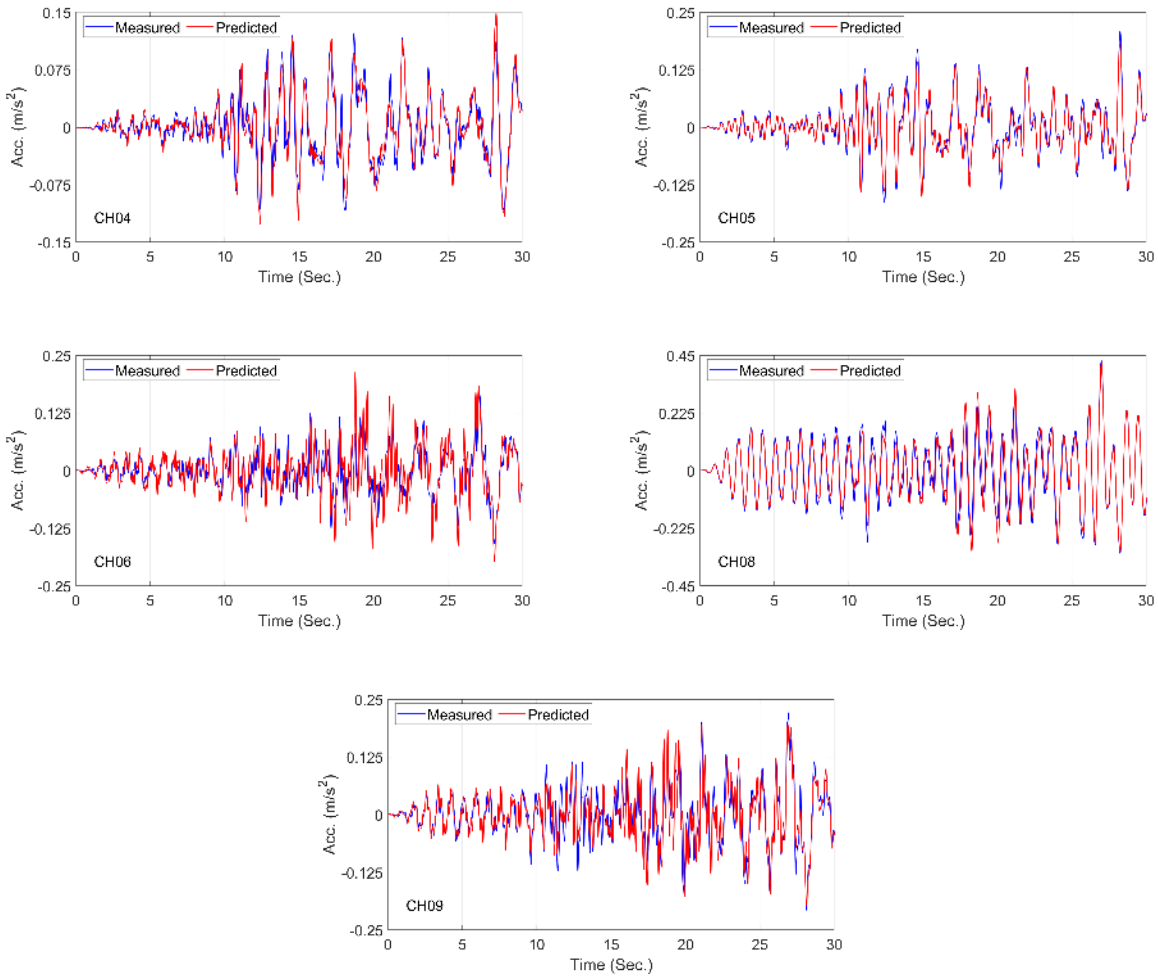

Figure 7-11: Comparison between recorded and predicted responses in San Simeon 2003 earthquake.

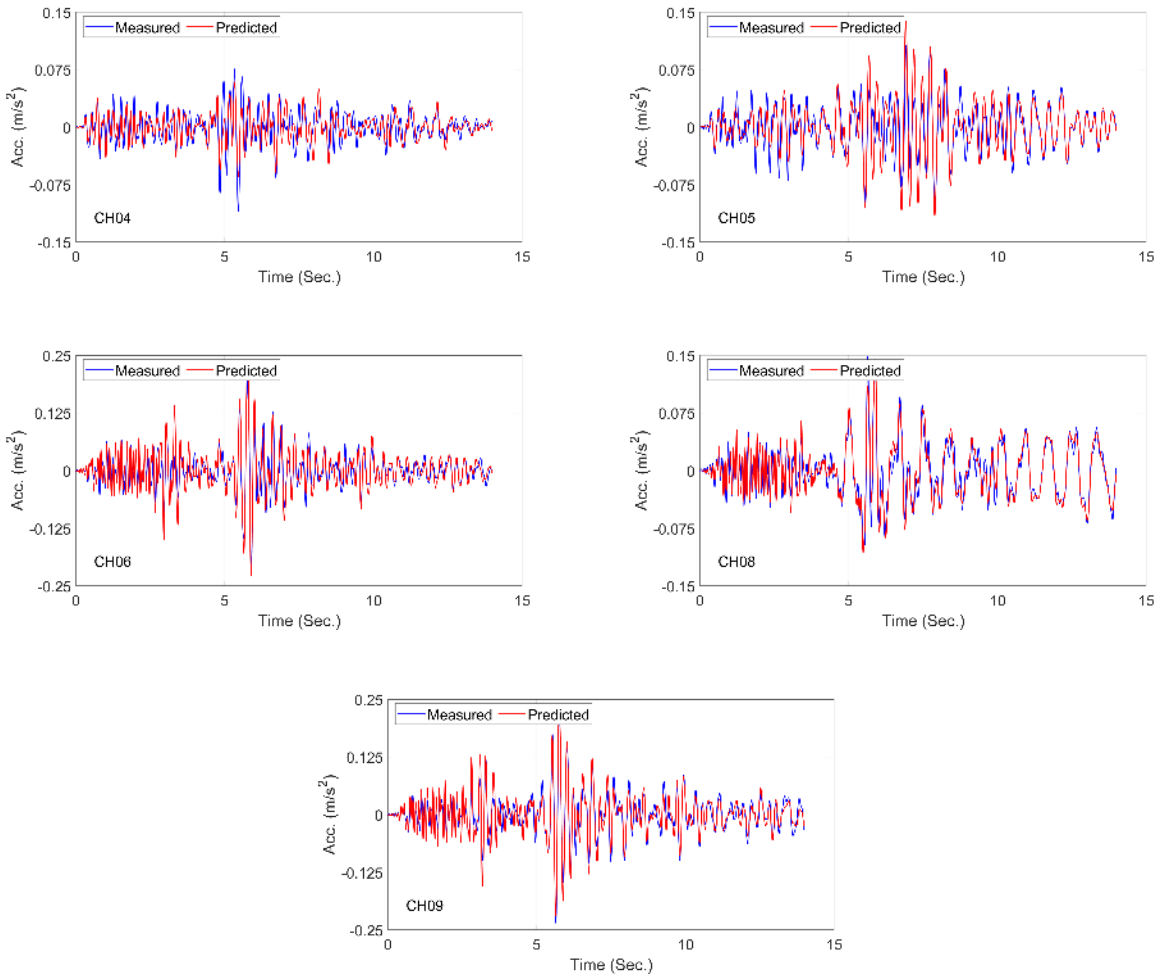

Figure 7-12: Comparison between recorded and predicted responses in Isla Vista 2004 earthquake.

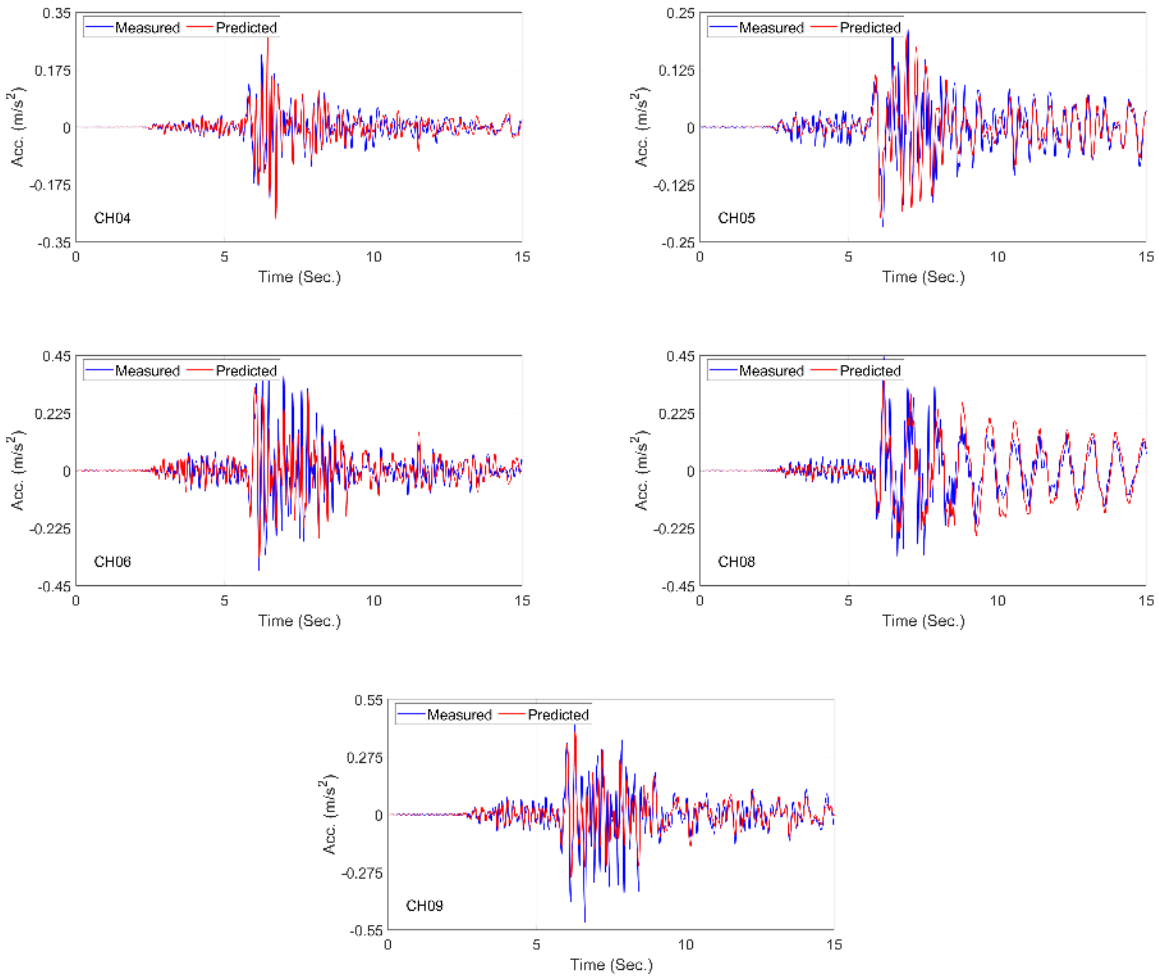

Figure 7-13: Comparison between recorded and predicted responses in Isla Vista 2013 earthquake.

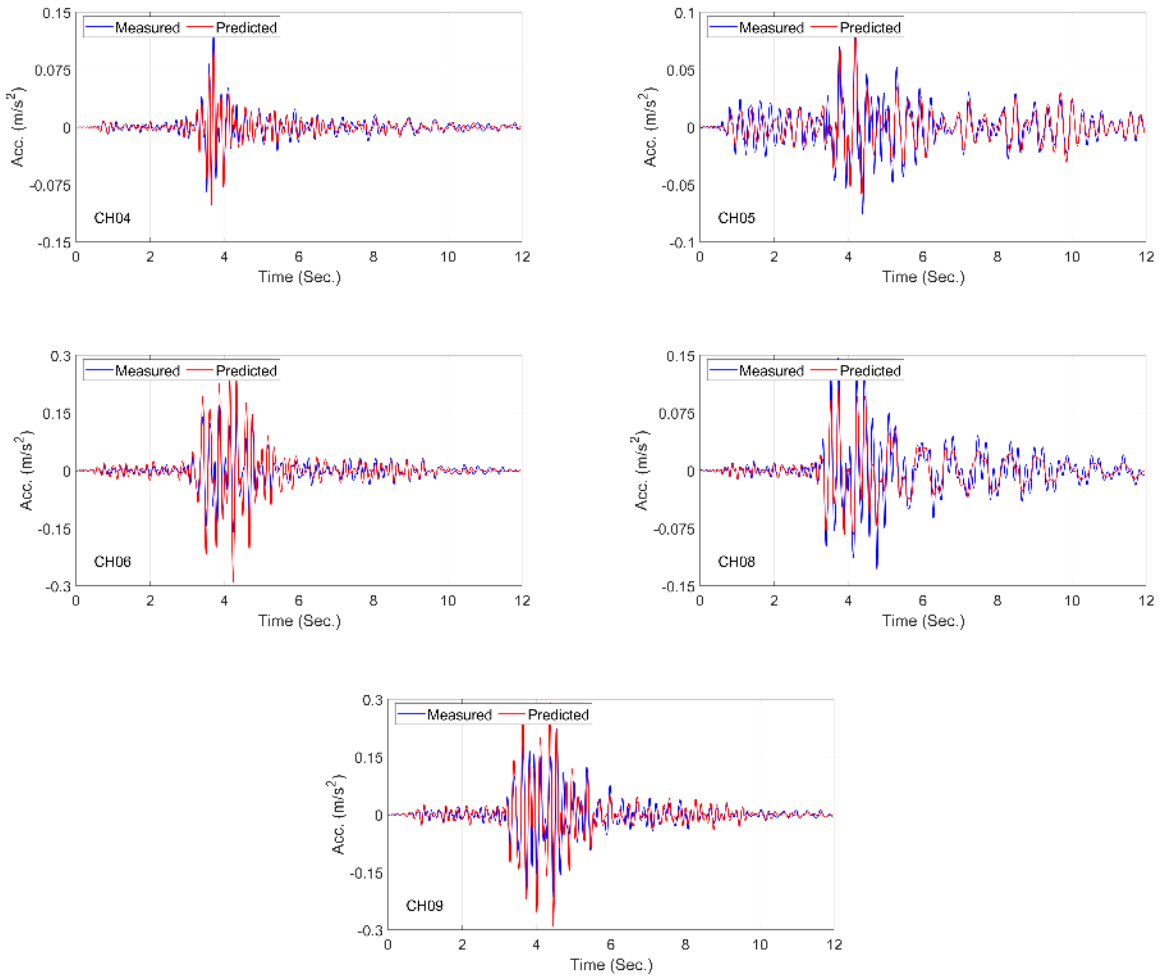

Figure 7-14: Comparison between recorded and predicted responses in Montecito 2017 earthquake.

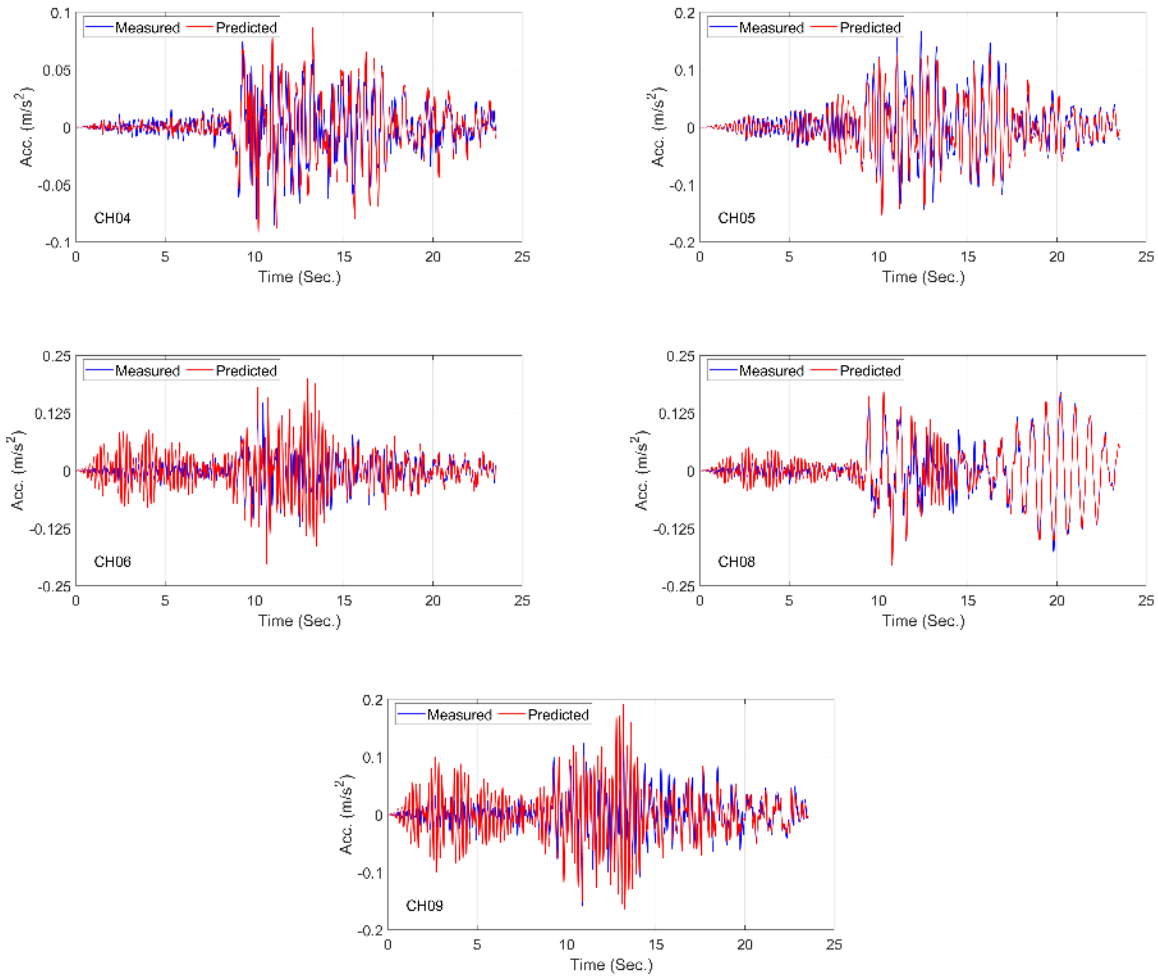

Figure 7-15: Comparison between recorded and predicted responses in Santa Cruz 2018 earthquake.

The identification process was carried out with Rayleigh damping using initial stiffness matrix, because we are trying to estimate inherent damping which can be used along with other sources of damping (e.g., nonlinearity), and can be set regardless of the earthquake intensity or nonlinear properties of the model. We tested to see how the results would be different if the current stiffness matrix at each time instant is used to calculate Rayleigh damping. As an example, Figure 7-16 shows a comparison between recorded and predicted responses at Channel 5 in Isla Vista 2004 earthquake with initial and current stiffness. As seen, because the identification is carried out sequentially, the prediction at strong shaking part of the signal is better with initial stiffness Rayleigh damping (Figure 7-16a). When using current stiffness matrix in damping estimation, the estimated stiffness-proportional damping factor decreases in the tail (low-level excitation) of the responses which reduces damping level for the strong part too, which is not involved in the updating process. So, the response is underestimated as seen in Figure 7-16(b). It is important to keep in mind that neither initial stiffness nor current stiffness matrices are perfect for damping estimation, because Rayleigh damping is itself just a modeling assumption. However, the initial-stiffness model helps

us to exclude errors in nonlinear modeling from inherent damping. Also, as discussed earlier, it provides more accurate response prediction when using within sequential updating method.

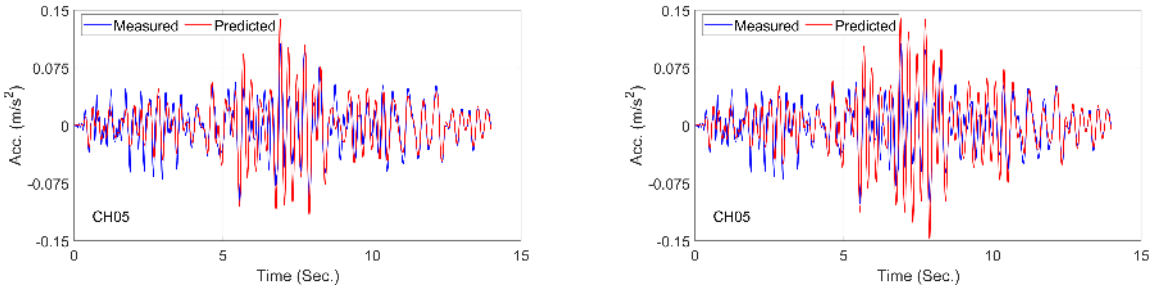

(a) initial stiffness (b) current stifffness

Figure 7-16: Comparison between recorded and predicted responses in Isla Vista 2004 earthquake with two different Rayleigh damping.

The comparison between the estimated FIMs in longitudinal and transverse directions is shown in Figure 7-17. Note that as we Channel 3 malfunctioned during 2017 Montecito and 2018 Santa Cruz earthquakes, we used Channel 4 for the recorded FFM in the longitudinal direction and Channel 1 for the transverse direction (without any projection). As seen, the estimated FIMs are almost identical to the recorded FFMs in the San Simeon earthquake 2003, because the source of the earthquake is far from the SRC bridge (~187 km), so the high-frequency components are filtered out and low-frequency components move the region including the bridge. Looking at the two last earthquakes for which identified longitudinal FIM is compared with Channel 4 shows that there is no significant bridge-abutment interaction, so what is recorded by Channel 4 could be used as input excitation at least for low-intensity ground motions. Identified longitudinal FIMs in other earthquakes show high similarity to the recorded FFM. Therefore, neither kinematic interaction nor inertial interaction is significant for this bridge under such ground motion intensities and in the longitudinal direction, while, a higher level of differences are observed between recorded FFMs and identified FIMs in the transverse direction. In addition to SSI effects, one source of this discrepancy could be due to the spatial variability of the input motions. The bridge is much more flexible in the transverse direction rather than the longitudinal direction, so minor variation in the input excitations at different piers could affect the response. So the estimated FIM shows significant difference with respect to the FFM.

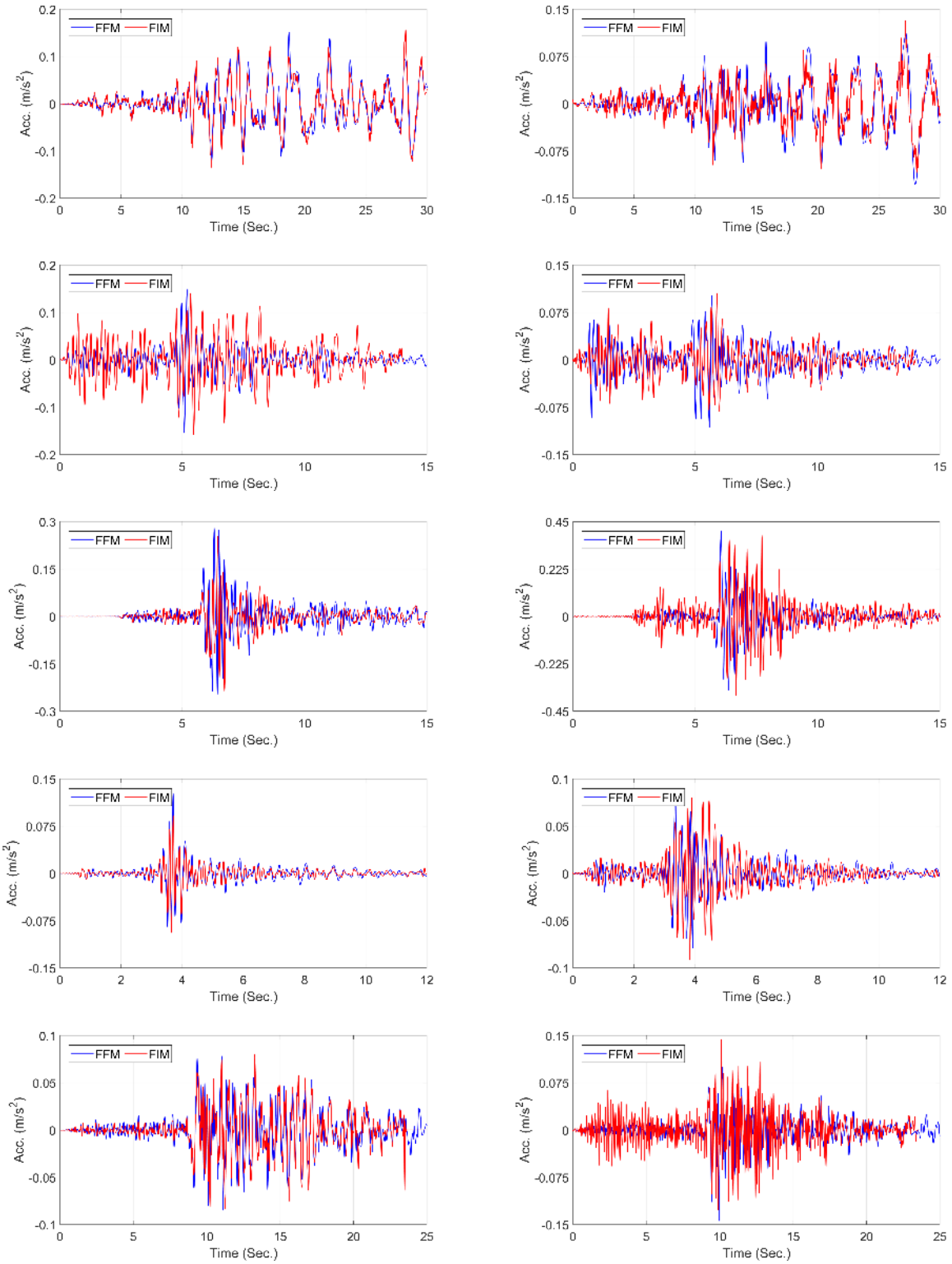

Figure 7-17: Comparison between FFM and estimated FIMs in longitudinal (left) and transverse (right) directions.

While the main purpose of this project is to estimate inherent damping, we were able to identify other sources of uncertainties in FE modeling. Parameters 1 and 3 are concrete's modulus of elasticity used for the deck, and columns, respectively, and are identified from real-life data. Herein, we show the average value of these two parameters for all 5 earthquakes so that we can see the amplitude dependency, because their correlation could mask amplitude dependency. Figure 7-18 shows these parameters for earthquakes which are sorted chronologically. The initial value taken from as-built structural drawings is shown in red dashed line. While the identified values are close to the assumed value, there is an inter-event variation. As seen, the value obtained from Isla Vista 2013 earthquake shows the lowest values, which makes sense as it is the strongest earthquake.

The identified elastomeric pad's shear stiffnesses are shown in Figure 7-19. As seen, the level of the identified values in the transverse direction is higher than the longitudinal direction. This is expected, because the deck is more constrained in this direction. Indeed, we considered a single parameter representing the combined effects of the pad, shear key, and materials filled between the deck and the shear key. The level of the identified values is close in different earthquakes with an exception which is the 2018 Santa Cruz earthquake. Probably, the deck stayed fully constrained in this earthquake, so the identified value is showing infinite pad's stiffness.

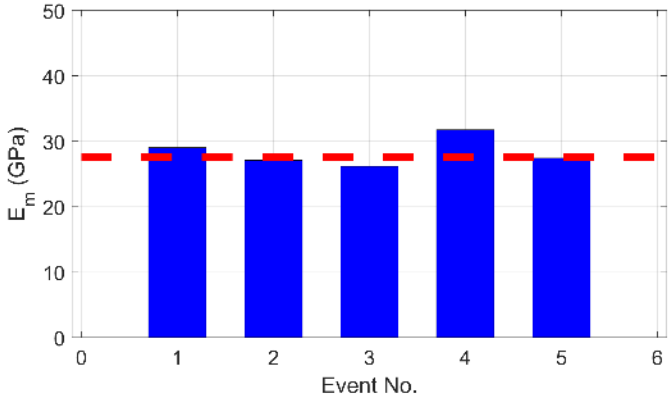

Figure 7-18: Mean value of the concrete's modulus of elasticity.

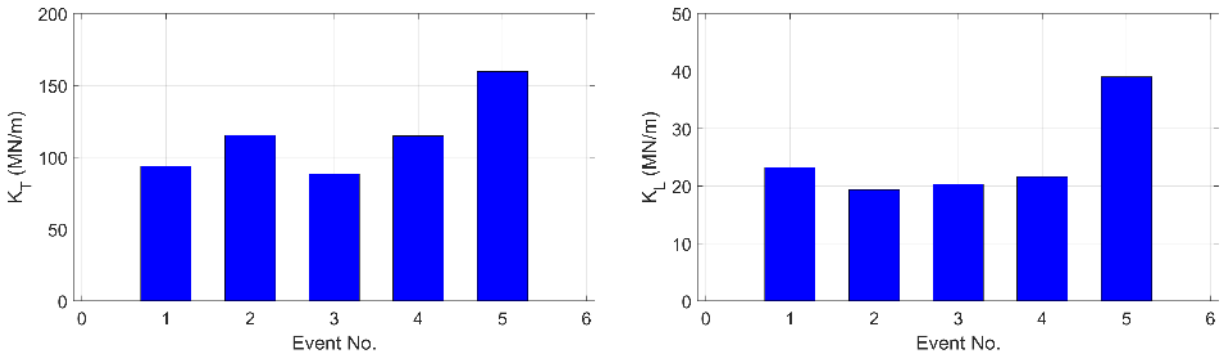

Figure 7-19: Stiffness of the elastomeric pad.

Finally, we present the identified inherent damping. Instead of presetting Rayleigh damping factors, we present the modal damping ratio in Figure 7-20. As seen, the SRC bridge shows almost zero damping in the first earthquake, i.e., San Simeon 2003 earthquake, because the bridge behaves almost quasi statically due to the absence of high-frequency components in the excitation. The identified damping from the Isla Vista 2013 earthquake clearly shows that the inherent damping is still a function of earthquake intensity! Also, this earthquake shows that 5% Rayleigh damping model for the first and last (significant) modes in low to the moderate earthquake is suitable. However, under weak excitation, much lower damping around 2% values should be considered.

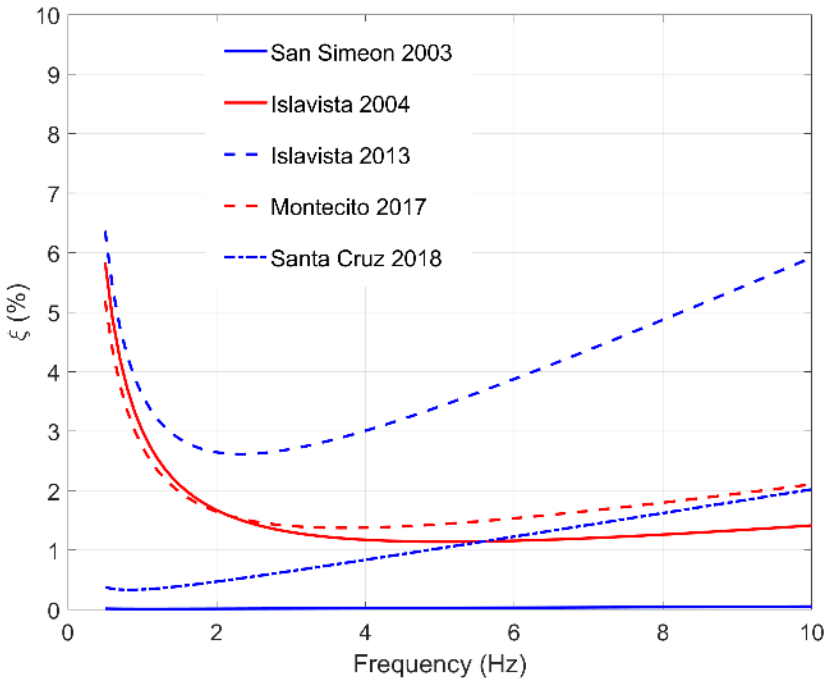

Figure 7-20: Identified Rayleigh damping model.

7.2. THE UNION MILLS BRIDGE

The Union Mills Bridge (UMB), which is also called Truckee River Bridge, is the second bridge studied in this chapter. The UMB (Figure 7-21) is located in California and is a part of the freeway 80, which connects Sacramento CA to the Reno NV. It is a continuous concrete box girder bridge with two concrete piers (one column per pier). Columns are I-shaped in the upper portion and rectangular in the lower segment. The bridge has spread footings supporting the piers and seat type abutments at its two ends. The UMB was instrumented in 1995 (6 years after its construction) under the interagency agreement between Caltrans and DOC. As shown in Figure 7-22, there are five accelerometers on the bridge and three at a nearby free-field station. Three sensors out of six accelerometers measure the response of the deck in the transverse direction, and two other accelerometers recording the longitudinal response of the deck, especially to check if the deck hits the abutment backwall.

Figure 7-21: The UMB bridge.

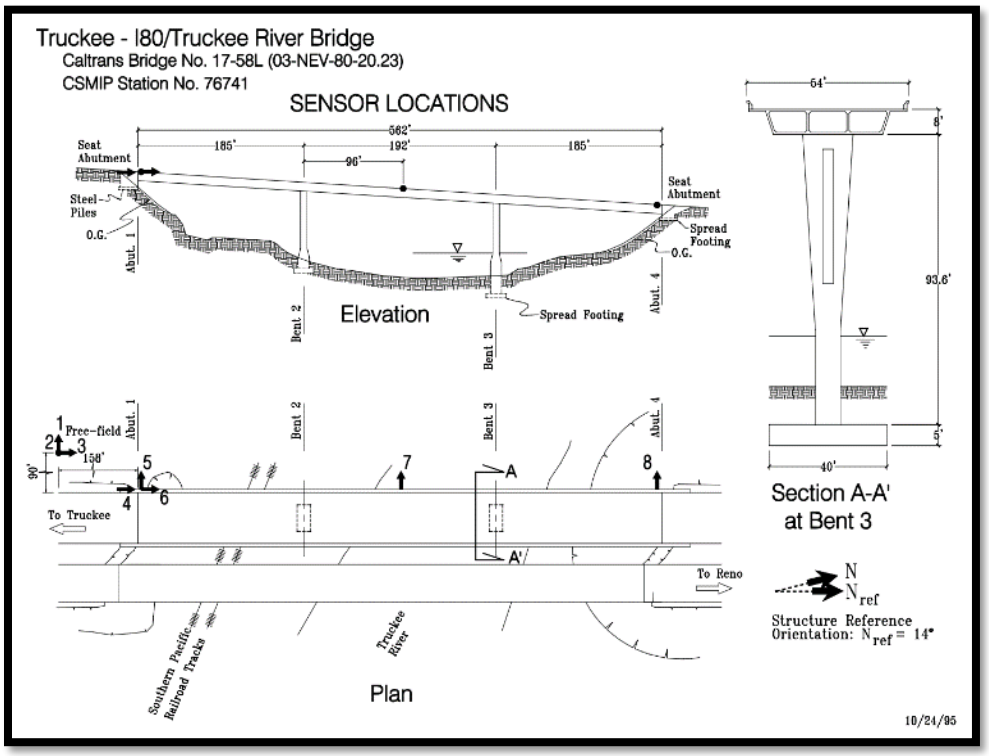

Figure 7-22: The UMB bridge instrumentation layout.

The UMB is structurally very similar to the SRC, which was described in very details in the last section. So, we skip presenting details of the structural model created in Opensees.

Since its instrumentation, the UMB bridge has recorded four earthquakes whose data is publicly available in CESMD. These earthquakes are listed in Table 7-1 along with their date, distance to the UMB bridge, and the PGA and PSA at the UMB site. All these real earthquake data will be analyzed here. It is important to mention that not all channels data is available. FFM channels (channels 1, 2, and 3) are not available in the Truckee earthquake. Also, Channel 8 is unavailable in events 1 to 3.

Table 7-3: Earthquakes recorded by the UMB bridge.

No.	Earthquake	Date	Distance (km)	PGA (g)	PSA (g)
1	King Beach	06/03/2004	10.1	0.032	0.054
2	Tahoe Vista	06/26/2005	7.6	0.189	0.273
3	White Hawk	10/26/2011	40.0	0.037	0.090
4	Truckee	06/27/2017	22.0	0.014	0.015

7.2.1 Identifiability

Similar to the SRC case, we first carry out an identifiability study using simulated data to find the identifiable parameters using the very limited number of sensors. The initial list of parameters is identical to the one shown in Table 7-2 for the SRC case. We carry out the identifiability analysis under Kings Beach 2004 FFM for two cases with and without channel 8, as this channel is not available for 3 out of 4 earthquakes.

To find the most identifiable parameters, the information gain is shown in Figure 7-23. As seen, there are 9 parameters which are potentially identifiable due to their high information gain with or without having channel 8. These parameters sorted in descending order are parameters No. 5, 1, 4, 3, 33, 19, 34, 15, and 20. To see the mutual information among these parameters, Figure 7-24 is shown. As seen, there is no significant mutual information among the first four dominant parameters (5, 1, 4, and 3), so they are chosen to be parameters which can be identified. However, some level of correlation is observed among other parameters. To make this existing correlation more visible, Figure 7-25, which is a scaled version of Figure 7-24, is presented. While parameters 33 and 34 have a mutual correlation with each other, we keep them because they are not dependent on other parameters can we are interested in their collective effects, i.e., inherent damping. Parameters 15 and 19 are highly correlated so one of them must be kept fixed. The normalized index of parameter 15 is much higher, so it should be removed from the updating parameters list. Parameters No. 19 and 20 are identifiable according to the carried out identifiability analysis. However, similar to the SRC case, the verification studies showed that they cannot be identified accurately. The reason is that the identifiability analysis was carried out assuming known input, while the identification is carried out in an output-only way. As the number of sensors in the longitudinal direction is very limited, the input is unknown, and there are already several parameters contributing in this direction, parameters No. 19 and

20 (respectively, the far-field soil-foundation stiffness and damping in the longitudinal direction at abutments) cannot be identified accurately. So, we remove these two parameters from verification and application results presented in this chapter. In summary, the updating parameters are 1, 3, 4, 5, 33, and 34, which are identical to the SRC bridge.

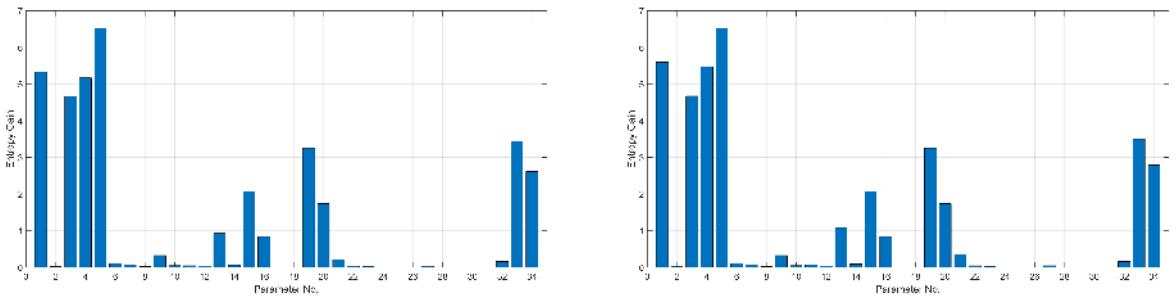

Figure 7-23: The information gain without (left) and with (right) channel 8.

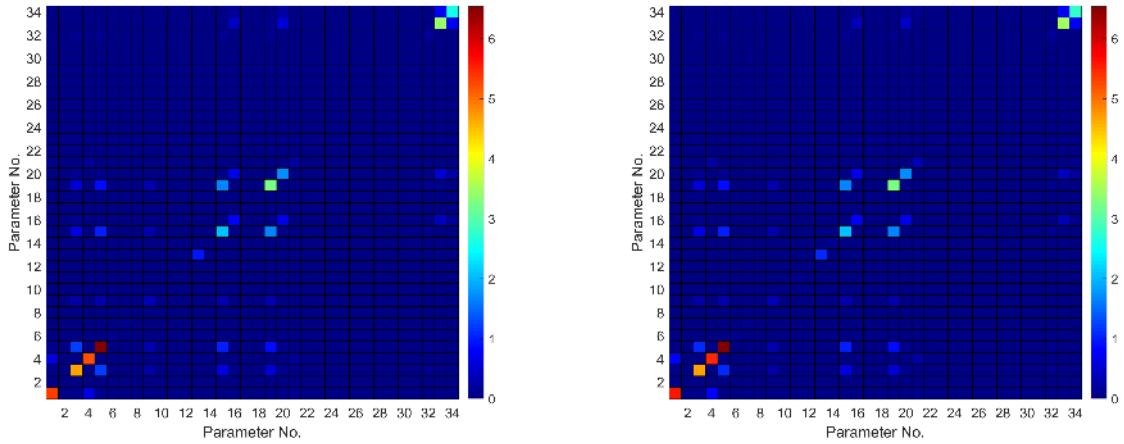

Figure 7-24: The mutual information without (left) and with (right) channel 8.

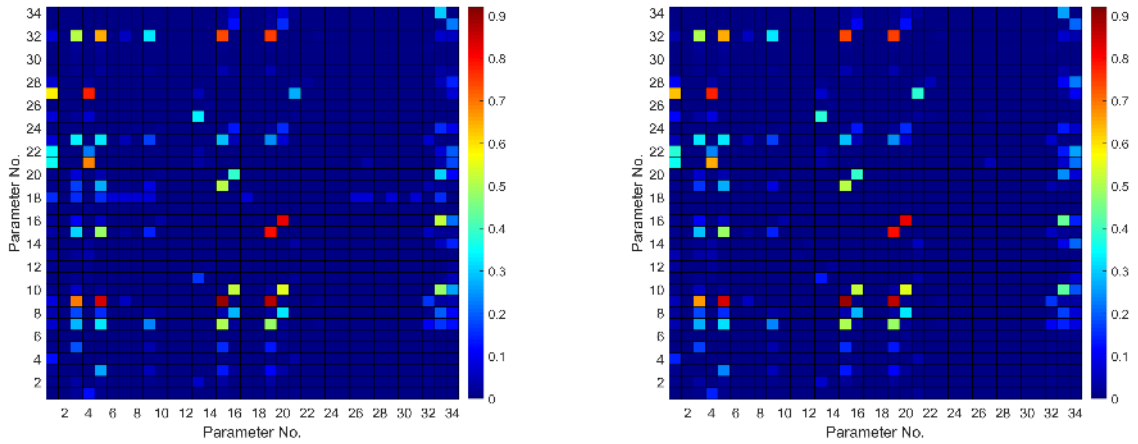

Figure 7-25: The mutual information without (left) and with (right) channel 8 after scaling.

7.2.2 Verification

Herein, we simulate the response of the SRC bridge under recorded FFMs and use the developed identification to estimate 6 unknown parameters and FIMs using response signals recorded exactly at the locations which are instrumented in the real case. Similar to the SRC case, we remove vertical excitation from the problem, which is fairly decoupled from the other two directions. Also, to reduce the computational cost, we estimate FIMs up to 10 Hz by properly lowpass filtering measured and predicted response signals. Note that the nonlinear time history analyses during the updating process are still carried out at the original sampling rate to maintain the needed accuracy.

We carried out the identification with assuming a 20% initial error of the unknown parameters. Figure 7-26 to Figure 7-29 show comparison between recorded (synthetically simulated) and predicted responses for cases with and without channel 8 and with initial stiffness or tangent stiffness proportional damping. As seen, for all four cases, the predicted responses are almost identical to the recorded responses confirming the superb performance of the method and reliability of the results obtained later using similar but real-life data.

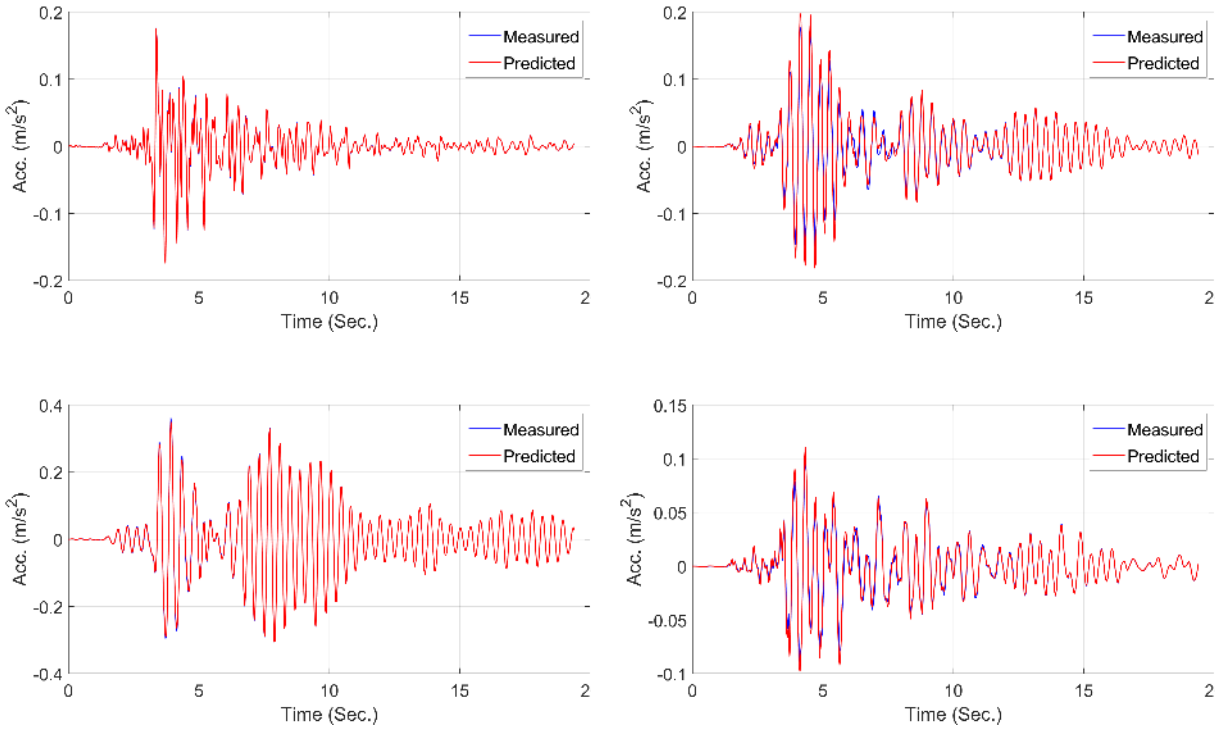

Figure 7-26: Comparison between measured and predicted responses at channels 4 (top-left), 5 (top-right), 6 (button-left), and 7 (bottom-right) using initial stiffness proportional damping.

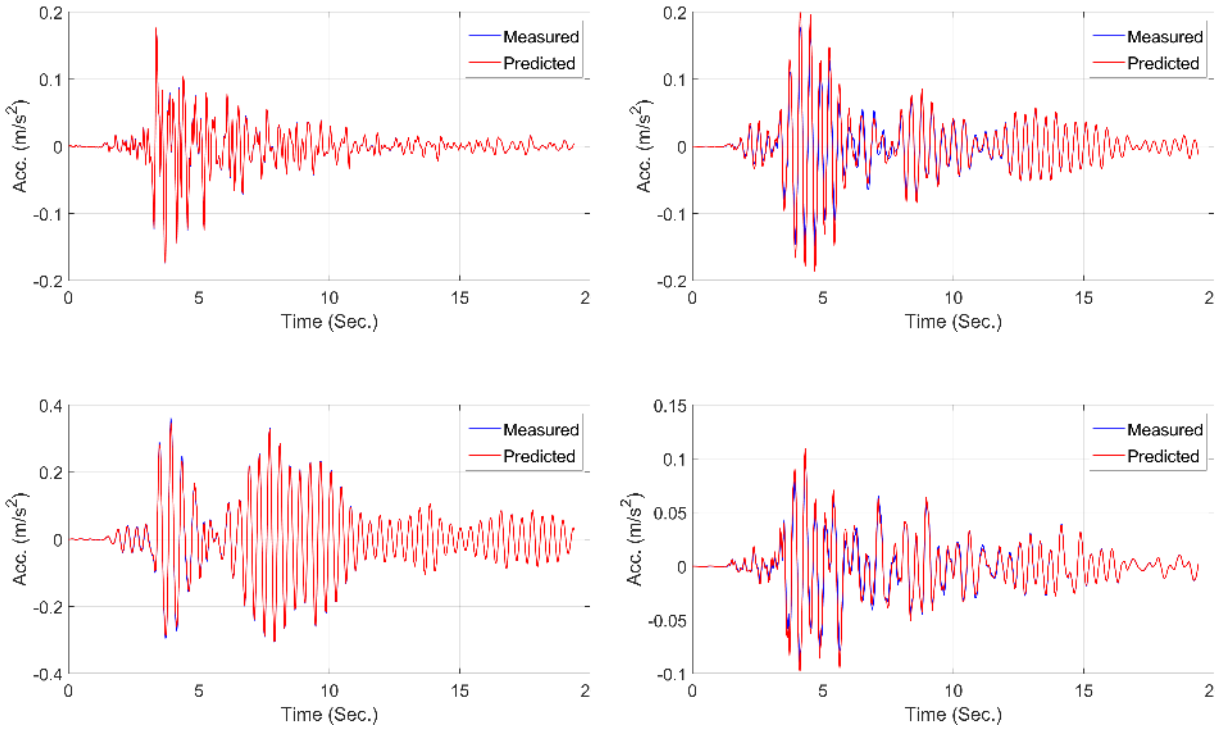

Figure 7-27: Comparison between measured and predicted responses at channels 4 (top-left), 5 (top-right), 6 (button-left), and 7 (bottom-right) using tangent stiffness proportional damping.

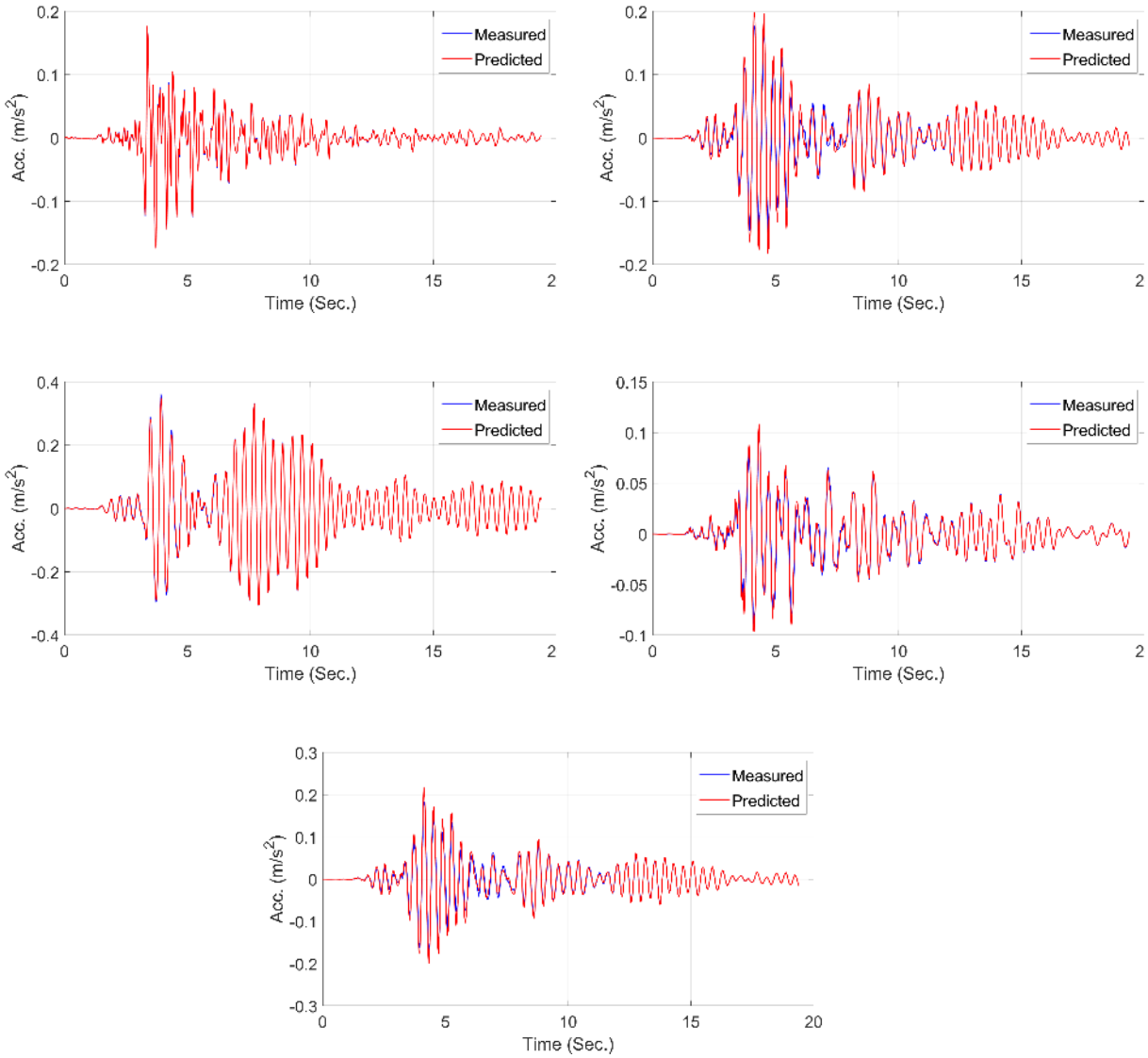

Figure 7-28: Comparison between measured and predicted responses at channels 4 (top-left), 5 (top-right), 6 (mid-left), 7 (mid-right), and 8 (bottom) using initial stiffness proportional damping.

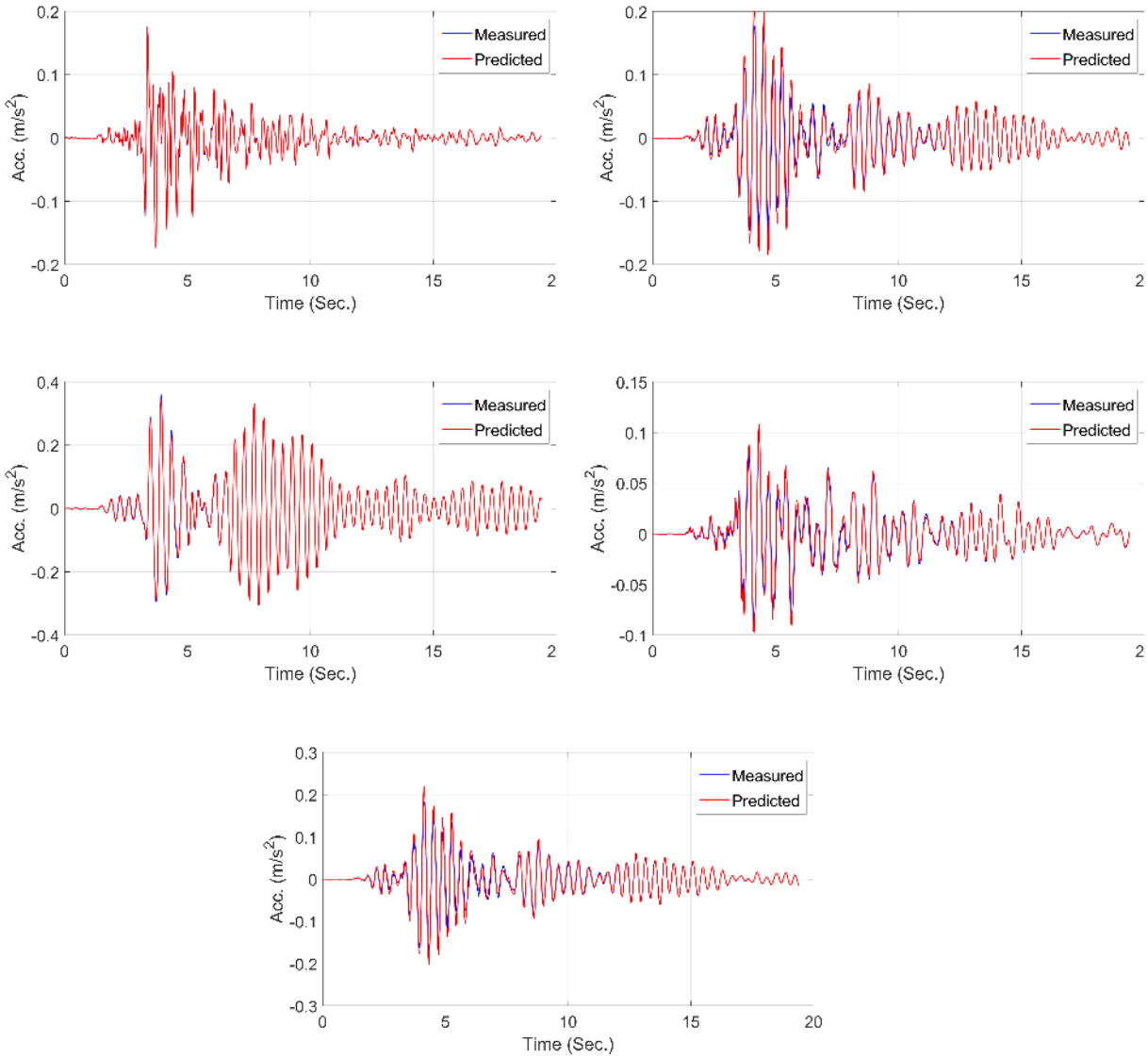

Figure 7-29: Comparison between measured and predicted responses at channels 4 (top-left), 5 (top-right), 6 (mid-left), 7 (mid-right), and 8 (bottom) using tangent stiffness proportional damping.

The time variation of the parameters during the updating process is shown in Figure 7-30 for all four cases mentioned above. As seen, there are no significant differences among these four cases; that is, the performance of the method for this bridge and under this specific input excitation and instrumentation layout is not very sensitive to the presence or absence of channel 8 or to the type of stiffness matrix used for damping calculation. This figure also shows that the identified stiffness-proportional damping factor is not as accurate as of the SRC bridge.

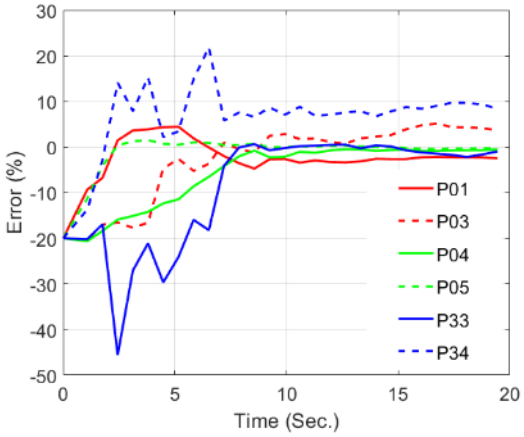

a) Initial stiffness proportional damping without channel 8

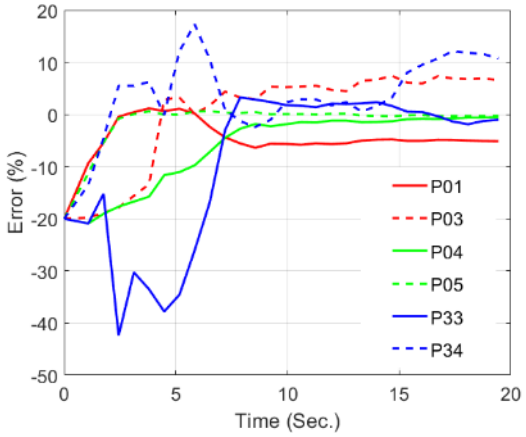

b) Initial stiffness proportional damping with channel 8

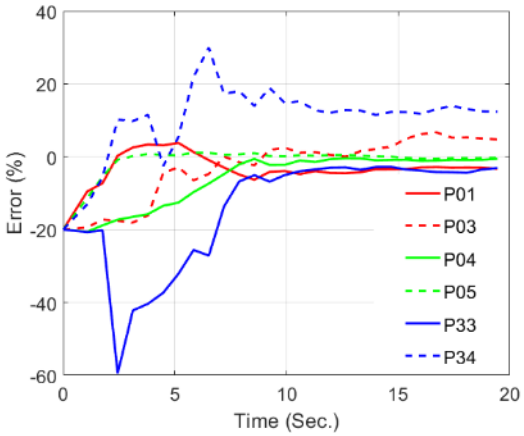

c) Tangent stiffness proportional damping without channel 8

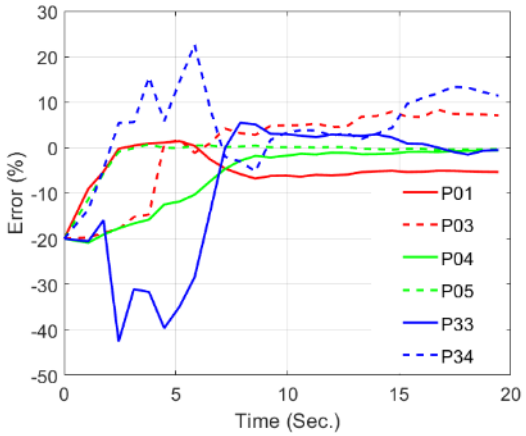

d) Tangent stiffness proportional damping with channel 8

Figure 7-30: The relative error of the parameters in time.

Finally, Figure 7-31 and Figure 7-32 show a comparison between exact and estimated FIMs in longitudinal and transverse directions, respectively. As seen, except minor differences observed in the transverse direction, the estimated FIMs for all four cases are perfect.

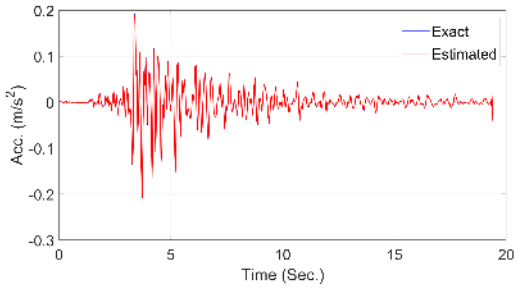

a) Initial stiffness proportional damping without channel 8

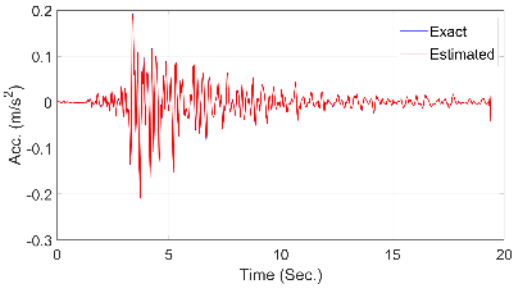

b) Initial stiffness proportional damping with channel 8

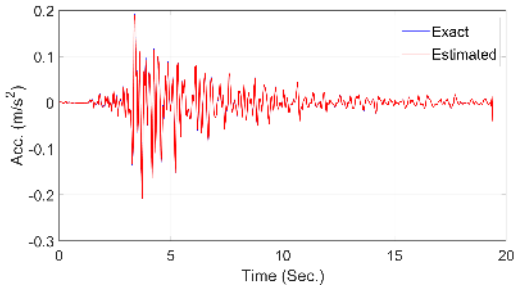

c) Tangent stiffness proportional damping without channel 8

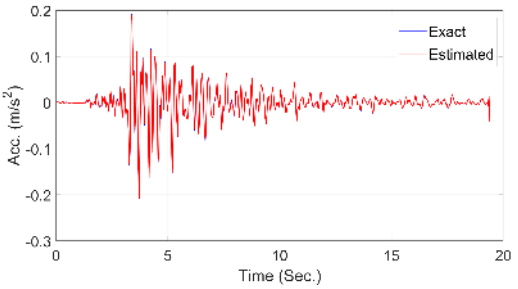

d) Tangent stiffness proportional damping with channel 8

Figure 7-31: Comparison between exact and estimated longitudinal FIMs.

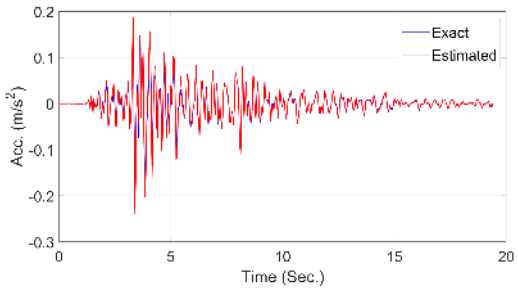

a) Initial stiffness proportional damping without channel 8

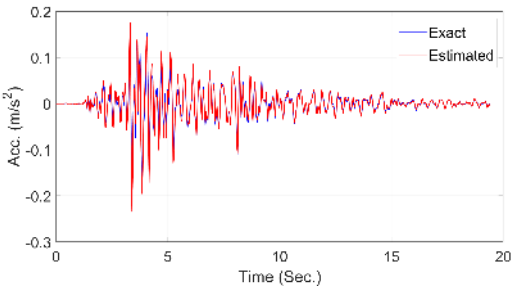

b) Initial stiffness proportional damping with channel 8

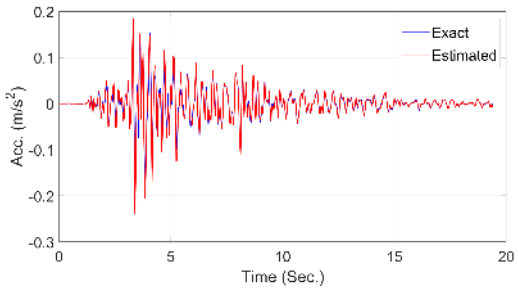

c) Tangent stiffness proportional damping without channel 8

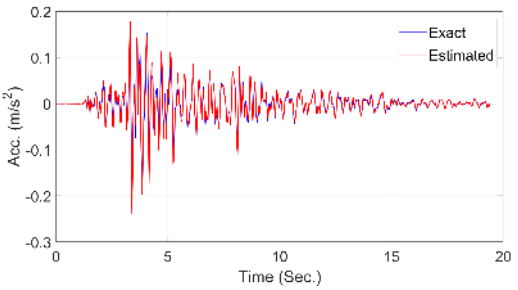

d) Tangent stiffness proportional damping with channel 8

Figure 7-32: Comparison between exact and estimated transverse FIMs.

7.2.3 Real Data

In this section, the UMB bridge model is used along with real earthquake data sets (Table 7-3) to identify six unknown parameters specified in the identifiability section and two FIMs. Similar to the verification study of the previous section, FIMs are estimated in the frequency band 0-10 Hz and vertical FIM is excluded from the analysis. We use only a significant portion of the signals as we did for the SRC bridge.

Figure 7-33 to Figure 7-36 show the comparison between recorded acceleration responses and predicted ones at the end of the updating process. As mentioned earlier, we selected a significant portion of the data, which has a high signal to noise ratio, for the identification analysis. Considering the fact that these are real-life data, the similarity between recorded and prediction is very high. That is, the updated model is capable to predict the response of the UMB bridge.

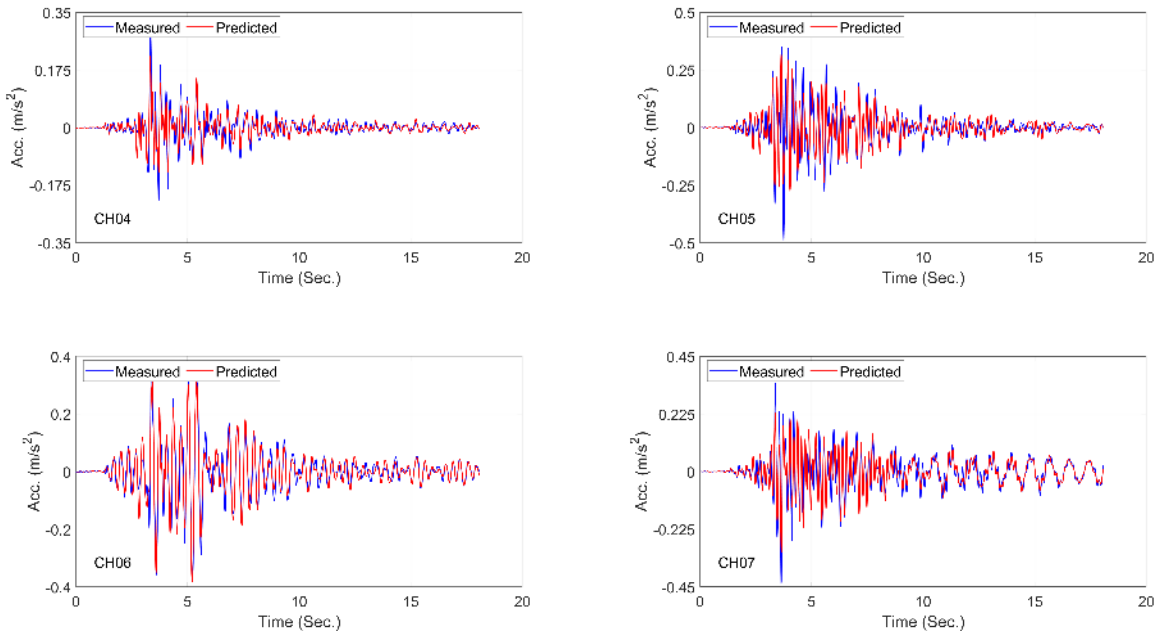

Figure 7-33: Comparison between recorded and predicted responses in Kings Beach 2004 earthquake.

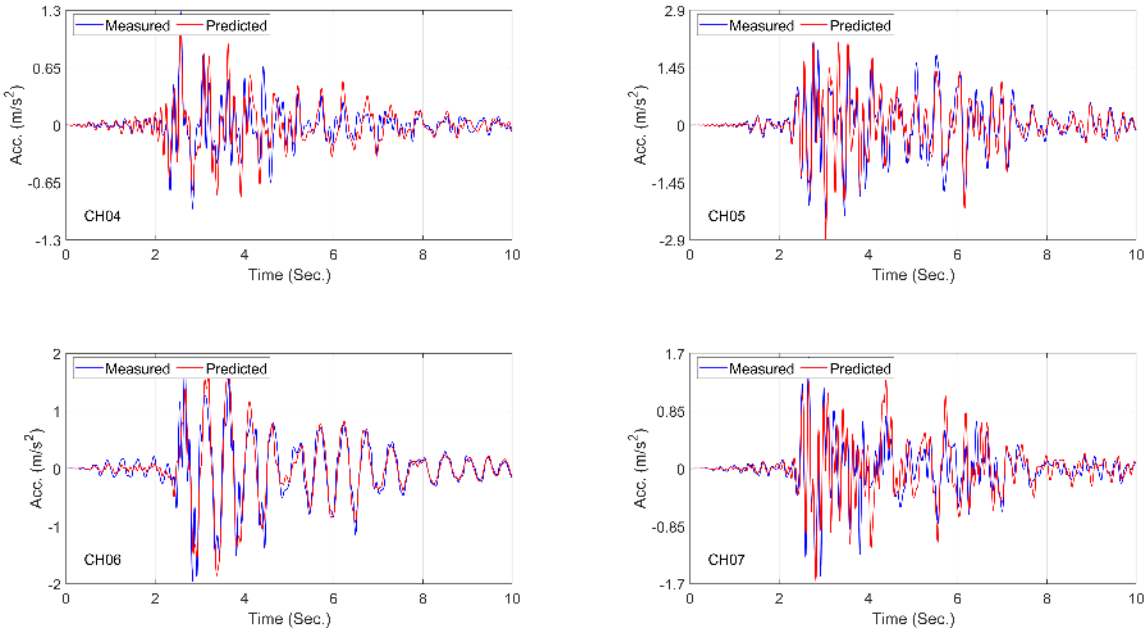

Figure 7-34: Comparison between recorded and predicted responses in Tahoe Vista 2005 earthquake.

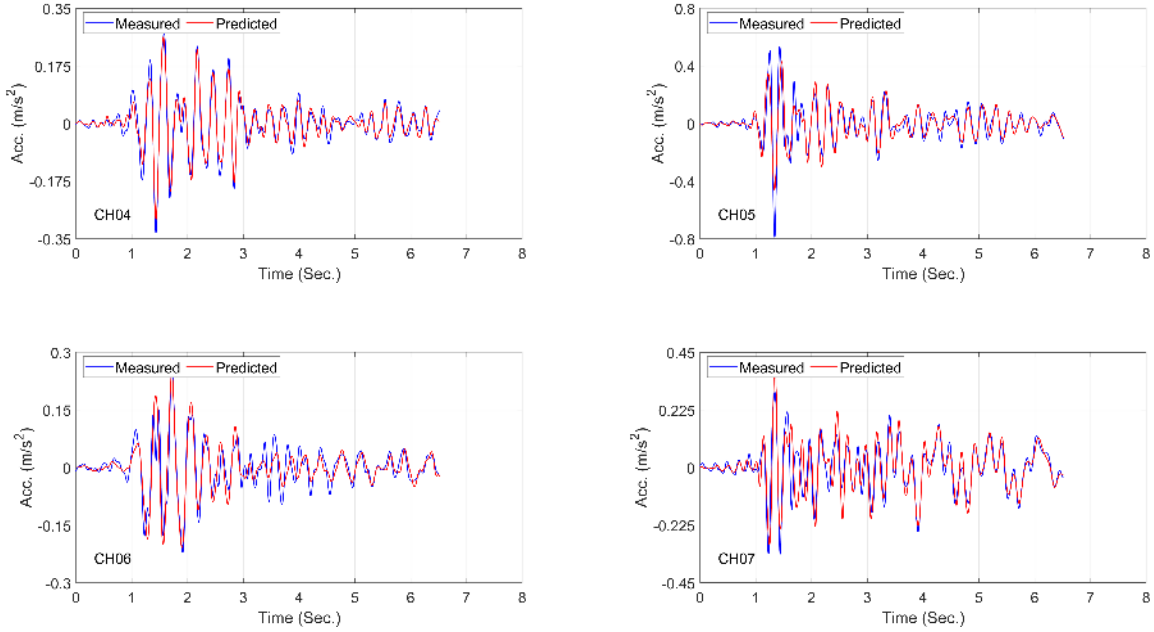

Figure 7-35: Comparison between recorded and predicted responses in White Hawk 2011 earthquake.

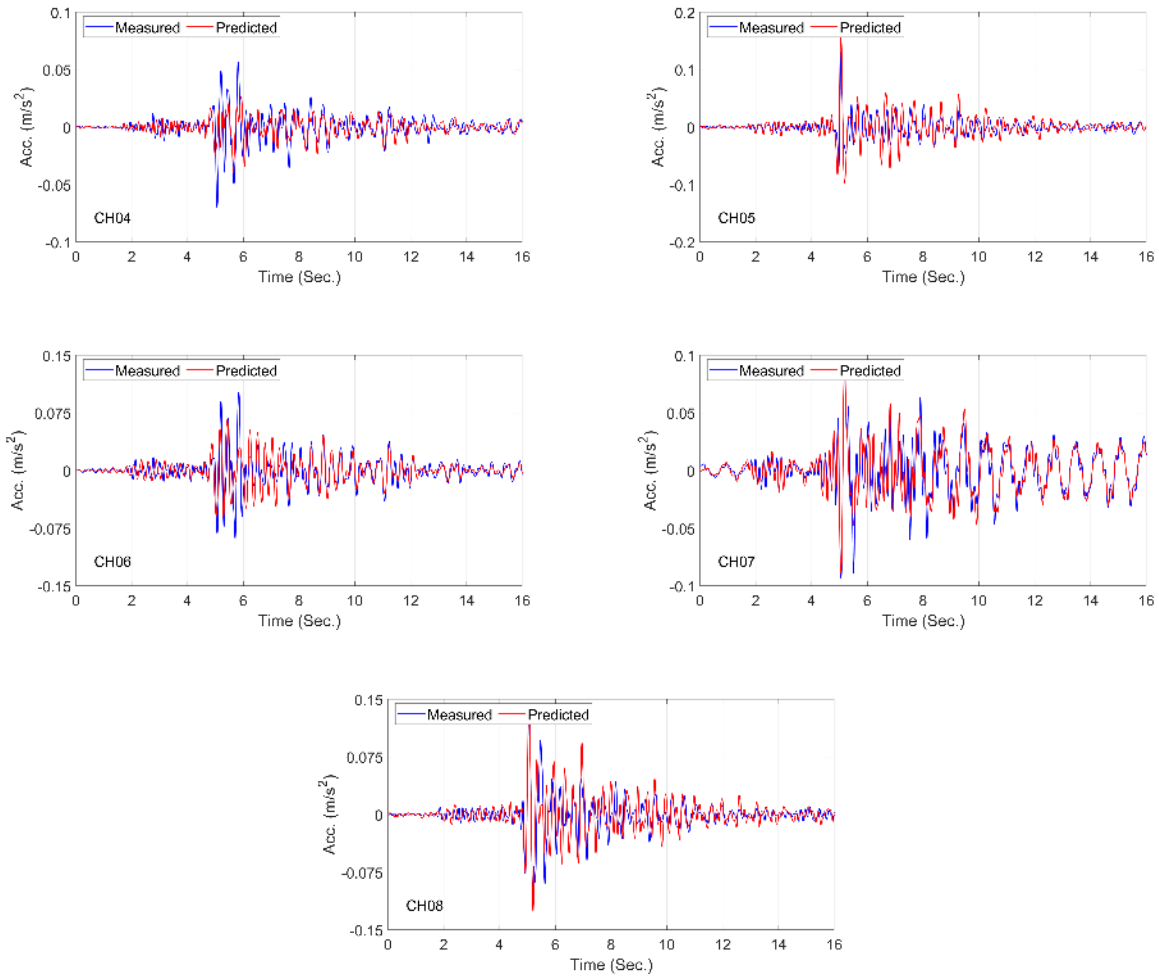

Figure 7-36: Comparison between recorded and predicted responses in Truckee 2017 earthquake.

The comparison between the estimated FIMs in longitudinal and transverse directions is shown in Figure 7-37. As seen, in the Tahoe Vista earthquake whose data is more reliable to the level of motions, the estimated FIM in the longitudinal direction is very similar to the recorded FFM. However, there is a significant discrepancy in the transverse direction. In two other earthquakes fo which FFMs are available, the estimated FIMs and recorded FFMs are more similar, while the mentioned discrepancy is still seen in the transverse direction.

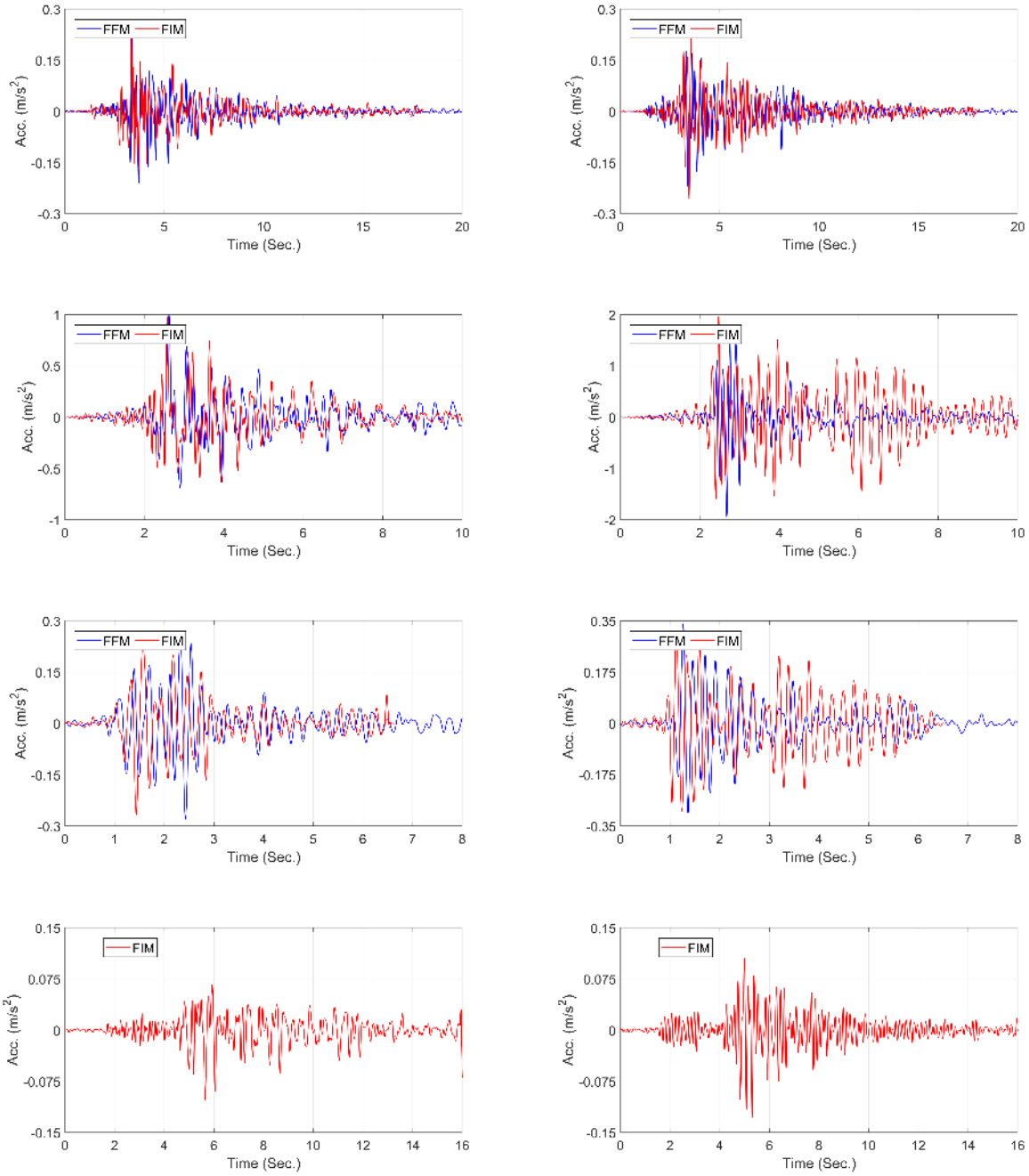

Figure 7-37: Comparison between FFM and estimated FIMs in longitudinal (left) and transverse (right) directions.

Similar to the SRC case, herein the identified parameters are shown. Figure 7-38 displays the average value of the concrete's elastic modulus. As seen, the identified values are very close to the value suggested in the as-built drawings. Results obtained for the stiffness of the bearing pads (Figure 7-39) show the same trend as seen in the SRC bridge. That is, the level of stiffnesses in the transverse direction is higher due to the contribution of the shear key.

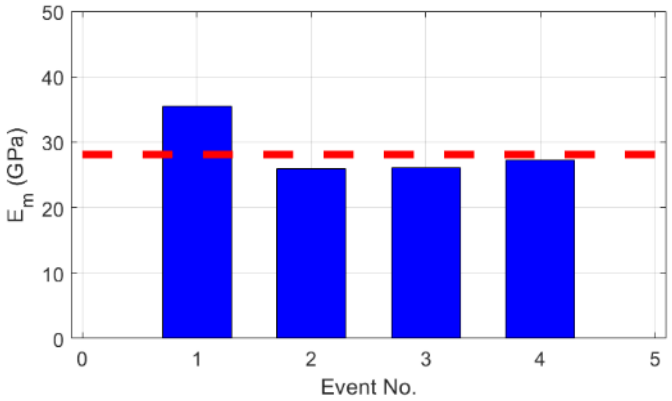

Figure 7-38: Mean value of the concrete's modulus of elasticity.

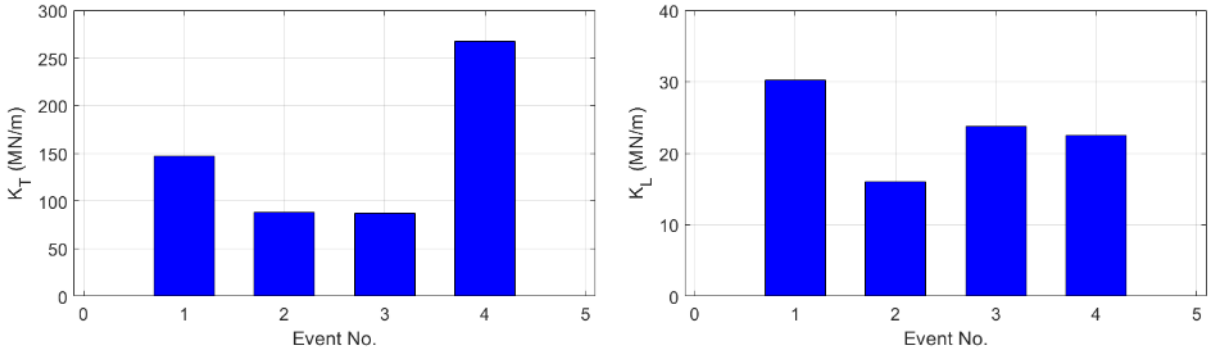

Figure 7-39: Stiffness of the elastomeric pad.

Finally, we present the identified inherent damping as the modal damping ratio in Figure 7-40. Interestingly, the behavior of the inherent damping is quite similar to what we observed in the SRC bridge. That is, the damping is a combination of mass and stiffness proportional parts in a large earthquake, i.e., Tohe Vista 2005, while it is mostly stiffness-proportional in King Beach 2004 and White Hawk 2011 earthquakes. The damping level behaves mostly mass-proportional with a low level of damping in the Truckee 2017 earthquake, which was a very weak event. So, we can conclude that the traditional 5% Rayleigh damping model for the first and last (significant) modes in low to the moderate earthquake is suitable. However, under weak excitation, much lower damping around 2% values should be considered.

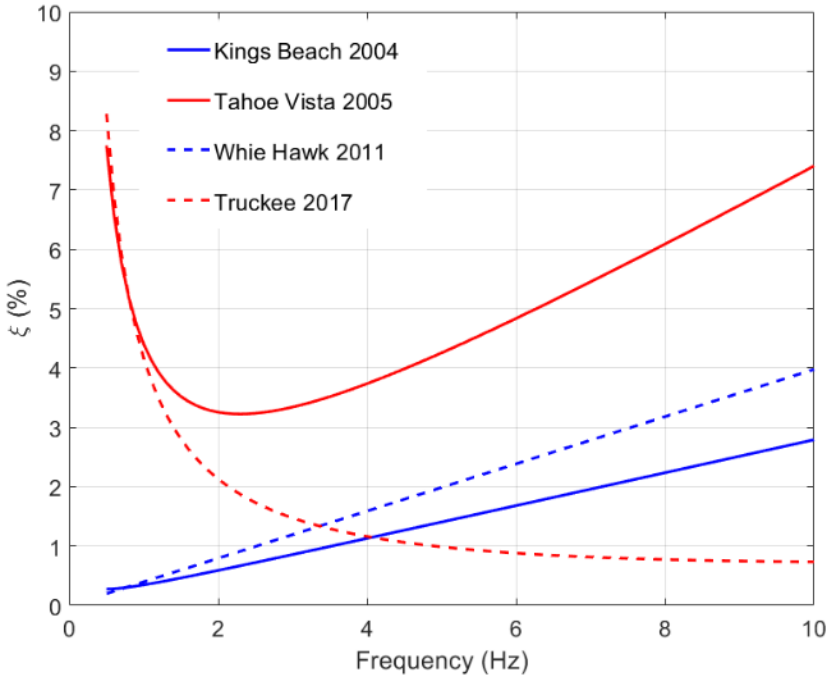

Figure 7-40: Identified Rayleigh damping model.

CHAPTER 8: CONCLUSIONS

8.1. SUMMARY

Thanks to the current development in the computational resources and advancement in structural analysis and material behavior, accurate and detailed Finite element (FE) models are easily accessible. The access to these numerical models provides an opportunity to be able to predict the response of structures, especially infrastructures like bridges which provide vital transportation links between metropolitan, industrial and agricultural regions, and their seismic performance impacts the well-being of the entire state and thus, the nation. However, while the nonlinear behaviors of most superstructure's[14] components (for example columns) and soil-foundation interaction elements can be captured relatively well with current capabilities, devising accurate models and parameter values for damping has eluded researchers and practitioners alike. We are still modeling inherent damping in our FE models based on simplified Rayleigh damping model with some prescribed values obtained from some old experimental studies because damping cannot be analytically or numerically calculated based on the structural properties. This is a simplified assumption that has worked well for decades, because structures have been designed in a compatible way. That is, classic forced-based methods have been used to design such structures where all components are being treated uniformly. With the advent of the Performance-Based Earthquake Engineering (PBEE), nonlinear time-history analyses are getting a significant role in the design and analysis of the structure. In these analyses, various sources of energy dissipation, which were used to be lumped to in a single damping term, are explcitily modeled. For example, the material can show nonlinear behavior and explicitly dissipates energy in the model, or radiation damping at the soil-structure boundaries are explicitly modeled through the discrete damper. However, as there is no way to explicitly add inherent damping of the structure, Rayleigh damping with same old and traditional values are used which may result in double counting the damping, because these values have been mostly obtained from data-driven identification methods through which all sources of damping are summed up.

In this project, we developed a model-based identification framework to identify the inherent damping from real-life earthquake response data recorded by the instrumented bridges, while other sources of energy dissipation mechanism are explicitly modeled. This method works based on the Bayesian filtering and is able to quantify uncertainties along with the identification of mean values of the uncertain parameters, e.g., damping parameters. Moreover, the method is able to work even when the Foundation input Motions (FIMs) are not measured, which is the case of almost all currently instrumented bridges in California. Here is a list of tasks carried out in this project:

[14] Refer to the Chapter 1 for accurate definition of terms like "bridge systems", "substructure", "superstructures", etc.

- A Matlab toolbox, called CSMIP-BRIDGE, was developed to automatically connect to the Center for Engineering Strong Motion Data (CESMD) to classify the bridges in California which are instrumented through California Strong Motion Instrumentation Program (CSMIP), a joint program conducted by the Department of Conservation (DOC) and California Department of Transportation (Caltrans), and some other agencies;

- A Matlab code was developed to automatically convert SAP2000 bridge models to the Opensees models;

- A series of direct simulations were carried out to see the importance of the inherent damping when other sources of damping are present;

- A robust model-based output-only Bayesian estimation method was developed for the purpose of joint input-parameter estimation;

- The method was extended to be able to be used for real-life problems which have specifications not usually considered in theoretical studies. For example, a double parallel-processing framework was designed and tested to make the method applicable even to a very large scale bridge structure with many uncertain parameters;

- The method was verified through simulated data obtained from numerical modeling of the Golden Gate Bridge;

- The real-life data of the Golden Gate Bridge was also used to test the performance of the method for real data;

- A pilot study for the specific purpose of inherent damping estimation was carried out using several real earthquake data sets recorded by a well-studied Meloland Road Overpass. This case is important as it is highly affected by the soil-structure interaction effects;

- Based on the Caltrans recommendations, two typical medium-size bridges in California were selected to be studied here whose results can be extended to many bridges in the state. In addition to their real-life data, extensive verification and identifiability studies were also carried out using these two nonlinear FE models.

8.2. CONCLUSIONS

The major findings of this study can be summarized as follows:

- Direct simulation using a single bridge model showed a quite complex behavior in the energy contribution pattern. That is, for the lowest level of modal damping, by increasing the level of ground motion, energy dissipated through damping mechanisms at the boundaries reduces and compensated by nonlinear behavior of the superstructure (e.g., plastic hinges) and inherent damping. If the level of excitation highly increases, the bridge superstructure mostly moves as a

rigid body system, so the contribution of the boundaries in the energy dissipation through damping or nonlinear behavior increases. However, if the level of inherent damping is too high then the variation in the ground motion intensity does not significantly change the contribution of the inherent damping.

- Close agreement between recorded and predicted responses (using updated models) in Meloland Road Overcrossing (MRO), San Roque Canyon (SRC), and Union Mills Bridge (UMB) shows that Rayleigh damping model is a suitable choice considering its advantage for making sparse damping matrix;

- For the bridges like Meloland Road Overpass which have monolithic abutments and high soil-structure interaction, the inherent damping decreases when the level of bridge response increases. Indeed, when the level of excitation increases the bridge superstructure mostly remains undeformed and moves as a rigid body due to significant soil-structure interaction effects. So, the contribution of superstructure's damping reduces.

- The SRC bridge shows almost zero damping in the first earthquake, i.e., San Simeon 2003 earthquake, because the bridge behaves almost quasi statically due to the absence of high-frequency components in the excitation. The identified damping from the Isla Vista 2013 earthquake clearly shows that the inherent damping is still a function of earthquake intensity! Also, this earthquake shows that 5% Rayleigh damping model for the first and last (significant) modes in low to the moderate earthquake is suitable. However, under weak excitation, much lower damping around 2% values should be considered.

- The behavior of the inherent damping in UMB is quite similar to what we observed in the SRC bridge. That is, the damping is a combination of mass and stiffness proportional parts in a large earthquake, i.e., Tohe Vista 2005, while it is mostly stiffness-proportional in King Beach 2004 and White Hawk 2011 earthquakes. The damping level behaves mostly mass-proportional with a low level of damping in the Truckee 2017 earthquake, which was a very weak event. So, we can similarly conclude that the traditional 5% Rayleigh damping model for the first and last (significant) modes in low to the moderate earthquake is suitable; while much lower damping around 2% values should be considered under weak excitation.

8.3. RECOMMENDATION FOR FUTURE STUDIES

The present project provided an opportunity to develop a robust and reliable solution for output-only FE model updating. This is a great advancement because we are now able to extract various information from data recorded by large-scale bridge structures during earthquakes, which could be representative of a real experimental test. The proposed solution works even in the absence of input motions, which is the case for almost all bridges because Foundation Input Motions (FIMs) are not measurable due to soil-structure interaction effects. However, the current study has some limitations which should be addressed in the future as follows:

- As identifiability studies showed, the lack of sensors on the foundation level prevents us to be able to estimate soil-foundation impedance functions. Unfortunately, most of the current CSMIP instrumented bridges have such problem. By adding instrumentation to the foundation level (even at a few piers), we will be able to extract valuable information from real-life data;

- The most part of the current project was devoted to developing the framework and its testing. Now, this developed method can be used to study more bridges to be able to aggregate results;

- While the Rayleigh damping model worked well for cases studied here, other models can be used too. Then, a systematic model class solution can be employed to find the most plausible (sufficiently simple and accurate) model. This may pave a way toward mechanics-based estimation of the damping!

- The level of ground motion data recorded by the bridges in this study was not large. Having more earthquake data with larger intensity can extend our conclusion for larger intensities;

- Aside from the main purpose of the current project, i.e., damping estimation, the developed methodology can be used for other purposes including Structural Health Monitoring and rapid post-event assessment. The updated FE models can be kept as Digital Twins to quickly detect any damages after a sever event.

REFERENCES

[1] R. Karoumi, "Some modeling aspects in the nonlinear finite element analysis of cable supported bridges," *Comput. Struct.*, 1999.

[2] A. Shamsabadi, K. M. Rollins, and M. Kapuskar, "Nonlinear Soil–Abutment–Bridge Structure Interaction for Seismic Performance-Based Design," *J. Geotech. Geoenvironmental Eng.*, vol. 133, no. 6, pp. 707–720, 2007.

[3] N. Johnson, M. S. Saiidi, and D. Sanders, "Nonlinear Earthquake Response Modeling of a Large-Scale Two-Span Concrete Bridge," *J. Bridg. Eng.*, 2009.

[4] R. Brincker, L. Zhang, and P. Andersen, "Modal identification of output-only systems using frequency domain decomposition," *Smart Mater. Struct.*, vol. 10, no. 3, pp. 441–445, 2001.

[5] M. I. Friswell and J. E. Mottershead, *Finite element model updating in structural dynamics*, vol. 38. 1995.

[6] B. Jaishi and W.-X. Ren, "Structural Finite Element Model Updating Using Ambient Vibration Test Results," *J. Struct. Eng.*, vol. 131, no. 4, pp. 617–628, 2005.

[7] E. Taciroglu, A. Shamsabadi, F. Abazarsa, R. L. Nigbor, and S. F. Ghahari, "Comparative study of model predictions and data from the Caltrans-CSMIP bridge instrumentation program: A case study on the Eureka-Samoa channel bridge. 2014," *Caltrans Rep. No*, no. October, 2014.

[8] A. F. Shakal, J. T. Ragsdale, and R. W. Sherburne, "CSMIP strong-motion instrumentation and records from transportation structures—Bridges," in *Lifeline Earthquake Engineering: Performance, Design and Construction*, 1984, pp. 117–132.

[9] P. K. Malhotra, M. J. Huang, and A. F. Shakal, "Seismic interaction at separation joints of an instrumented concrete bridge," *Earthq. Eng. Struct. Dyn.*, 1995.

[10] Y. Arici and K. M. Mosalam, "System identification of instrumented bridge systems," *Earthq. Eng. Struct. Dyn.*, vol. 32, no. 7, pp. 999–1020, 2003.

[11] J. Zhang and N. Makris, "Seismic Response Analysis of Highway Overcrossings including Soil-Structure Interaction," *Earthq. Eng. Struct. Dyn.*, vol. 31, no. 11, pp. 1967–1991, 2002.

[12] A. Zerva and V. Zervas, "Spatial variation of seismic ground motions: An overview," *Appl. Mech. Rev.*, vol. 55, no. 3, p. 271, 2002.

[13] J. P. Wolf and A. J. Deeks, *Foundation vibration analysis: A strength of materials approach*. Butterworth-Heinemann, 2004.

[14] S. F. Ghahari, F. Abazarsa, M. A. Ghannad, and E. Taciroglu, "Response-only modal identification of structures using strong motion data," *Earthq. Eng. Struct. Dyn.*, vol. 42, no. 8, 2013.

[15] S. F. Ghahari, F. Abazarsa, M. A. Ghannad, M. Celebi, and E. Taciroglu, "Blind modal identification of structures from spatially sparse seismic response signals," *Struct. Control Heal. Monit.*, vol. 21, no. 5, 2014.

[16] S. F. Ghahari, F. Abazarsa, and E. Taciroglu, "Blind modal identification of non-classically damped structures under non-stationary excitations," *Struct. Control Heal. Monit.*, 2016.

[17] F. Abazarsa, F. Nateghi, S. F. Ghahari, and E. Taciroglu, “Extended blind modal identification technique for nonstationary excitations and its verification and validation,” *J. Eng. Mech.*, vol. 142, no. 2, 2016.

[18] M. Iguchi and J. E. Luco, “Dynamic response of flexible rectangular foundations on an elastic half-space,” *Earthq. Eng. Struct. Dyn.*, vol. 9, no. 3, pp. 239–249, 1981.

[19] M. Mahsuli and M. A. Ghannad, “The effect of foundation embedment on inelastic response of structures,” *Earthq. Eng. Struct. Dyn.*, vol. 38, no. 4, pp. 423–437, 2009.

[20] R. Astroza, H. Ebrahimian, Y. Li, and J. P. Conte, “Bayesian nonlinear structural FE model and seismic input identification for damage assessment of civil structures,” *Mech. Syst. Signal Process.*, vol. 93, pp. 661–687, 2017.

[21] R. W. Clough and J. Penzien, *Dynamics of Structures*. 2013.

[22] T. Language and T. Computing, “MATLAB The Language of Technical Computing,” *Components*, vol. 3, no. 7, p. 750, 2004.

[23] CESMD, “Center for Engineering Strong Motion Data,” 2017. [Online]. Available: http://strongmotioncenter.org/. [Accessed: 01-Jan-2017].

[24] H. Huang, J. N. Yang, and L. Zhou, “Adaptive quadratic sum-squares error with unknown inputs for damage identification of structures,” *Struct. Control Heal. Monit.*, vol. 17, no. 4, pp. 404–426, 2010.

[25] H. Ebrahimian, R. Astroza, J. P. Conte, and C. Papadimitriou, “Bayesian optimal estimation for output-only nonlinear system and damage identification of civil structures,” *Structural Control and Health Monitoring*, 2018.

[26] S. J. Julier, “New extension of the Kalman filter to nonlinear systems,” in *Proceedings of SPIE*, 1997, pp. 182–193.

[27] A. K. Chopra and others, *Dynamics of structures*, vol. 3. Prentice Hall New Jersey, 1995.

[28] M. Bayes and M. Price, “An essay towards solving a problem in the doctrine of chances. by the late rev. mr. bayes, frs communicated by mr. price, in a letter to john canton, amfrs,” *Philos. Trans.*, pp. 370–418, 1763.

[29] R. E. Kalman, “A New Approach to Linear Filtering and Prediction Problems,” *J. Basic Eng.*, vol. 82, no. 1, pp. 35–45, 1960.

[30] H. Ebrahimian, R. Astroza, J. P. Conte, and R. A. de Callafon, “Nonlinear finite element model updating for damage identification of civil structures using batch Bayesian estimation,” *Mech. Syst. Signal Process.*, vol. 84, pp. 194–222, 2017.

[31] S. Haykin, *Kalman Filtering and Neural Networks*, vol. 5, no. 3. 2001.

[32] D. Simon and D. L. Simon, “Constrained Kalman filtering via density function truncation for turbofan engine health estimation,” *Int. J. Syst. Sci.*, vol. 41, no. 2, pp. 159–171, 2010.

[33] R. R. Ebrahimian, H.; Astroza, R.; Conte, J.P.; Bitmead, “An Information-theoretic Approach for Identifiability Assessment of Nonlinear Structural Finite Element Models,” *ASCE J. Eng. Mech.*, vol. in press, 2018.

[34] J. B. Strauss and C. E. Paine, *The Golden Gate bridge: report of the chief engineer to the Board of directors of the Golden Gate Bridge and Highway District, California, September, 1937*. Golden Gate Bridge, Highway and Transportation District, 1938.

[35] M. A. Ketchum and C. Seim, *Golden Gate bridge seismic evaluation*. TY Lin International, 1990.

[36] A. M. Abdel-Ghaffar and R. H. Scanlan, “Ambient vibration studies of golden gate bridge: I. Suspended structure,” *J. Eng. Mech.*, vol. 111, no. 4, pp. 463–482, 1985.

[37] A. M. Aabdel-Ghaffar and R. H. Scanlan, “Ambient Vibration Studies of Golden Gate Bridge: II. Pier-Tower Structure,” *J. Eng. Mech.*, vol. 101, no. 4, pp. 483–499, 1985.

[38] T. J. Ingham, S. Rodriguez, M. N. Nader, F. Taucer, and C. Seim, “Seismic retrofit of the golden gate bridge,” in *Proc., National Seismic Conf. on Bridges and Highways: Progress in Research and Practice*, 1995.

[39] M. Çelebi, “Golden Gate Bridge response: A study with low-amplitude data from three earthquakes,” *Earthq. Spectra*, vol. 28, no. 2, pp. 487–510, 2012.

[40] L. H. Nishkian, “Vertical vibration recorders for the Golden Gate Bridge,” *Bull. Seismol. Soc. Am.*, vol. 37, no. 2, pp. 81–88, 1947.

[41] G. S. Vincent, “Golden Gate bridge vibration studies,” *Trans. Am. Soc. Civ. Eng.*, vol. 127, no. 2, pp. 667–701, 1962.

[42] G. S. Vincent and M. Labse, “Correlation of predicted and observed suspension bridge behavior,” *Trans. Am. Soc. Civ. Eng.*, vol. 127, no. 2, pp. 646–666, 1962.

[43] H. Tanaka and A. G. Davenport, “Wind-Induced Response of Golden Gate Bridge,” *J. Eng. Mech.*, vol. 109, no. 1, pp. 296–312, 1983.

[44] S. N. Pakzad, G. L. Fenves, S. Kim, and D. E. Culler, “Design and Implementation of Scalable Wireless Sensor Network for Structural Monitoring,” *J. Infrastruct. Syst.*, vol. 14, no. 1, pp. 89–101, 2008.

[45] S. N. Pakzad and G. L. Fenves, “Statistical Analysis of Vibration Modes of a Suspension Bridge Using Spatially Dense Wireless Sensor Network,” *J. Struct. Eng.*, vol. 135, no. 7, pp. 863–872, 2009.

[46] S. N. Pakzad, G. V. Rocha, and B. Yu, “Distributed modal identification using restricted auto regressive models,” *Int. J. Syst. Sci.*, vol. 42, no. 9, pp. 1473–1489, 2011.

[47] M. Chang and S. N. Pakzad, “Modified Natural Excitation Technique for Stochastic Modal Identification,” *J. Struct. Eng.*, vol. 139, no. 10, pp. 1753–1762, 2013.

[48] T. J. Matarazzo and S. N. Pakzad, “Modal identification of golden gate bridge using pseudo mobile sensing data with STRIDE,” in *Dynamics of Civil Structures, Volume 4*, Springer, 2014, pp. 293–298.

[49] T. J. Matarazzo and S. N. Pakzad, “STRIDE for structural identification using expectation maximization: iterative output-only method for modal identification,” *J. Eng. Mech.*, vol. 142, no. 4, p. 4015109, 2016.

[50] J. Bendat and A. Piersol, *Engineering applications of correlation and spectral analysis*. 1993.

[51] L. Ljung, “System Identification: Theory for the user,” *Englewood Cliffs*, 1987.

[52] G. W. Housner and C. C. Thiel Jr., “Competing against time: report of the Governor’s Board of Inquiry on the 1989 Loma Prieta earthquake,” *Earthq. Spectra*, vol. Vol. 6, no. 4, p. 681–711. Nov., 1990.

[53] A. F. Shakal, C. D. Petersen, A. B. Cramlet, and R. B. Darragh, “CSMIP near-real-time strong motion monitoring system: Rapid data recovery and processing for event response,” in *Proceedings SMIP95 Seminar on Seismological and Engineering Implications of Recent Strong-Motion Data, Huang, MJ, Ed*, 1995.

[54] M. Huang, P. Hipley, and A. Shakal, “Seismic Instrumentation of Toll Bridges in California,” in *Sevnetgh National Seismic Conference on Brdiges and Highways, Oakland, Californa, Paper*, 2013, p. P10.

[55] François Auger, P. Flandrin, P. Gonçalvès, and O. Lemoine, “Time-Frequency Toolbox for Use with Matlab - Reference Guide,” *October*, pp. 1995–1996, 1996.

[56] M. ?elebi, Y. Hisada, R. Omrani, S. F. Ghahari, and E. Tacirogluc, “Responses of two tall buildings in Tokyo, Japan, before, during, and after the M9.0 Tohoku earthquake of 11 March 2011,” *Earthq. Spectra*, vol. 32, no. 1, 2016.

[57] F. Baron, M. Arikan, and R. E. Hamati, *The effects of seismic disturbances on the Golden Gate Bridge*. University of California, College of Engineering, Earthquake Engineering Research Center, 1976.

[58] A. M. Abdel-Ghaffar and E. E. R. Laboratory, “Dynamic analyses of suspension bridge structures,” 1976.

[59] A. M. Abdel-Ghaffar and L. I. Rubin, “Vertical seismic behaviour of suspension bridges,” *Earthq. Eng. Struct. Dyn.*, vol. 11, no. 1, pp. 1–19, 1983.

[60] A. M. Abdel-Ghaffar and R. G. Stringfellow, “Response of suspension bridges to travelling earthquake excitations: Part I. Vertical response,” *Int. J. Soil Dyn. Earthq. Eng.*, vol. 3, no. 2, pp. 62–72, 1984.

[61] A. M. Abdel Ghaffar and L. I. Rubin, “Lateral Earthquake Response of Suspension Bridges,” *J. Struct. Eng.*, vol. 109, no. 3, pp. 664–675, 1983.

[62] A. M. Abdel-Ghaffar and R. G. Stringfellow, “Response of suspension bridges to travelling earthquake excitations: Part II-lateral response,” *Int. J. Soil Dyn. Earthq. Eng.*, vol. 3, no. 2, pp. 73–81, 1984.

[63] A. M. Abdel-Ghaffar, R. H. Scanlan, and J. Diehl, *Analysis of the dynamic characteristics of the Golden Gate Bridge by ambient vibration measurements*. Princeton University, 1985.

[64] C. Seim and S. Rodriguez, “Seismic performance and retrofit of the Golden Gate bridge,” in *Structural Engineering in Natural Hazards Mitigation:*, 1993, pp. 133–138.

[65] C. Seim and M. Ketchum, “Golden Gate Bridge Mass Transit Feasibility Study, Golden Gate Bridge, Highway and Transportation District, San Francisco, California,” 1990.

[66] S. Rodriguez and T. J. Ingham, “Seismic protective systems for the stiffening trusses of the Golden Gate Bridge,” in *Proceedings of the National Seismic Conference on Bridges and Highways*, 1995.

[67] M. Nader and T. J. Ingham, “Seismic Retrofit of the Towers of the Golden Gate Bridge,” in *Proceedings of the National Seismic Conference on Bridges and Highways, San Diego, CA, December*, 1995.

[68] R. Imbsen and R. Schamber, “Seismic retrofit of the north approach viaduct of the Golden Gate Bridge,” *Transp. Res. Rec. J. Transp. Res. Board*, no. 1688, pp. 154–162, 1999.

[69] M. I. Gürelli and C. L. Nikias, “EVAM: An Eigenvector-Based Algorithm for Multichannel Blind Deconvolution of Input Colored Signals,” *IEEE Trans. Signal Process.*, vol. 43, no. 1, pp. 134–149, 1995.

[70] Y. Nakamura, A. Der Kiureghian, and D. Liu, *Multiple-support response spectrum analysis of the Golden Gate Bridge*, vol. 93, no. 5. Earthquake Engineering Research Center, University of California, 1993.

[71] R. A. Dameron, R. S. Dunham, and J. C. Castro, “Nonlinear analysis and experimental validation of a stiffening truss chord of the golden gate bridge,” in *Computing in Civil Engineering (New York)*, 1994, no. 2, pp. 1106–1114.

[72] T. Game, C. Vos, R. Morshedi, R. Gratton, F. Alonso-Marroquin, F. Tahmasebinia, and F. Alonso-Marroquin, “Full dynamic model of Golden Gate Bridge,” in *AIP Conference Proceedings*, 2016, vol. 1762, no. 1, p. 20005.

[73] Strand7, “Strand7 Finite Element Analysis System.” Strand7 Software Sydney, Australia, 2007.

[74] Hibbitt, Karlsson, and Sorensen, *ABAQUS/standard User’s Manual*, vol. 1. Hibbitt, Karlsson & Sorensen, 2001.

[75] S. V CSI, “8, 2002. Integrated Finite Element Analysis and Design of Structures Basic Analysis Reference Manual,” *Comput. Struct. Inc., Berkeley, California, USA*, 2010.

[76] F. McKenna, “OpenSees: a framework for earthquake engineering simulation,” *Comput. Sci. Eng.*, vol. 13, no. 4, pp. 58–66, 2011.

[77] J. G. Reid, “Structural Identifiability in Linear Time-Invariant Systems,” *IEEE Trans. Automat. Contr.*, vol. 22, no. 2, pp. 242–246, 1977.

[78] M. . Shrikhande and V. K. . Gupta, “Dynamic soil-structure interaction effects on the seismic response of suspension bridges,” *Earthq. Eng. Struct. Dyn.*, vol. 28, no. 11, pp. 1383–1403, 1999.

[79] S. D. Werner, J. L. Beck, and M. B. Levine, “Seismic response evaluation of Meloland Road Overpass using 1979 imperial Valley earthquake records,” *Earthq. Eng. Struct. Dyn.*, vol. 15, no. 2, pp. 249–274, 1987.

[80] A. W. Smyth, J. S. Pei, and S. F. Masri, “System identification of the Vincent Thomas suspension bridge using earthquake records,” *Earthq. Eng. Struct. Dyn.*, vol. 32, no. 3, pp. 339–367, 2003.

[81] J. P. Stewart, R. B. Seed, and G. L. Fenves, *Empirical evaluation of inertial soil-structure interaction effects*. Pacific Earthquake Engineering Research Center, 1998.

[82] J. C. Wilson and B. S. Tan, “Bridge abutments. Assessing their influence on earthquake response of meloland road overpass,” *J. Eng. Mech.*, vol. 116, no. 8, pp. 1838–1856, 1990.

[83] J. L. Beck, “Determining models of structures from earthquake records,” *Caltech*, 1978.

[84] S. R. F. Levine Marie B., “Dynamic response verification of simplified bridge-foundation model,” *J. Geotech. Eng.*, vol. 115, pp. 246–260, 1989.

[85] J. Zhang and N. Makris, “Seismic response analysis of highway overcrossings including soil-structure interaction,” 2001.

[86] J. Zhang and N. Makris, “Kinematic response functions and dynamic stiffnesses of bridge embankments,” *Earthq. Eng. Struct. Dyn.*, vol. 31, no. 11, pp. 1933–1966, 2002.

[87] O.-S. Kwon and A. S. Elnashai, “Seismic Analysis of Meloland Road Overcrossing Using Multiplatform Simulation Software Including SSI,” *J. Struct. Eng.*, vol. 134, no. 4, pp. 651–660, 2008.

[88] A. Kotsoglou and S. Pantazopoulou, “Response simulation and seismic assessment of highway overcrossings,” *Earthq. Eng. Struct. Dyn.*, vol. 39, no. 9, pp. 991–1013, 2010.

[89] A. Rahmani, M. Taiebat, and W. D. Liam Finn, “Nonlinear dynamic analysis of Meloland Road Overpass using three-dimensional continuum modeling approach,” *Soil Dyn. Earthq. Eng.*, vol. 57, pp. 121–132, 2014.

[90] A. Rahmani, M. Taiebat, W. D. Liam Finn, and C. E. Ventura, “Evaluation of substructuring method for seismic soil-structure interaction analysis of bridges,” *Soil Dyn. Earthq. Eng.*, vol. 90, pp. 112–127, 2016.

[91] A. Shamsabadi, T. Ostrom, and E. Taciroglu, “Three dimensional global nonlinear time history analyses of instrumented bridges to validate current bridge seismic design procedures,” 2013.

[92] C. E. Ventura, J. C. Carvajal, L. Finn, and J. Traber, “Ambient vibration testing of the meloland road overpass,” *4th Int. Oper. Modal Anal. Conf. IOMAC 2011*, pp. 162–168, 2011.

[93] V. Mosquera, A. W. Smyth, and R. Betti, “Utilization of strong-motion data for assessment of structural integrity in instrumented highway bridges,” *SMIP09*, vol. 65, 2009.

[94] J. C. Wilson and B. S. Tan, “Bridge abutments. Formulation of simple model for earthquake response analysis,” *J. Eng. Mech.*, vol. 116, no. 8, pp. 1828–1837, 1990.

[95] R. Omrani, B. Mobasher, X. Liang, S. Gunay, K. M. Mosalam, F. Zareian, and E. Taciroglu, “Guidelines for nonlinear seismic analysis of ordinary bridges: Version 2.0,” 2015.

[96] S. D. C. Caltrans, “Caltrans seismic design criteria, v. 1.7.” April, 2013.

[97] a. Aviram, A. Aviram, K. Mackie, K. Mackie, B. Stojadinovic, and B. Stojadinovic, “Guidelines for Nonlinear Analysis of Bridge Structures in California,” *PEER Rep.*, 2008.

[98] P. Kaviani, F. Zareian, and E. Taciroglu, “Seismic behavior of reinforced concrete bridges with skew-angled seat-type abutments,” *Eng. Struct.*, 2012.

[99] J. B. Mander, M. J. N. Priestley, and R. Park, “Theoretical Stress-Strain Model for Confined Concrete,” *J. Struct. Eng.*, 2008.

[100] S. Timoshenko, *Theory of Plates and Shells*. 1941.

[101] P. F. Silva, S. Megally, and F. Seible, “Seismic performance of sacrificial exterior shear keys in bridge abutments,” *Earthq. Spectra*, 2009.

[102] P. Khalili-Tehrani, A. Shamsabadi, J. P. Stewart, and E. Taciroglu, “Backbone curves with physical parameters for passive lateral response of homogeneous abutment backfills,” *Bull. Earthq. Eng.*, 2016.

[103] E. Mechanics, “Field investigation report for abutment backfill characterization,” *SSRP*, vol. 5, p. 2, 2005.

[104] J. P. Stewart, E. Taciroglu, J. W. Wallace, E. R. Ahlberg, A. Lemnitzer, C. Rha, P. Tehrani, S. Keowen, R. L. Nigbor, and A. Salamanca, “Full scale cyclic testing of foundation support systems for highway bridges. Part II: Abutment backwalls,” 2007.

[105] G. Gazetas, “Formulas and Charts for Impedances of Surface and Embedded Foundations,” *J. Geotech. Eng.*, 2008.

[106] A. Pais and E. Kausel, “Approximate formulas for dynamic stiffnesses of rigid foundations,” *Soil Dyn. Earthq. Eng.*, vol. 7, no. 4, pp. 213–227, 1988.